Volume 2 No. 6
Pt. I

SOVIET ATOMIC ENERGY

АТОМНАЯ ЭНЕРГИЯ
(ATOMNAYA ÉNERGIYA)

TRANSLATED FROM RUSSIAN

CONSULTANTS BUREAU, NEW YORK

THE BR-2 EXPERIMENTAL FAST NEUTRON REACTOR

A.I. Leipunskii, D.I. Blokhintsev, I.N. Aristarkhov, I.I. Bondarenko, O.D. Kazachkovskii, M.S. Pinkhasik, Iu.Ia. Stavisskii, E.A. Stumbur, F.I. Ukraintsev and L.N. Usachev

A brief survey is made of the design of the experimental fast neutron reactor and of its basic experimental and auxiliary equipment. The reactor was designed for physical experimentation with fast neutrons. The core is composed of plutonium rods; the lateral reflector is filled with depleted uranium. Heat is removed from the core by mercury and from the uranium reflector by air. The total rated power of the reactor is 150 kw of which about 100 kw is derived from the core.

The Reactor Core

The fuel elements of the BR-2 reactor are plutonium rods 10 mm in diameter and 130 mm long. These are enclosed in EIa1T stainless steel sealed tubes of 0.3 mm thickness.

Each fuel element is fastened to a long tungsten shaft clad in steel. In addition to the plutonium rods the core contains rods of depleted uranium of similar design. There is a total of 108 plutonium and uranium rods. The fuel element assembly is contained in a steel tube of 130 mm inside diameter. The heat-transfer agent occupies 17% of the core volume.

The Reflector

The reflector consists of a layer of uranium (outside diameter 700 mm) and a layer of copper (outside diameter 1000 mm). The uranium reflector is made of rods 35 mm in diameter which are steel jacketed.

The tungsten shafts of the fuel elements form the upper end reflector. The lower end reflector is made of uranium.

Control

The reactor is controlled by a regulating system and an emergency shutdown system. The control elements are the movable parts of the shield near the core. The principal element of the emergency system is a cylinder of 15 mm thickness moving in a circular opening close to the core. An auxiliary safety device and two automatic power regulators are placed in a second circular opening. All control elements are made of a copper-nickel alloy.

The control elements are lowered in order to reduce the reactor reactivity. Their maximum displacement of 130 mm produces the following changes in the reactivity:

Principal emergency element	3.6%
Auxiliary emergency element	0.9%
Automatic regulators (each)	0.2%

The control system also includes boron ionization chambers in the water shield of the reactor, electronic equipment and servodrives.

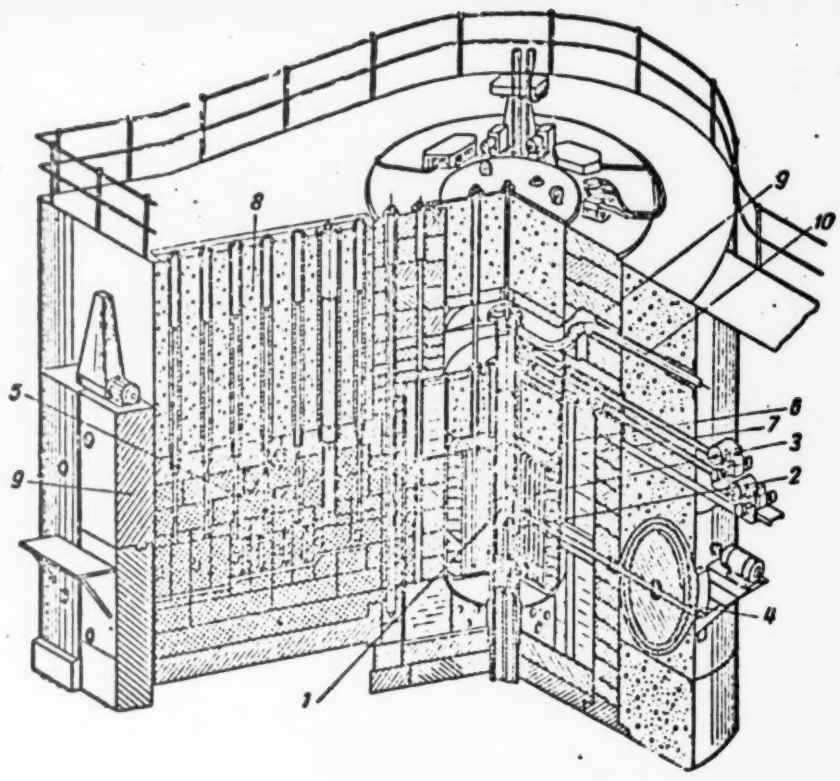

Fig. 1. Diagram of reactor: 1) core; 2) control and emergency devices; 3) reflector; 4) neutron beam channel; 5) thermal column; 6) ionization chamber channel; 7) water shield; 8) concrete shield; 9) cast iron shield; 10) mercury loop.

The emergency shutdown system is activated when a given power level is exceeded and danger signals are received from the technological equipment. The electromagnets which hold the protective elements are de-energized so that these elements drop under the action of gravity. The flow parameters are controlled by a system of control and measuring instruments which are read by the operator at the central instrument panel.

Under normal operating conditions the static temperature coefficient of pile reactivity was negative at $2 \cdot 10^{-5} \Delta k/C^{\circ}$. Under some operating conditions the static temperature coefficient was positive without affecting the stability of the reactor.

Heat Removal System

The mercury was circulated by a centrifugal pump with a capacity of 6 m^3 per hour. The mercury was cooled in a water heat exchanger. In case of breakdown or shutting-off of the pump, a separate loop with natural circulation was provided to give power extraction up to 20 kw.

Shielding

The shield of the reactor consists of: a) a water shield 500 mm thick; b) a layer of cast iron 400 mm thick; and c) a layer of heavy concrete ($\gamma = 4.2$ g/cm^3) 1200 mm thick.

The measuring ionization chambers are in the water layer, which is closest to the reactor. When the reactor is operating at its rated power the radiation level in the reactor room with beams completely cut off is considerably below the tolerance level and does not much exceed the cosmic ray background.

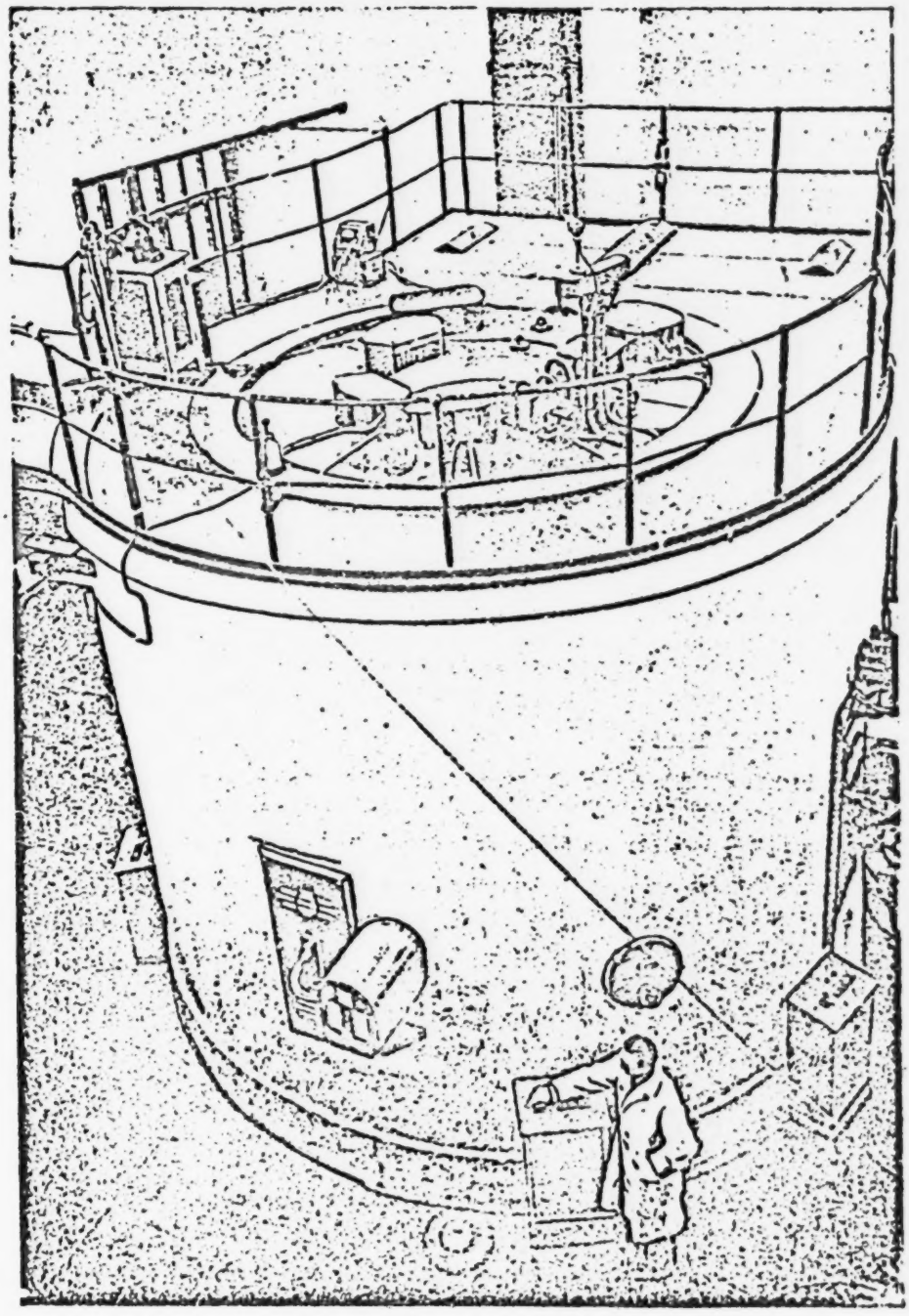

Fig. 2. General view of the reactor.

Building

A special laboratory building was constructed to house the reactor and its auxiliary equipment. The reac-

tor was placed in the main experimental hall which is 14 x 17 m^2 in area and 14 m high, thus providing ample space for physical experimenting. The technological and communication equipment is located in separate shielded rooms. The building also contains separate physical and chemical laboratories.

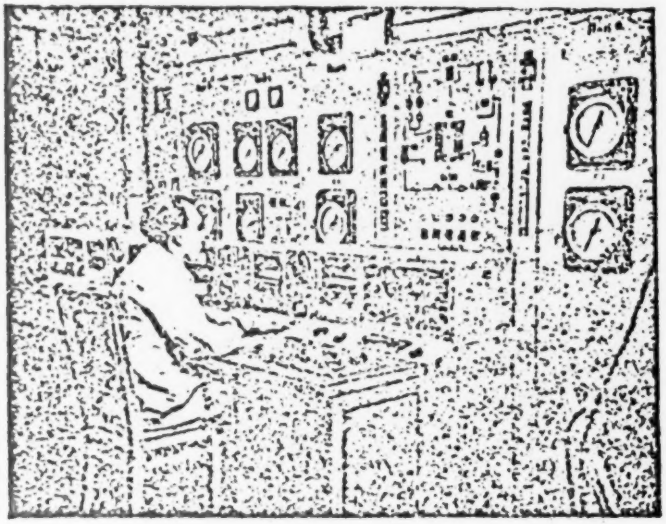

Fig. 3. Central control console and panels.

Experimental Arrangements

Central experimental channel. This channel passes vertically along the axis of the reactor through the core and end reflectors. Its inside diameter is 8 mm.

This channel is designed for the irradiation of specimens with powerful fast neutron beams.

The maximum fast neutron flux at the center of the core is 10^{14} neutrons/cm^2 sec. Specimens can be irradiated either with the hard spectrum of the core or with the softer spectra of the lower end reflector.

Experimental channels in the lateral reflector. The lateral reflector contains two experimental channels which are parallel to the reactor axis at distances of 160 and 260 mm. The inside diameter of the channels is 30 mm. These channels are designed for irradiation of specimens and for the installation of a local oscillator.

Neutron beams. The reactor has three horizontal channels for the extraction of fast neutron beams outside of the reactor shield. Two channels proceed directly from the core and the third from the lateral reflector. The channel diameter is 50 mm. The extracted neutron flux is 10^9 neutrons/cm^2 sec. The walls of the reactor room contain neutron trapping chambers opposite the beams.

Thermal column. For comparison of fast and thermal neutron cross sections the reactor is equipped with a graphite thermal column which is of the dimensions 1400 x 1400 x 2600 mm. For protection from the gamma ray background the column is separated from the reactor shield by a 200 mm layer of lead. The thermal neutron flux along the axis of the column varies from 10^{11} to 10^7 neutrons/cm^2 sec.

The thermal column contains several channels for the irradiation of specimens and for the extraction of a thermal beam outside of the reactor shield. There are also special channeling blocks placed along the axis of the thermal column.

Utilization of the Reactor

Various physical investigations have been conducted with the BR-2 reactor. Principal attention has been devoted to experiments for the determination and improvement of the physical constants that are required for

the designing of fast neutron power reactors which are known to breed nuclear fuel. Such experiments include the measurement of the fast neutron capture cross sections of various elements including fissionable elements. Fast neutron fission has been investigated, with the measurement of ν, etc. In addition the reactor has been used for experiments which are of interest for general nuclear physics, such as small angle neutron scattering, the production of isomers by inelastic neutron scattering, etc.

The effect of fast neutrons on various materials has also been studied.

The experimental results are being prepared for publication.

The reactor will be rebuilt in 1957 in order to provide a considerable increase of its power.

Received March 14, 1956

BLANK
PAGE

SCATTERING OF FAST PROTONS BY NONSPHERICAL NUCLEI

S.I. Drozdov

The angle distributions of protons scattered by spherical and nonspherical nuclei are considerably different. A comparison of the calculated and experimental results makes it possible to estimate the departure from sphericity of the nuclei. The scattering of fast protons by nonspherical nuclei is analyzed under the assumption that proton energy is large compared with the energy of the Coulomb barrier ($E \gtrsim 20$ Mev). The "black nucleus" model is used in conjunction with the adiabatic approximation according to which the calculation of the effective scattering cross sections is reduced to a determination of the scattering amplitudes for a fixed nucleus. It is shown that the amplitude can be given in the form of a sum of amplitudes for diffraction scattering and scattering in the electric field of the nucleus. Both parts of the amplitude are determined under the assumption that the nuclear shape does not exhibit a large departure from sphericity ($\alpha_2 Ze^2/\hbar v \ll 1$). The angle distributions for protons elastically scattered by even-even nuclei are calculated.

1. Formulation of the Problem

We shall be interested in the scattering of protons by nonspherical nuclei. If the proton time-of-flight in the vicinity of the nucleus is small compared with the rotational period of the nucleus, in determining the Ψ-function of the system the adiabatic approximation can be used:

$$\Psi(\mathbf{r}, \omega) \approx u_{\mathbf{k}}(\mathbf{r}, \omega)\varphi_n(\omega). \tag{1.1}$$

Here $u_{\mathbf{k}}(\mathbf{r}, \omega)$ is the wave function for the system comprised of the proton and a fixed nucleus; $\varphi_n(\omega)$ is the wave function for the rotational state of the nucleus which depends on the angle ω, determining the orientation; $\mathbf{k}$ and $\mathbf{r}$ are the wave vector and the position vector of the incident proton respectively. Thus, in the adiabatic approximation we analyze the scattering of a proton by a fixed nucleus which is in a rotational state $\varphi_n(\omega)$ prior to the scattering event.

The adiabatic approximation is valid if the following condition is fulfilled [1]:

$$kR\frac{\Delta\varepsilon}{E} \ll 1, \tag{1.2}$$

where kR is the ratio of the dimensions of the nucleus to the wavelength of the particle; $\Delta\varepsilon$ is the spacing between the first rotational levels and E is the energy of the particle.

The wave function $u_{\mathbf{k}}(\mathbf{r}, \omega)$, which describes the motion of the proton in the field of the fixed nucleus, assumes the following asymptotic form as $r \to \infty$:

$$u_{\mathbf{k}}(\mathbf{r}, \omega) \sim \left(1 + \frac{i\alpha^2}{kr - \mathbf{kr}}\right)e^{i\mathbf{kr} + i\alpha \ln(kr - \mathbf{kr})} + f(\Omega, \omega)\frac{e^{i(kr - \alpha \ln 2kr}}{r}, \tag{1.3}$$

where $f(\Omega, \omega)$ is the scattering amplitude of the proton in a direction Ω with respect to the fixed nucleus, which

depends on the orientation of the nucleus ω; $\alpha = Ze^2m/\hbar^2k$; Ze is the charge of the nucleus and m is the mass of the proton. In accordance with Equations (1.1) and (1.3) the Ψ-function of the system has the asymptotic form:

$$\Psi(\mathbf{r}, \omega) \sim \left[\left(1 + \frac{i\alpha^2}{kr - \mathbf{kr}}\right) e^{i(\mathbf{kr} + \alpha \ln(kr - \mathbf{kr})} + f(\Omega, \omega) \frac{e^{i(kr - \alpha \ln 2kr}}{r}\right] \varphi_n(\omega). \tag{1.4}$$

just as for neutrons [1], from this expression we determine the scattering cross sections with the excitation of rotational states of the nucleus. The differential scattering cross section in the direction Ω with the excitation of the rotational state $\varphi_{n'}(\omega)$ has the form

$$\left.\begin{aligned} \sigma_{n'n}(\Omega) &= |f_{nn'}(\Omega)|^2, \\ f_{nn'}(\Omega) &= \int \varphi^*_{n'}(\omega) f(\Omega, \omega) \varphi_n(\omega)\, d\omega. \end{aligned}\right\} \tag{1.5}$$

The wave functions for the rotational states of the nucleus are the eigenfunctions for a symmetric top:

$$\varphi_n(\omega) = \sqrt{(2I+1)/8\pi^2}\, D^I_{MK}(\omega), \tag{1.6}$$

where I is the total moment of the nucleus; M and K are the projections on an external axis and along the symmetry axis of the nucleus respectively. Substituting (1.6) in (1.5) and using the well-known relations for the functions in (1.6) [2], we obtain the following expression for the differential cross section for the excitation of a rotational level of the nucleus with an energy $\epsilon_{I'K}$ if prior to scattering the nucleus has a rotational energy ϵ_{IK}:

$$\sigma^{I'K}_{IK}(\Omega) = \sum_{\varkappa, m} \frac{2I'+1}{2\varkappa+1} (C^{\varkappa 0}_{I'KI\ K})^2 \times \left[\int Y^*_{\varkappa m}(\omega) f(\Omega, \omega) Y_{00}(\omega)\, d\omega\right]^2, \tag{1.7}$$

where the $C^{\varkappa 0}_{I'KI-K}$ are the Clebsch-Gordan coefficients, $Y_{Km}(\omega)$ are the normalized spherical functions. In particular, the differential cross section for elastic scattering is determined from Equation (1.7) for $I' = I$.

Hence, in the adiabatic approximation the solution of the problem reduces itself to the determination of the scattering amplitude $f(\Omega, \omega)$ for a fixed nucleus.

2. Scattering Amplitude

In calculating the amplitudes $f(\Omega, \omega)$ we shall assume that the wavelength of the incident protons is considerably smaller than the dimensions of the nucleus ($kR \gg 1$) and that the nucleus absorbs all particles which are incident upon it (black nucleus). In this case the scattering of protons can be considered as a quasi-classical analog to the diffraction of light or neutrons on a black body.

We now generalize the Kirchoff diffraction theory [3] to the case of charged-particle scattering. Let $u(\mathbf{r}) \equiv u_k(\mathbf{r}, \omega)$ be the wave function which describes the motion of the particle in the field of a fixed nucleus and which satisfies the Schrödinger equation

$$[\Delta + K^2(\mathbf{r}, \omega)]\, u(\mathbf{r}) = 0,$$

and let $G(\mathbf{r}, \mathbf{r}_0)$ be the corresponding Green's function

$$\Delta + K^2(\mathbf{r}, \omega)\, G(\mathbf{r}, \mathbf{r}_0) = -4\pi\delta(\mathbf{r} - \mathbf{r}_0).$$

Then, as is well known, we have the following relation:

$$u(\mathbf{r}_0) = \frac{1}{4\pi} \int_S [u(\mathbf{r}) \nabla G(\mathbf{r}, \mathbf{r}_0) - G(\mathbf{r}, \mathbf{r}_0) \nabla u(\mathbf{r})]\, ds, \tag{2.1}$$

where the integration is carried out over some closed surface S. We choose the surface S such that it passes through the nucleus. Since the nucleus is black, on this surface in the region of the nuclear shadow S_S in the first approximation the wave function u(r) can be set equal to zero. In this same approximation, on the surface S outside the shadow of the nucleus the functions u and G can be assumed to be those which would exist in the absence of the nuclear forces. Then

$$u(r_0) = \frac{1}{4\pi} \int_{S-S_S} [\psi(r) \nabla g(r, r_0) - g(r, r_0) \nabla \psi(r)] ds, \tag{2.2}$$

where

$$\begin{gathered} [\Delta + k^2(r, \omega)] \psi(r) = 0; \\ [\Delta + k^2(r, \omega)] g(r, r_0) = -4\pi\delta(r - r_0); \\ k^2(r, \omega) = \frac{2m}{\hbar^2} [E - V(r, \omega)], \end{gathered} \tag{2.3}$$

where $V(r, \omega)$ is the electrostatic energy of the interaction of the particle with the nucleus, which depends on the orientation ω. Thus, the wave function $\psi(r)$ describes the motion of the particle in the electric field of the nucleus. In accordance with Equations (2.1) and (2.2)

$$u(r_0) = \psi(r_0) + \frac{1}{4\pi} \times \int_{S_S} [g(r, r_0) \nabla \psi(r) - \psi(r) \nabla g(r, r_0)] ds, \tag{2.4}$$

where the integration is carried out over the area of the nuclear shadow.

In scattering problems the point of observation is usually taken at infinity ($r_0 \to \infty$). In this case the function $u(r_0) \equiv u_k(r_0, \omega)$ in the left-hand part of Equation (2.4) assumes the asymptotic form (1.3). On the other hand, in the right-hand side of the equation the function $\psi(r_0)$, which describes the scattering in the electric field of the nucleus, assumes the following form at infinity:

$$\psi(r) \sim \left(1 + \frac{f_0}{kr - kr}\right) e^{i(kr + \alpha \ln(kr - kr)} + f_e(\Omega, \omega) \frac{e^{ikr - i\alpha \ln 2kr}}{r}, \tag{2.5}$$

where $f_e(\Omega, \omega)$ is the scattering amplitude in the electric field of the nucleus, which depends on the orientation ω. Substituting (1.3) and (2.5) in (2.4) we find that the integral over the area of the nuclear shadow in (2.4) has an asymptotic form similar to a diverging wave

$$\frac{1}{4\pi} \int_{S_S} [g(r, r_0) \nabla \psi(r) - \psi(r) \nabla g(r, r_0)] ds \sim f_d(\Omega, \omega) \frac{e^{ikr - i\alpha \ln 2kr}}{r}. \tag{2.6}$$

In this expression the function $f_d(\Omega, \omega)$ is naturally called the diffraction-scattering amplitude. According to Equations (1.3) and (2.4-2.6),

$$f(\Omega, \omega) = f_e(\Omega, \omega) + f_d(\Omega, \omega),$$

that is, the scattering amplitude comprises the sum of the amplitudes associated with diffraction scattering and scattering due to the electric field of the nucleus.

3. Diffraction-Scattering Amplitude

The function $g(r, r_0)$ which appears in the integral in (2.6) is the wave function for the charged particles which emanate at the point r and move in the electric field of the nucleus. It follows that for $r_0 \to \infty$ the function $g(r, r_0)$ should assume the form of a diverging wave. As is well known

$$g(\mathbf{r}, \mathbf{r}_0) = \frac{1}{2\pi i} \int_C \frac{\psi_{\mathbf{k}'}(\mathbf{r}, \omega)\, \psi_{\mathbf{k}'}(\mathbf{r}_0, \omega)}{k'^2 - k^2}\, dk', \tag{3.1}$$

where $\psi_{\mathbf{k}}(\mathbf{r}, \omega) \equiv \psi(\mathbf{r})$ are wave functions which satisfy Equation (2.3) and the boundary Condition (2.5); the path of integration C in the complex plane of the variable k' passes around the point $k' = k$ from below in accordance with the boundary conditions at infinity. For $r_0 \to \infty$, from (3.1) and (2.5) we have

$$g(\mathbf{r}, \mathbf{r}_0) \sim \psi_{-\mathbf{k}'}(\mathbf{r}, \omega) \frac{e^{(ikr_0 - i\varkappa \ln 2kr}}{r_0}, \tag{3.2}$$

where $\mathbf{k}' = k\mathbf{r}_0/r_0$ is the wave vector of the scattered particle. Substituting (3.2) in (2.6) we find the amplitude for diffraction scattering

$$f_d(\Omega, \omega) = \frac{1}{4\pi} \int_{S_S} [\psi_{-\mathbf{k}'}(\mathbf{r}, \omega) \nabla \psi_{\mathbf{k}}(\mathbf{r}, \omega) - \psi_{\mathbf{k}}(\mathbf{r}, \omega) \nabla \psi_{-\mathbf{k}'}(\mathbf{r}, \omega)]\, d\mathbf{s}. \tag{3.3}$$

In this integral the wave functions $\psi_{\mathbf{k}}(\mathbf{r}, \omega)$ which describe the motion of the particle in the electric field of the nucleus are, generally speaking, unknown; only the asymptotic forms are known (2.5). The surface of integration S_S is equal to the area of the nuclear shadow on an arbitrary surface S, which passes through the nucleus. For simplicity, S_S may be taken as a surface which is perpendicular to the direction of the incident beam k. The area S_S depends on the orientation of the nucleus ω. For $E \gg Ze^2/R (kR \gg \alpha)$ it is possible to neglect the deformation of the trajectories of the incident particles in the electric field of the nucleus. In this case, the surface S_S, without change of shape, can be displaced in the direction k to a rather large distance from the nucleus a_0 such that the wave functions $\psi_{\mathbf{k}}(\mathbf{r}, \omega)$ can be represented by their asymptotic forms at this surface (2.5). As is well known [4], for $kR \gg 1$, the main contribution in the scattering amplitude comes from the large values of the impact parameters; these values correspond to incident particles at the edge of the surface S_S. In this case, the diverging wave in (2.5) does not give an important contribution in the integral (3.3) and hence, in making the substitutions in (3.3) it is possible to make use of only the distorted plane waves:

$$\left.\begin{aligned} \psi_{\mathbf{k}}(\mathbf{r}, \omega) &\sim e^{i(kr + \varkappa \ln(kr - \mathbf{kr})}, \\ \psi_{-\mathbf{k}'}(\mathbf{r}, \omega) &\sim e^{i(\mathbf{k}'\mathbf{r} + \varkappa \ln(kr + \mathbf{k}'\mathbf{r})}. \end{aligned}\right\} \tag{3.4}$$

Substituting (3.4) in (3.3) and changing the variable of integration $\left(\mathbf{r} = \mathbf{a}_0 + \boldsymbol{\rho},\ k\mathbf{r} \approx k\mathbf{a}_0 + \frac{(k\boldsymbol{\rho})^2}{2ka_0}\right)$, for small scattering angles, $\theta \ll 1$, we obtain

$$f_d(\Omega, \omega) = \frac{ik}{2\pi} \int_{\sigma} e^{-i\mathbf{k}'\boldsymbol{\rho} + 2i\varkappa \ln k\rho}\, d\boldsymbol{\rho},\ \alpha \ll kR,\ \theta \ll 1. \tag{3.5}$$

As is to be expected, the parameter a_0 in Equation (3.5) drops out. For $\alpha = 0$ this equation describes neutron scattering.

---

*From the derivation of Equation (3.5) it is apparent that in calculating the amplitudes for the diffraction scattering it is not necessary to take account of the fine details of the electric field of the nucleus. Hence, in verifying Expression (3.5) it is possible to apply any method, using for $\psi_{\mathbf{k}}(\mathbf{r}, \omega)$ the Coulomb wave functions

$$\psi_{\mathbf{k}}^{c}(\mathbf{r}) = e^{-\pi\varkappa/2}\, \Gamma(1 + i\varkappa)\, e^{i\mathbf{kr}}\, F[-i\varkappa, 1, i(kr - \mathbf{kr})],$$

which describe the motion of the particle in the field of a point charge at the center of the nucleus. In this case, the surface of integration S_S in (3.3) can be chosen as a surface which passes through the center of the nucleus $r = 0$ perpendicularly to the incident beam ($\mathbf{kr} = 0$). The main contribution in the integral (3.3) comes from the large impact parameters $k\rho \sim kR \gg 1$. Using the asymptotic representation of the hypergeometric function $F(-i\alpha, 1, ikr)$, for $\alpha \ll kr$, we obtain (3.5).

Let the nucleus be an ellipsoid of rotation with semiaxes $\underline{a}$ and $\underline{b}$ with $\underline{a}$ along the axis of symmetry. In this case the integration in (3.5) is taken over the area of the ellipse S_S with semi-axes $\underline{b}$ and

$$a' = b\sqrt{z^2 + (1-z^2)\mu^2}, \quad z = a/b, \quad \mu = \cos\vartheta,$$

$(\vartheta, \varphi) = \omega$. In polar coordinates the integral in (3.5) has the form

$$f_d(\Omega, \omega) =$$

$$= \frac{ik}{2\pi}\xi(\mu)\int_0^b\int_0^{2\pi}\exp\{-ik\rho\vartheta[\xi^2(\mu)\cos^2(\varphi-\Phi)+$$

$$+\sin^2(\varphi-\Phi)]^{\frac{1}{2}}\cos\varphi' +$$

$$+2i\alpha\ln[k\rho(\xi^2(\mu)\cos^2(\varphi'-\varphi_1)+$$

$$+\sin^2(\varphi-\varphi_1))^{\frac{1}{2}}]\rho\,d\rho\,d\varphi',$$

$$\sin\varphi_1 = \sin(\varphi-\Phi)[\xi^2(\mu)\cos^2(\varphi-\Phi)+$$

$$+\sin^2(\varphi-\Phi)]^{\frac{1}{2}}, \quad (\vartheta, \Phi) = \Omega.$$

If the nuclear shape is almost spherical, since $\alpha\left|\frac{a}{b}-1\right| \ll 1$, the argument of the logarithm may be taken as $k\rho$. Then the integration over φ' leads to a Bessel function of zero order:

$$f_d(\Omega, \omega) = \frac{i}{k}\xi(\mu)\left(\frac{kb}{t}\right)^{2(1+i\alpha)}\int_0^t x^{1+2i\alpha}J_0(x)\,dx.$$

Integrating by parts

$$\int_0^t x^{1+2i\alpha}J_0(x)\,dx = t^{1+2i\alpha}J_1(t) - 2i\alpha\int_0^t x^{2i\alpha}J_1(x)\,dx$$

and using the well-known relations between the Bessel functions $J_n(x)$ and the Γ-function $\Gamma(x)$:

$$J_1(x) = x\sum_{n=0}^{\infty}\frac{t^{n-1}J_{1+n}(t)}{n!\,2^n}\left[1-\left(\frac{x}{t}\right)^2\right]^n,$$

$$\int_0^1 u^{i\alpha}(1-u)^n\,du = \frac{n!\,\Gamma(1+i\alpha)}{\Gamma(2+n+i\alpha)},$$

we obtain the following expression for the diffraction part of the scattering amplitude

$$f_d(\Omega, \omega) = \frac{i}{k}(kb)^{2(1+i\alpha)}\xi(\mu)\times$$

$$\times\left[\frac{J_1(t)}{t} - i\alpha\sum_{n=0}^{\infty}\frac{\Gamma(1-i\alpha)\,t^{n-1}J_{1+n}(t)}{2^n\Gamma(2+n+i\alpha)}\right], \qquad (3.6)$$

$$t = kb\vartheta\sqrt{\xi^2(\mu)\cos^2(\varphi-\Phi)+\sin^2(\varphi-\Phi)},$$

$$\alpha\left|\frac{a}{b}-1\right| \ll 1, \quad a \ll kR.$$

For $\alpha = 0$ this equation described neutron scattering [1].

4. Scattering Amplitude in the Electric Field of the Nucleus

The equation which describes the nuclear surface can be given in the form

$$r(\mu') = R'(1 + a(\mu')), \quad a(\mu') = \sum_{n>1} a_n P_n(\mu'), \tag{4.1}$$

where μ' is the cosine of the angle between the symmetry axis of the nucleus and the radius vector. The electrostatic energy of the proton $V(r, \omega)$ in the field of the nucleus is given by the expression

$$\Delta V_1(r, \omega) = -\frac{3Ze^2}{R^3}, \quad \Delta V_2(r, \omega) = 0,$$

the solutions of which must be joined at the surface of the nucleus (4.1). When the shape does not depart very far from sphericity, in joining the solutions it is convenient to expand the functions V in a series in the parameter $a(\mu')$. Moreover, in investigating scattering at small angles, the finite dimensions of the nucleus can be neglected. In this case the electrostatic energy of the proton, to a first approximation, has the form

$$\begin{aligned} V(r, \omega) &= \frac{Ze^2}{r} + V_1(r, \omega); \\ V_1(r, \omega) &= \sum_n V_n(r) P_n(\mu'); \\ V_n(r) &= \frac{3a_n}{2n+1} \frac{Ze^2R^n}{r^{n+1}}. \end{aligned} \tag{4.2}$$

To calculate the scattering amplitude in the electric field (4.2) we shall use perturbation theory, taking the energy of the multipole interaction $V_1(r, \omega)$ as the energy perturbation. In the first approximation the scattering amplitude in the electric field of the nucleus assumes the form

$$f_e(\Omega, \omega) = f_k(\theta) - \frac{2m}{\hbar^2} \sum_{n,m} \frac{Y^*_{nm}(\omega)}{2n+1} \times \int \phi^*_{-k'}(r) V_n(r) Y_{nm}\left(\frac{r}{r}\right) \phi^+_k(r)\, dr, \tag{4.3}$$

where the $\phi^+_k(r)$ are the Coulomb wave functions, which describe the scattering of the particle in the field Ze^2/r; $f_c(\theta)$ is the amplitude of the Coulomb scattering (5.4).

Perturbation theory can be used (4.3) in the case in which the energy of the particle is considerably greater than the Coulomb barrier ($kR \gg \alpha$), by applying the formula for the scattering amplitude at small angles $\theta \lesssim (kR)^{-1}$:

$$f_e(\Omega, \omega) = \frac{ik}{2\pi} \int e^{-ik\rho} \left[1 - \exp\left(-\frac{im}{\hbar^2 k} \times \int_{-\infty}^{\infty} \left(\frac{Ze^2}{r_e} + V_1(r, \omega)\right) dz\right)\right] d\rho,$$

where the integration is carried out over the plane (x, y), perpendicular to the direction of the incident beam. In the integral over ρ an important contribution comes from distances $\rho \sim R$. Considering the interaction $V_1(r, \omega)$ as a perturbation, we expand in a series

$$\exp\left(-\frac{im}{\hbar^2 k} \int_{-\infty}^{\infty} V_1(r, \omega)\, dz\right) \approx 1 - \frac{im}{\hbar^2 k} \int_{-\infty}^{\infty} V_1(r, \omega)\, dz + \cdots$$

From this expression and Equation (4.2) it is easy to show that the conditions for applying perturbation theory assume the form $\alpha a_2 \ll 1$ or

$$a\left|\frac{a}{b} - 1\right| \lesssim 1.$$

This condition was used in the above in calculating the diffraction-scattering amplitude (3.6).

5. Elastic Scattering of Protons on Even-Even Nuclei

In accordance with Equation (2.7) the scattering amplitude for protons scattered by a fixed nucleus is determined by the sum of the amplitudes for diffraction scattering (3.6) and scattering due to the electric field (4.3). It is easily verified that for $\alpha_n = 0$ ($a/b = 1$) the expression which is obtained coincides with the formula for the diffraction-scattering amplitude on a black spherical nucleus [4].

According to (1.7) the differential cross section for elastic scattering has a particularly simple form for scattering on even-even nuclei which are in the ground state prior to scattering

$$\sigma_0(\theta) = \left| \int f(\Omega, \omega) Y_{00}^* d\omega \right|^2. \tag{5.1}$$

In the first perturbation approximation the multipole electric interaction, in accordance with (2.7), (5.1) and (4.3), gives no contribution in the cross section for elastic scattering because of the orthogonality of the spherical functions. In this case the amplitude for elastic scattering is made up of the mean value for the diffraction part and the amplitude of the Coulomb scattering:

$$\int f(\Omega, \omega) Y_{00}^* d\omega = \int f_d(\Omega, \omega) Y_{00}^* d\omega + f_k(\theta), \tag{5.2}$$

in which, according to (3.6)

$$\int f_d(\Omega, \omega) Y_{00}^* d\omega = i \frac{2}{\pi k} (kb)^{2(1+ia)} \int_0^1 \int_0^{\pi/2} \xi(\mu) F(t) d\mu d\varphi, \tag{5.3}$$

$$F(t) = \frac{J_1(t)}{t} - ia \sum_{n=0}^{\infty} \frac{t^{n-1} J_{1+n}(t) \Gamma(1+ia)}{2^n \Gamma(2+n+ia)},$$

$$t = kb0 \sqrt{\xi^2(\mu) \cos^2\varphi + \sin^2\varphi},$$

$$f_c(\theta) = -\frac{2a}{k} \exp\left\{ -2ia \ln \frac{\theta}{2} \right\} \frac{\Gamma(1+ia)}{\Gamma(1-ia)}. \tag{5.4}$$

The conditions under which the obtained formulas can be used, (3.6), are satisfied at proton energies $E \gtrsim 20$ Mev.

Using Equations (5.1-5.4) the angle distributions have been calculated for protons with energies of 20, 30 and 50 Mev elastically scattered on Gd_{64}^{160} and U_{92}^{238}. In Figures 1-4 are shown curves for the ratio of the cross section for elastic scattering $\sigma_0(0)$ to the cross section for Coulomb scattering $\sigma_c(0) = |f_c(0)|^2$. The curves have been plotted for spherical and nonspherical nuclei ($z = a/b$ equal to 1.0 and 1.3 respectively) and the volumes of the spherical and nonspherical nuclei have been assumed equal ($zb^3 = R^3$, $R = 1.3 \cdot 10^{-13} A^{1/3}$ cm). As is to be expected in the small-angle region there is Coulomb scattering; the corresponding angular interval is independent of the deformation parameter z. In the region of comparatively high angles $\theta \sim (kR)^{-1}$, the cross section for elastic scattering is essentially less than for Coulomb scattering and the angle distribution of the protons is similar to the distribution of neutrons elastically scattered by nonspherical nuclei [1]. Actually, as is apparent from the figures, in the region of comparatively large angles, diffraction scattering takes place and the angle distribution exhibits characteristic maxima and minima. The cross section for elastic scattering in this region depends in an essential way on the deformation parameter z. With increasing z the probability for elastic scattering in this angle region is reduced and the diffraction maxima and minima become smeared out. For example, when z is increased from 1.0 to 1.3 the height of the maxima is reduced by two or three times. The

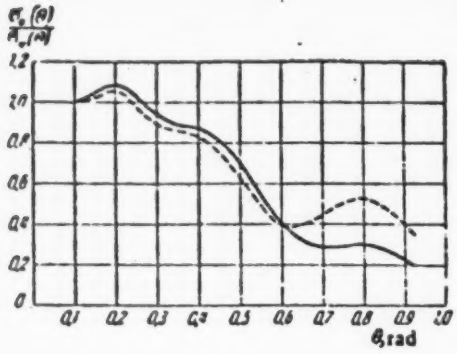

Fig. 1. E = 20 Mev, nucleus Gd^{160}_{64}.

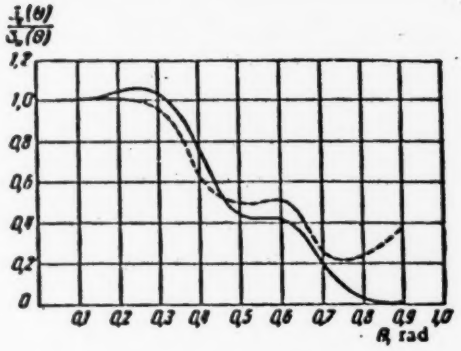

Fig. 2. E = 30 Mev, nucleus Gd^{160}_{64}.

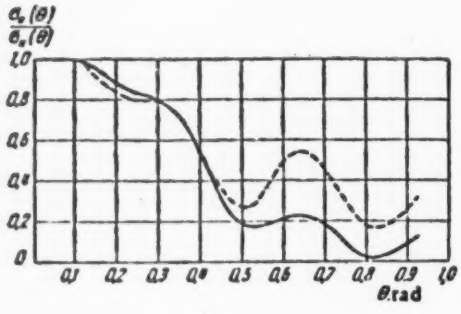

Fig. 3. E = 30 Mev, nucleus U^{238}_{92}.

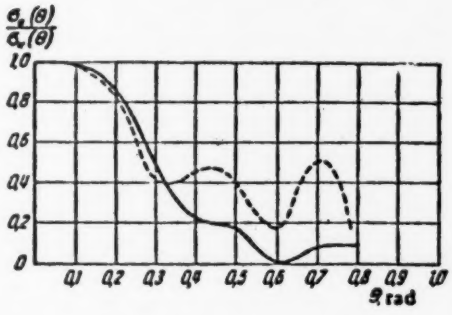

Fig. 4. E = 50 Mev, nucleus U^{238}_{92}.

The ratio of the differential cross section for elastic scattering of protons $\sigma_0(0)$ with an energy E to the cross section for Coulomb scattering $\sigma_C(0)$; the dashed curves apply to a spherical nucleus ($z = a/b = 1.0$, $R = 1.3 \cdot 10^{-13} A^{1/3}$ cm), the solid curves apply to a nonspherical nucleus of the same volume.

positions of the maxima and minima are virtually independent of z. A comparison of Figures 1–4 also shows that when the proton energy or the nuclear dimensions are increased, the diffraction maxima and minima are displaced toward the small-angle region.

The author wishes to express his sincere gratitude to B.T. Geilikman who proposed this problem and also to K.A. Ter Martirosyan, B.G. Nosov and V.M. Galitsky for a number of valuable discussions. The author is also indebted to N.M. Trukachev for carrying out the numerical calculations.

LITERATURE CITED

[1] S.L. Drazdov, J. Exptl. Theoret. Phys. 28, 734 (1955); 30, 786 (1956).

[2] K. Alder, Helv. Phys. Acta 25, 251 (1952).

[3] M. Born Optics, Kharkov-Kiev DNTVY 1937, No. 45, 46.

[4] A. Akhiezer and I. Pomeranchuk, Certain Problems in the Theory of the Nucleus (State Tech. Press, Moscow-Leningrad, 1950), §22.

[5] L.I. Schiff, Phys. Rev. 103, 443 (1956).

Received December 27, 1956

STATISTICAL THEORY FOR THE ANGLE DISTRIBUTION OF FISSION FRAGMENTS

V.M. Strutinsky

The angle distribution for fission fragments is considered at high excitation levels; in this case the angular momentum is distributed over a large number of nucleons and statistical theory can be applied to the nucleus. The distribution of states of the "transition" nucleus over values of the quantity K, the projection of the moment of the compound nucleus along the fission axis, is computed. The most probable state is found to be that with $K = 0$, which, in the case of neutron-induced fission leads to the appearance of maxima in the fragment angle distribution at 0° and 180°. The results are compared with experiment; the moment of inertia of the "transition" nucleus with respect to the symmetry axis is determined (fission direction). The fragment angle distribution for fission induced by charged particles and γ-rays is also analyzed.

In recent years a great deal of work has been devoted to investigations of the anisotropy in the fission-fragment angle distribution in fission induced by protons [1, 2], neutrons [3, 4] and γ-rays [5-7]. In certain cases the angle distribution of the fragments has also been measured. The general characteristics of the fission-fragment angle distribution in fission induced by particles of low energy has been discussed in References [8, 9]. In capture of a γ-quantum or a nucleon with energies of 1-2 Mev, a compound nucleus is formed with spin oriented in a certain direction with respect to the particle beam. The fragment angle distribution is determined by the relation between the direction of spin of the compound nucleus and the fission direction (line of flight of the fragments), that is, for a given total moment the angle distribution is determined by the quantity K, the projection of the total moment on the fission direction. At energies close to threshold almost all the energy of the initial excitation of the compound nucleus is transferred at the saddle point in the potential energy of deformation. Hence, in fission close to threshold, at the saddle point there should exist a system of well separated levels, each of which is characterized by a definite value of K. The fragment angle distribution is then determined by the particular state through which fission occurs [8-10]. This implies a marked dependence of the angle distribution on the energy of the incoming particle at energies close to threshold. It appears that an effect of this kind has been observed experimentally [4, 10].*

As has been shown by the experimental data, at high energies the anisotropy in the fission-fragment angle distribution in fission induced by neutrons increases with increasing energy, reaching a maximum at 7-10 Mev and then falling off (Figure 1). At neutron energies above 2 Mev the fissioning nucleus is highly excited and the level density in the nucleus becomes large; hence, some other mechanism becomes responsible for the angle distribution. It is reasonable to assume that at this energy the "transition" nucleus can be reasonably described in terms of a statistical model. Furthermore, when the kinetic energy of the incoming neutron is higher than 3-4 Mev, the momentum imparted to the nucleus is large ($kR \gtrsim 4$-5), so that it can be considered as a classical vector. We shall limit ourselves to the case in which the target nucleus is an even-even nucleus or has a spin which is small compared with the orbital moment of the incoming particle. Qualitatively, the role of the initial spin is clear: the larger the spin of the target nucleus, the smaller the anisotropy in the angle distribution of the fragments; this situation exists because of the poor alignment of the spin of the compound nu-

*This model (the "transition-nucleus" model) is also found to be suitable for explaining a number of other features of fission [11].

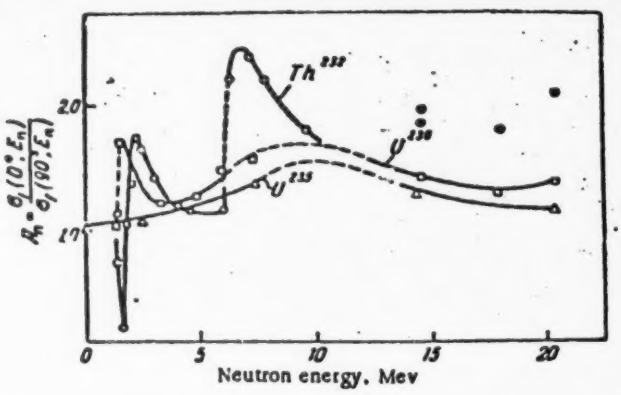

Fig. 1. Anisotropy in fragment angle distribution as a function of neutron energy.

cleus.

If the spin of the target nucleus is small or zero the moment of the compound nucleus coincides with the orbital moment of the neutron and, like the latter, is oriented in the plane perpendicular to the neutron beam. The symmetry axis of the "transition" nucleus coincides with the fission direction and forms an angle Φ ($\cos\Phi = K/i$) with the direction of the total moment.* Averaging to take account of the rotation of the nuclear axis about the spin direction and taking an average to account for the direction of the spin in the plane perpendicular to the beam, it is possible to determine the probability for a given orientation of the axis of the "transition" nucleus for fixed values of K and $\underline{i}$ [8]:

$$F_{i,K}(\vartheta)\,d\Omega = \frac{1}{\sqrt{\sin^2\vartheta - (K/i)^2}}\,d\Omega, \tag{1}$$

where ϑ is the angle with respect to the neutron beam; $\underline{i}$ is the total moment of the system; K is the projection on the symmetry axis of the transition nucleus. This expression must be summed over all possible values of K:

$$F_i(\vartheta) = \sum_{K=0}^{i} \frac{a(K)}{\sqrt{\sin^2\vartheta - (K/i)^2}}. \tag{2}$$

The total fission probability from a state characterized by moment $\underline{i}$ is

$$W(i) = 2\pi \int_0^{2\pi} \sin\vartheta\,d\vartheta\,F_i(\vartheta) = \sum_{K=0}^{i} a(K). \tag{3}$$

This relation determines the normalization conditions for a(K). It will be assumed that the fission probability from a state with spin $\underline{i}$ is independent of $\underline{i}$, i.e.,

*It may be assumed that at high excitations K is not a good quantum number since the quantum-mechanical condition for adiabaticity of rotation (the distance between levels must be large compared with the energy of rotation) no longer holds. In the statistical case, however, another criterion applies, namely, that the energy of rotation assigned to one particle be small compared with the mean energy of the particle [12]. In this case, K being the mean energy of the momentum of the nucleons with respect to the nuclear axis, characterizes the rotation of the nucleus as a whole with respect to the axis of symmetry.

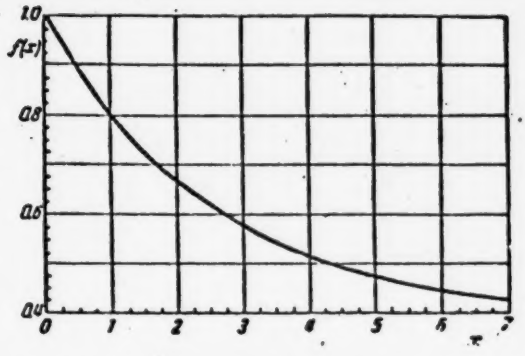

Fig. 2. Fission fragment angle distribution

$$x=\frac{\hbar^2(kR)^2}{2J_zT}\sin^2\vartheta.$$

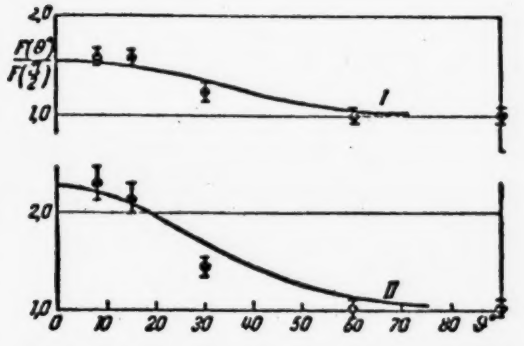

Fig. 3. Fission fragment angle distributions in U^{238} and Th^{232}. I) Curve for U^{238}, E_n = 7.26 Mev, x_0 = = 2.2(2.0); II) Curve for Th^{232}, E_n = 7.15 Mev, x_0 = = 5.7(4.8).

$$W(i)=\sum_{K=0}^{i}a(K)=1. \qquad (4)$$

It will be further assumed that the fission probability for any value of K is proportional to the number of states of the transition nucleus with a given value of K. According to statistical theory the distribution of K in the transition nucleus will have the form (cf. Appendix I):

$$a(K)=\frac{1}{N(i)}\exp\left\{-\frac{B_z}{T}K^2\right\}=\frac{1}{N(i)}\exp\{-\alpha K^2\}, \qquad (5)$$

where B_z is the rotational constant for rotation about the axis of symmetry ($B_z = \hbar^2/2J_z$, where J_z is the component of the moment of inertia with respect to the symmetry axis); T is the effective temperature of the "transition" nucleus and N(i) is a normalization factor which is determined by Equation (3). Replacing the summation over K in Equation (2) by integration, we find:

$$F_i(\vartheta)=\frac{1}{N(i)}\exp\left\{-\frac{\alpha i^2\sin^2\vartheta}{2}\right\}\times I_0\left(\frac{\alpha i^2\sin^2\vartheta}{2}\right), \qquad (6)$$

where I_0 is a Bessel function of imaginary argument. The complete angle distribution is obtained by integrating over all moments which appear in the reaction

$$F(\vartheta)=\int_0^{i_{max}}F_i(\vartheta)\,i\,di, \qquad (7)$$

where $i\,di$ is the probability for capture of a neutron with moment i; $i_{max} \approx kR$ is the maximum moment assigned to a neutron where R is the radius of the target nucleus; and k is the wave vector of the neutron. For charged particles $i_{max} \approx kR\sqrt{1-V/E}$, where V is the energy of the Coulomb barrier and E is the energy of the particle.

The integral in (7) cannot be computed in general form if the normalization condition in (4) is used. For simplicity we shall assume that N(i) = i which, strictly speaking, is only true at small values of αi^2. However, it can be shown that the replacement of the exact normalization condition on a(K) by the approximation results only in a reduction in the contribution at large values of i in the integral in (7); in practice, this effect is not reflected in the angle distribution since it causes only a certain reduction in the parameter $x_0 = \alpha(kR)^2$ of the corresponding anisotropy. Using the approximate normalization condition N(i) = i, the integral in (7) is easily computed:

$$F(\vartheta)=f(x)=\exp\left(-\frac{x}{2}\right)\left[I_0\left(\frac{x}{2}\right)+I_1\left(\frac{x}{2}\right)\right], \qquad (8)$$

where $x = x_0 \sin^2 \vartheta$. The angle distribution (8) is normalized to unity at $\vartheta = 0°$. A graph of the function f(x) is shown in Figure 2.

The angle distribution (8) is symmetric with respect to $\vartheta = 90°$ and has maxima at 0° and 180°. The presence of the maxima in the angle distribution at $\vartheta = 0°$ and 180° is a result of the fact that the distribution a(K) has a maximum at $K = 0$ [8, 9].

In Figure 3 is shown the angle distributions for fission fragments in U^{238} and Th^{232} induced by neutrons with energies of 7.26 and 7.15 Mev respectively. The experimental points pertain to the measurements by Henkel and Brolley [4]. The curves have been plotted from the formula given in (8). The parameter x_0 was determined from the experimental value of the anisotropy $A_n(E_n) = \frac{F(0°)}{F(90°)}$. These values of x_0 are shown in the caption for Figure 3. The values of x_0 obtained with the normalization of a(K) in accordance with Equation (4) are shown in brackets. For $x_0 = 2.0$, α is 0.08.* For T = 0.5 Mev the rotational constant B_Z is found to be approximately 40 kev, which is approximately eight times greater than the value for the moment of inertia of a solid body:

$$(\hbar^2 2I_{z\,\text{solbody}} \sim 5 \text{ kev}).$$

This discrepancy is not to be taken seriously since the moment of inertia should coincide with that of a solid body only at very high degrees of excitation. Since, in point of fact, the excitation energy is not very high, the moment of inertia can be considerably smaller than J_{solbody}, particularly if the "transition" nucleus has a structure which approximates that of a "magic" nucleus (a small number of nucleons outside of closed shells). From this point of view it is also possible to explain qualitatively the difference in the magnitude of the anisotropy in uranium and thorium and also the difference in the energy dependence of the anisotropy in these nuclei; this effect is especially noticeable close to the fission barriers.

In the statistical model the dependence of the fragment anisotropy on the energy of the incoming particle is determined by the energy dependence of the parameter x_0. The increase in anisotropy with energy, which is observed up to neutron energies of approximately 10 Mev, is connected with the increased moment which is imparted to the nucleus in particle capture. The reduction in the anisotropy at higher energies may be related to the increased moment of inertia of the "transition" nucleus. Furthermore, at these energies emissive fission becomes possible (that is, fission after the emission of a neutron); fission due to inelastic scattering of neutrons can also occur. At nucleon energies above 50-60 Mev the nucleus becomes "black." At these energies the onset of nuclear cascade processes occur; in these processes a considerable part of the energy and momentum is carried away by one or several "fast" nucleons. Furthermore, the probability for emissive fission becomes higher. It is clear that in this case the fragment angle distribution will be more isotropic than in the "black-nucleus" case. If, as a result of a nuclear cascade process, a momentum in the direction of the incoming particle is imparted to the nucleus, the fragment angle distribution will exhibit a maximum at $\vartheta = 90°$. The fragment angle distribution in fission induced by high-energy protons has been investigated in References [13, 14].

In addition to the "transition-nucleus" model, there is another possible interpretation of the fragment angle distribution. It may be assumed that the anisotropy is related to the spin dependence of the fragment level density. In fact, a simple statistical analysis indicates that the level density of the nucleus falls off with increasing spin. Hence, the formation of fragments with small spins is more probable in fission. The orbital moment of the fragments $\mathbf{l} = \mathbf{I} - \mathbf{s}$, where $\mathbf{s} = \mathbf{j}_1 + \mathbf{j}_2$, $\mathbf{j}_1$ and $\mathbf{j}_2$ are the spins of the fragments, will be oriented preferentially along the spin of the compound nucleus. This leads to a corresponding angular anisotropy of the fragments. In this case the angle distribution of the fragments is still described by Equation (8) (cf. Appendix II) with the sole difference that, in place of the moment of inertia of the "transition" nucleus in the parameter x_0, we have the moment of inertia of the fragments with respect to the line which connects them: $J_{\text{frag}} = J_1 + J_2$; also, in place of the temperature of the "transition" nucleus we have the fragment temperature. Since the temperature of the fragments is approximately equal to 1.0-1.2 Mev, to obtain the experimental value of the anisotropy it is assumed that in U^{236}, $J_1 + J_2$ is 13-15 times smaller than the sum of the solid-body moments of inertia of the fragments. Furthermore, considering only the statistical distribution for the fragments it is ob-

*This value may be somewhat high since the value of x_0 depends on the choice of $I_{\max}$ and the function W(I).

viously impossible to explain the significant difference in the magnitude of the angular anisotropy in uranium and thorium and the nonmonotonic dependence of the anisotropy on neutron energy close to the fission threshold. On the other hand, it is doubtful that the experimentally observed connection between the anisotropy and fission asymmetry [1, 2, 6, 7] can be explained, considering only the state close to the saddle point. As has been shown by Fong [15], the internal structure of the fragments plays an important role; in asymmetric fission the fragments lie closer to the magic numbers and this may lead to a preference for asymmetric fission. The higher anisotropy in asymmetric fission could also be explained by the smaller magnitude of the moments of inertia in nuclei which are almost magic. From this point of view the reduction in the anisotropy at neutron energies above 10 Mev may be related to the increased contribution due to symmetric fission.

The case of photofission is different in that a small moment is transferred to the nucleus. For dipole quanta and even-even target nuclei the fragment angle distribution is given by the formula [9]

$$F_1(\vartheta) = \sum_{K=0,\pm 1} a(K) |D^1_K|^2, \tag{9}$$

where D^J_{MK} is the matrix of the irreducible representation of the rotation group

$$|D^1_1|^2 = \frac{1}{2}\sin^2\vartheta, \quad |D^1_{\pm 1}|^2 = \frac{1}{2} - \frac{1}{4}\sin^2\vartheta.$$

It is reasonable to suppose that the parameter α in Equation (5) is determined primarily by the excitation energy and is independent of the nature of the incoming particle. For photons with energies ranging from 10 to 15 Mev, which correspond to neutrons with energies from 5 to 10 Mev, $\alpha = 0.1$. The anisotropy in the angle distribution in this case is found to be $A_\gamma = \frac{F(90^\circ)}{F(0^\circ)} \approx 1.05$. Experimentally, one usually observes a considerably larger anisotropy; however, in view of the fact that γ-rays with a continuous spectrum are used, the high anisotropy may be due to fission induced by low-energy quanta. This view is supported by the experiments of Winhold and Halpern [7] which indicate that the anisotropy in the fragment angle distribution in photofission is due to photons with energies which do not exceed threshold by more than 2-3 Mev.

The author wishes to express his gratitude to B.T. Gelikman for a discussion of the work and valuable comments.

APPENDIX

1. Equation (5), which gives the distribution of K, can be obtained directly on the basis of the statistical model of the nucleus. We consider a nucleon gas in an axially symmetric field. In such a field the projection of the moment on the symmetry axis is an integral of the motion. The average value is

$$\overline{K} = \int_0^\infty \int_{-\infty}^{+\infty} d\varepsilon\, dK\, g(\varepsilon, K) f(\varepsilon, K), \tag{10}$$

where $g(\varepsilon, K)$ is the number of states with given K in the energy interval $d\varepsilon$ and $f(\varepsilon, K)$ is the filling function. For free Fermi particles

$$f(\varepsilon, K) = \left\{\exp\left(\frac{\varepsilon - \varepsilon_0 - \gamma K}{T}\right) + 1\right\}^{-1}.$$

where ε_0 is the Fermi energy; T is the temperature; and $\gamma/\hbar$ is the angular velocity.

Expanding $f(\varepsilon, K)$ in a series in γ, we find (with an accuracy to order T/ε_0 and $E_{rot}/A\varepsilon_0$): $\overline{K} = J_z\gamma/\hbar$, where

$$J_z = \hbar^2 \int_{-\infty}^{+\infty} K^2 dK g(\xi_0, K). \tag{11}$$

The moment of inertia can be written in a somewhat different form

$$J_z = \hbar^2 \overline{K^2} / D_0, \tag{11a}$$

where $D_0 = \left[\int_{-\infty}^{\infty} g(\xi_0, K)\, dK \right]^{-1}$ is the mean distance between the nuclear levels close to the ground state

and $\overline{K^2} = D_0 \int_{-\infty}^{\infty} K^2 g(\xi_0, K)\, dK$ is the mean value of K^2 for these states.

Noting further, that $\frac{\partial S}{\partial K} = -\frac{\gamma}{T}$, we find the entropy of the system $S = S_0 - \frac{\hbar^2 K^2}{2 J_z T}$, where S_0 is independent of K.* The distribution of K is determined by the formula

$$a(K) \sim \exp S(K) \sim \exp\left\{ -\frac{\hbar^2 K^2}{2 J_z T} \right\}.$$

For an ideal Fermi gas, Equation (11) gives a value for the moment of inertia which corresponds to the solid-body value; in this case, $\overline{K^2} \approx \frac{1}{\hbar^2} (2m\xi_0 b^2)$, where b is the minor semiaxis of the nucleus. However, in the derivation of this expression, in addition to assuming the quasi-classical motion of the nucleons, it has also been assumed that it is valid to replace the summation over states by an integration over energy. For this assumption to hold, the temperature must be large compared with the distance between the lower levels of the nucleus. In actual nuclei, for excitations $\lesssim$ 10-20 Mev, these quantities are apparently of the same order of magnitude and the quantum numbers are small so that one would expect a considerable deviation in J_z from the solid-body value at such excitations. It is also clear that this departure from the J_z solbody value should increase with increasing proximity to nuclei with closed shells. The interaction between nucleons can also lead to a departure in the moment of inertia from the value J_z solbody. Equation (11a) reflects the dependence of J_z on D_0 and the structure of the first levels in a qualitative fashion. Hence, smaller values of $\overline{K^2}$ correspond to smaller values of the moment of inertia.

2. The density of fragment states with a given value of the total spin $s = j_1 + j_2$ is

$$\rho(s) = \int [\rho_1(j_1)\, \rho_2(j_2)]\, |_{s = \text{const}}\, dj_1 dj_2,$$

where $\rho(j)$ is the density of levels in a fragment with spin j. On the statistical theory $\rho(j)$ is given by the expression $\rho(j) = \rho_0 \exp(-\alpha j^2)$, where $\alpha = \hbar^2/2JT$; J is the moment of inertia; and T is the temperature of the fragment (it is assumed that $j \gg 1$).

After integration over j_1 and j_2 we have

$$\rho(s) \sim \exp\left\{ -\frac{a_1 a_2}{a_1 + a_2} s^2 \right\} = \exp\left\{ -\frac{\hbar^2 s^2}{2(J_1 + J_2) T} \right\} \quad (T_1 = T_2 = T). \tag{12}$$

The distribution of the projection of the vector s along the fission-flight direction in conjunction with the distribution of the projection of I in this direction (K) gives the formula (the projection of the orbital moment in

*This method was used by Bethe [16] for deriving the statistical expression for the level density associated with a given momentum.

the fragment-flight direction is zero)

$$\rho_{\text{frag}}^{(K)} = \int_{K}^{\infty} \rho(\varepsilon)\, d\varepsilon \sim \exp\left\{-\frac{\hbar^2 K^2}{2(J_1+J_2)T}\right\}.$$

This expression coincides with the distribution given in (5); hence, on the basis of a calculation similar to that presented above we obtain Equation (8) in which $J_z = J_1 + J_2$ and T is the temperature of the fragments. For zero spin of the target nucleus of the fragment-angle distribution can be written in the form [9]

$$F(\vartheta) \sim \sum_{K=0}^{l} a(K) |D_{0K}^{l}|^2 \sim \sum_{K} a(K) |Y_{l,K}(\vartheta)|^2.$$

The function in (1) is an analog of the quantum-mechanical distribution $|Y_{l,K}|^2$, where $Y_{l,K}$ is the spherical harmonic. Hence, the use of Equation (2) is not connected with the particular fission model. Equation (8) can also be obtained in another way by considering directly the angle distribution of particles with orbital moments distributed in accordance with Equation (12), taking $s = l - L$

LITERATURE CITED

[1] B.L. Cohen, W.H. Jones, G.H. McCormick and B.L. Ferrell, Phys. Rev. 94, 625 (1954).

[2] B.L. Cohen, B.L. Ferrell-Bryan, D.J. Coombe and M.K. Hullings, Phys. Rev. 98, 685 (1955).

[3] J.E. Brolley and W.C. Dickinson, Phys. Rev. 90, 388 (1953); 94, 640 (1954); J.E. Brolley, W.C. Dickinson and R.L. Henkel, Phys. Rev. 99, 159 (1955).

[4] R.L. Henkel and J.E. Brolley, Phys. Rev. 103, 1292 (1956).

[5] E.J. Winhold, P.T. Demos and I. Halpern, Phys. Rev. 85, 728 (1952); 87, 1139 (1952).

[6] A.W. Fairhall, I. Halpern and E.J. Winhold, Phys. Rev. 94, 733 (1954).

[7] E.J. Winhold and I. Halpern, Phys. Rev. 103, 990 (1956).

[8] A. Bohr, On the Theory of Nuclear Fission (Report No. 911 presented by the Danish Delegation to the International Conference on the Peaceful Use of Atomic Energy, Geneva 1955). See also, Prob. Contem. Phys. 1 (1956).

[9] V.M. Strutinsky, J. Exptl. Theoret. Phys. 30, 606 (1956).

[10] D.M. Chase and L. Wilets, Phys. Rev. 103, 1296 (1956).

[11] J. Wheeler, J. Atomic Energy 5, 71 (1956).*

[12] L.D. Landau and E.M. Lifshitz, Statistical Physics, Chapt. III.(State Tech. Press, Moscow 1951).

[13] O.V. Lozhkin, N.A. Perfilov and V.G. Shamov, Proc. Acad. Sci. USSR 103, 407 (1955).

[14] R.L. Wolke, Phys. Rev. 98, 1199 (1955).

[15] P. Fong, Phys. Rev. 102, 434 (1956).

[16] H. Bethe, Nuclear Physics, Chapt. II (State Tech. Press, Moscow 1948).

Received October 27, 1956

*[Original Russian pagination. See C.B. Translation pagination.]

BLANK
PAGE

RESONANCE SCATTERING OF γ-RAYS IN Mg^{24}

N.A. Burgov and Yu.V. Terekhov

Resonance scattering of γ-rays with energies $E_{\gamma_1} = 1.38$ Mev, corresponding to the transition to the ground state in Mg^{24}, have been observed in metallic magnesium. The energy given off by the γ-ray ($E_{\gamma_1} = 1.38$ Mev) in emission and collision with the nucleus, is compensated for by the energy obtained due to recoil associated with the emission of the preceding γ-ray with an energy $E_{\gamma_2} = 2.76$ Mev. Using a fast coincidence method and amplitude discrimination, coincidences were recorded between the γ-rays with energies $E_{\gamma_1} = 1.38$ Mev and $E_{\gamma_2} = 2.76$ Mev. Scatterers of magnesium and aluminum were alternately placed in the path of the 1.38 Mev γ-rays. The source was radioactive Na^{24} in a water solution of NaOH. At an angle of 120° between the γ-rays a strong attenuation of the 1.38 Mev γ-rays was observed; this is attributed to resonance scattering. When the angle between the γ-rays was varied by 5°, the strong attenuation of the flux disappeared. The width of the level at 1.38 Mev in Mg^{24} has been estimated at $\Gamma > 1.6 \cdot 10^{-4}$ Mev.

INTRODUCTION

Resonant fluorescence radiation is a well-known process in atomic physics. The analogous process – resonance scattering on nuclei – should exist and should be observed in the emission of γ-rays by excited nuclei.

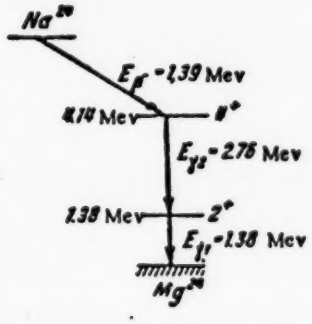

Fig. 1. Decay scheme for Na^{24}.

The cross section for resonance scattering can be given as follows [1]:

$$\sigma(E_\gamma) = 4\pi\lambda^2 \cdot \frac{2j+1}{2i+1} \cdot \frac{1}{1+\frac{(E_\gamma - E_r)^2}{\left(\frac{\Gamma}{2}\right)^2}}, \qquad (1)$$

where E_γ is the energy of the γ-rays; E_r is the energy of the level at which scattering is observed; λ is the wave length of the γ-rays; j is the moment associated with the excited level; i is the moment of the ground state of the nucleus; and Γ is the natural width of the excited level.

If the cross section at resonance is designated by

$$\sigma_0 = 4\pi\lambda^2 \frac{2j+1}{2i+1}, \qquad (2)$$

for nuclei the levels of which have moments characterized by $j = 2$ and $i = 0$, we have

$$\sigma_0 = \frac{2.448 \cdot 10^{-20}}{E_\gamma^2} \text{ cm}^2, \qquad (3)$$

where E_γ is expressed in Mev.

The observation of resonance scattering of γ-rays on nuclei is made difficult by the fact that in emission and scattering of γ-rays by a given nucleus part of the energy goes into recoil of the nucleus and the γ-rays are absorbed at energies smaller than that required for excitation of the same nucleus to its first level E_τ.

As has been shown in Reference [2] this energy decrement is

$$\Delta E_\tau = E_\tau - E_r = -\frac{E_\tau^2}{Mc^2}, \tag{4}$$

where M is the mass of the nucleus and c is the velocity of light. In nuclei the quantity ΔE_γ is of the order of several electron volts.

According to an estimate given by Weisskopf [3] the first nuclear levels are characterized by a width Γ of the order 10^{-3}-10^{-5} ev. It is clear from these considerations that the cross section for resonance scattering of γ-rays on nuclei, as calculated from Equation (1), is very small. For the nucleus Na^{24}, which decays according to the scheme shown in Figure 1, this cross section is $\sigma \sim 10^{-29}$ cm^2. With this small value of the cross section it is difficult to detect the effect in question against the background of Compton scattering.

To obtain a noticeable effect in resonance scattering it is necessary to somehow compensate for the low energy of the γ-rays, corresponding to the transition to the ground state; this effect can be achieved by using the Doppler shift to cause an energy change.

Description of the Experimental Method and the Apparatus

In the nucleus Na^{24} and a number of other nuclei which emit electrons and cascade γ-rays, the small energy can be compensated by the energy acquired due to recoil of the γ-rays and electrons which are emitted prior to the event in question.

We neglect the recoil due to the emission of the electron and neutron in β-decay and assume that the resulting nucleus is found at rest. We assume further that it emits cascade γ-rays. As a result of the emission of a γ-ray with an energy E_{γ_2}, corresponding to the transition to the first excited level, the nucleus acquires a velocity $\underline{v}$. If the axis Ox is taken in the direction of the emission of the subsequent γ-ray, which is characterized by an energy E_{γ_1}, corresponding to the transition to the ground state (cf. Figure 1) and v_x is the component of the nuclear velocity along the Ox-axis, then

$$v_x = \frac{E_{\gamma_2}^0}{Mc^2}\cos\varphi \tag{5}$$

and

$$E_{\gamma_1} = E_{\gamma_2}^0 \frac{1+\frac{v_x}{c}}{\sqrt{1-\frac{v^2}{c^2}}}, \tag{6}$$

where $E_{\gamma_1}^0$ and $E_{\gamma_2}^0$ are the energies of the γ-rays emitted by the nuclei at rest; E_{γ_1} is the energy of the γ-ray emitted by the moving nucleus; φ is the angle between the emitted cascade γ-rays. If we require that the energy E_{γ_1} be exactly equal to the energy E_τ required for the excitation of the nucleus to its first level, following several elementary manipulations of Equations (5) and (6), we obtain the compensation condition for the cascade γ-rays,

$$\cos\varphi_0 = -\frac{E_{\gamma_1}^0}{E_{\gamma_2}^0}. \tag{7}$$

In the case of Na^{24}-decay, $E_{\gamma_1}^0 = 1.38$ Mev, $E_{\gamma_2}^0 = 2.76$ Mev and $\varphi_0 = 120°$

Thus, to compensate for the inadequate energy the recoil due to the emission of the preceding γ-quantum must satisfy the following: a) the energy of the preceding γ-quantum must be larger than the energy of the γ-

quantum which characterizes the transition to the ground state; b) the angle between the emitted γ-rays must correspond to the compensation condition given in (7).

If the recoil due to the emission of the electron is included, the compensation condition can be written in the form

$$\cos\alpha = -\frac{E^0_{\gamma_2}}{(P_\beta)_{max}\cdot c}, \qquad (8)$$

where α is the angle between the direction of emission of the electron and the γ-ray; $(P_\beta)_{max}$ is the momentum of the maximum-energy electron.

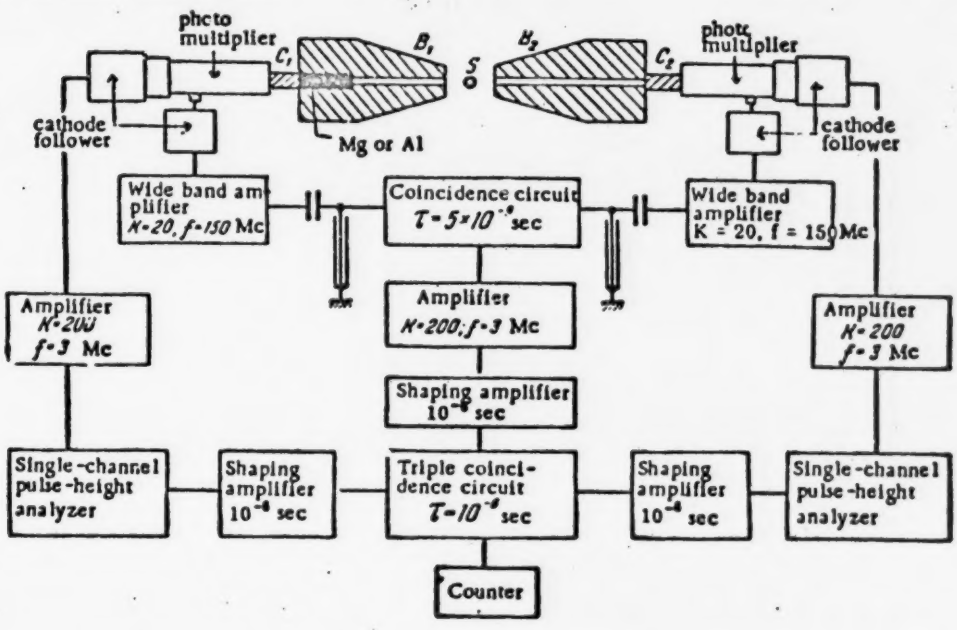

Fig. 2. Block diagram of the apparatus: S) γ-ray source; B_1 and B_2) lead collimators; C_1 and C_2) toluene crystals; PEM) PEM-19M photomultiplier; CF) cathode followers.

In the work being reported here an investigation was made of the resonance scattering of γ-rays with energies $E_{\gamma_2} = 1.38$ Mev, emitted by the excited level of Mg^{24} after β-decay of Na^{24}.

A block diagram of the apparatus is shown in Figure 2. On a rotating table were set two lead collimators with γ-ray detectors consisting of a PEM-19M photomultiplier with a toluene crystal.

The γ-ray source was radioactive Na^{24} in a NaOH solution in water, deposited in a quartz ampoule of cylindrical shape 10 mm in diameter and 70 mm high.

Coincidences between γ-rays emitted from the source with an angle φ between the lines of flight were recorded. One of the collimators and its detector could be moved about the axis of the source, thereby changing the angle φ.

The pulse from each detector was fed to a "fast" coincidence circuit with a resolving time of $5\cdot10^{-9}$ sec and also to a single-channel pulse-height analyzer which was adjusted to the energy of the Compton peak of the corresponding γ-quantum. From the analyzer and the "fast" coincidence circuit, the pulses were fed to a "slow" triple-coincidence circuit with a resolving time of 10^{-6} sec; the coincidences were then fed to a counter.

In the path of the counter which recorded the γ-rays with energies $E_{\gamma_2} = 1.38$ Mev, emitted in the transition to the ground state of a nucleus, there was placed a scatterer composed of the same nuclei as those emit-

ting the γ-rays, that is, magnesium. When the compensation condition (7) is fulfilled there should be observed an increase in the ejection or scattering of γ-rays from the beam due to resonance scattering in the magnesium sample. In a scatterer with other nuclei (for instance aluminum) the resonance scattering should not occur. The length of the magnesium scatterer was 60 mm. The length of the aluminum scatterer was chosen so as to make the counting rate (in the region of angle in which there was no resonance scattering) the same in both cases.

The need for the collimators was dictated by the fact that the angle interval between the γ-rays, in which one can hope to observe the effect, is small (of the order of 1-3°, as will be shown later). Because of the geometric requirements, the detectors (toluene crystals) were narrow parallelopipeds with the dimensions 60 x 10 x 30 mm³.

We now analyze in greater detail the angle problem. Because of the thermal motion of the nuclei in the radiator as well as in the scatterer, the mean effective cross section for resonance scattering can be written in the form

$$\sigma = \sigma_0 \Psi(\xi, x), \tag{9}$$

where the function $\Psi(\xi, x)$, which gives the shape of the line, is determined as in Reference [4]:

$$\xi = \frac{\Gamma}{\Delta}; \quad x = \frac{E_\gamma - E_r}{\frac{\Gamma}{2}}.$$

The Doppler width of the line Δ is given by the expression

$$\Delta = E_{\gamma_1} \sqrt{\frac{2k(T_1 + T_2)}{Mc^2}}, \tag{10}$$

where T_1 is the absolute temperature of the source; T_2 is the absolute temperature of the absorber; and k is the Boltzmann constant.

It is easily shown that $\Delta \gg \Gamma$; hence, the cross section assumes the form

$$\sigma = \sigma_0 \frac{\sqrt{\pi}}{2} \cdot \frac{\Gamma}{\Delta} \cdot \exp\left[-\frac{(E_{\gamma_1} - E_r)^2}{\Delta^2} \right]. \tag{11}$$

The energy of the γ-rays, E_{γ_1}, depends on the angle φ as follows:

$$E_{\gamma_1} = E^0_{\gamma_1} \left(1 + \frac{E^0_{\gamma_1}}{Mc^2} \cos\varphi \right). \tag{12}$$

At the same time, From Equation (4) we have

$$E_r = E^0_{\gamma_1} \left(1 + \frac{E^0_{\gamma_1}}{Mc^2} \right). \tag{13}$$

Thus, as a function of the angle φ between the γ-rays, the cross section for resonance scattering is given by

$$\sigma = \sigma_0 \frac{\sqrt{\pi}}{2} \cdot \frac{\Gamma}{\Delta} \times \exp\left[-\frac{(E^0_{\gamma_1})^2}{\Delta^2} \left(\frac{E^0_{\gamma_1}}{Mc^2} \cos\varphi - \frac{E^0_{\gamma_1}}{Mc^2} \right)^2 \right]. \tag{14}$$

When the compensation conditions given in (7) are satisfied the cross section is a maximum and is equal to

$$\sigma_{max} = \sigma_0 \frac{\sqrt{\pi}}{2} \cdot \frac{\Gamma}{\Delta}. \quad (15)$$

If we denote by $\varphi_1 = \varphi - \varphi_0$ the departure of the flight angle of the γ-rays from the angle corresponding to the compensation condition and assume that this departure is small, we have

$$\sigma = \sigma_{max} \cdot \exp\left[-\frac{(E^0_{\gamma 1})^2}{\Delta^2}\left(\frac{E^0_{\gamma 2} \sin \varphi_0}{Mc^2} \varphi_1\right)^2 \right]. \quad (16)$$

The angular width of the line Δ_φ and the cross section for resonance scattering σ are determined by the expressions:

$$\Delta_\varphi = \frac{\Delta}{E^0_{\gamma 1}} \cdot \frac{Mc^2}{E^0_{\gamma 2} \sin \varphi_0} = \frac{\Delta}{E^0_{\gamma 1}} \frac{Mc^2}{\sqrt{(E^0_{\gamma 2})^2 - (E^0_{\gamma 1})^2}}, \quad (17)$$

$$\sigma = \sigma_{max} \cdot \exp\left[-\frac{\varphi_1^2}{\Delta_\varphi^2} \right]. \quad (18)$$

For Mg^{24}, $\Delta_\varphi = 1° 8'$. Using the estimate given by Weisskopf for Γ, we obtain, for Mg^{24}

$$\sigma_{max} = 0{,}66 \cdot 10^{-24} \text{ cm}^2.$$

EXPERIMENTAL RESULTS

Measurements were made of the ratio A_k, the number of coincidences with the magnesium scatterer inserted N_{Mg} to the number of coincidences with the aluminum scatterer inserted N_{Al} at the angles φ shown in the table.

In the table are shown the mean-square errors. The mean counting rate for coincidences was 15 counts per minute.

In Figure 3 are shown the results obtained by adjusting for aluminum and magnesium scatterers of the same weight. The minimum in the curve corresponds to the maximum due to resonance scattering of γ-rays at 1.38 Mev.

To determine the ratio of the number of true coincidences to the number of accidental coincidences a length of coaxial cable was inserted in one of the channels; this arrangement produced a delay which was considerably greater than the resolving time of the coincidence circuit. Using these measurements the mean ratio of the number of true coincidences to the number of accidental coincidences (with the sample inserted) was obtained

$$\frac{N_{true}}{N_{accident}} = 0.87 \pm 0.02. \quad (19)$$

As a check control experiments were undertaken in which the scattering of the 2.76 Mev γ-rays in magnesium and aluminum scatterers were measured. A determination was made of the ratio of the number of coincidences with the magnesium scatterer to the number of coincidences with the

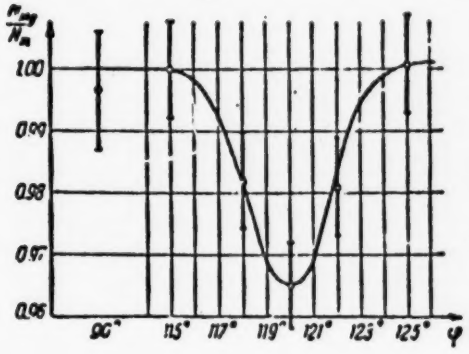

Fig. 3. Curve showing resonance scattering of γ-rays in Mg^{24}.

aluminum scatterer at 90° and 120°. In both cases this quantity was found to be $A_k = 1.01 \pm 0.01$. A reduction corresponding to resonance scattering was not observed. To check on the operation of the apparatus from time to time correlation curves were run for Ni^{60} and Mg^{24}. In both cases the form of the correlation curves within the limits of the experimental error corresponded to those which had been calculated theoretically.

Analysis of the Experimental Results. Conclusions

If we denote the experimentally determined transmission of the magnesium sample and the aluminum sample by

$$T_{Mg} = \frac{N_{Mg}}{N}; \quad T_{Al} = \frac{N_{Al}}{N}, \tag{20}$$

where N is the number of coincidences without the scatterer, then $T_{Mg} = T_{Mg,a} \cdot T_{Mg,r}(\varphi)$; $T_{Al} = T_{Al,a}$, where T_a is the transmission of the sample for normal scattering and absorption of the γ-rays and T_r is the transmission of the sample for resonance scattering of γ-rays.

In view of the fact that experimentally one measures both the true and random coincidences,

$$\frac{N_{Mg}}{N_{Al}}(\varphi) = \frac{T_{Mg,a}}{T_{Al,a}} \cdot \frac{[2N_0\tau + T_{Mg,r}(\varphi)]}{2N_0\tau + 1} \tag{21}$$

where N_0 is the number of decay events in the source per unit volume and τ is the resolving time of the coincidence circuit.

However, since $\frac{N_{true}}{N_{accident}} = \frac{1}{2N_0\tau}$,

$$\frac{T_{Mg,a}}{T_{Al,a}} = \frac{N_{Mg}}{N_{Al}}(90°), \tag{22}$$

and from (21) we obtain the transmission of the magnesium sample for resonance scattering.

$$T_{Mg,r}(120°) = 0{,}934 \pm 0{,}017. \tag{23}$$

Since the angle interval selected by the apparatus is larger than the angular width of the line Δ_φ, in the experiment we actually average the transmission and the experimental quantity does not correspond to the magnitude of the cross section calculated from Equation (15). The calculation of the geometric corrections is given in the Appendix.

The experimentally observed transmission is close to unity and its value can be given in the form

$$T_{Mg,r} = 1 - n_{Mg}\overline{\sigma_{Mg,r}}d_{Mg}, \tag{24}$$

where $\overline{\sigma_{Mg,r}}$ is the cross section for resonance scattering averaged over solid angle; n_{Mg} is the number of Mg^{24} nuclei per unit volume of the scatterer; and d_{Mg} is the thickness of the magnesium scatterer.

From Equation (24) and Equation (III) of the Appendix we can obtain the cross section for resonance scattering at the maximum

$$\sigma_{max} = \frac{1}{0{,}55}\overline{\sigma_{Mg,r}} = (0{,}61 \pm 0{,}15) \text{ barns} \tag{25}$$

The assumptions taken as a basis for deriving Equation (15) are not completely fulfilled in the case being considered. Hence, the value σ_{max} cannot be used without reservations in calculating the width of the level Γ at 1.38 Mev in Mg^{24}. Actually, we assume: a) there is no recoil due to β-decay; and b) free motion of the recoil nucleus after the emission of the 2.76 Mev γ-ray.

Taking into account the recoil due to β-decay causes the sharp maximum in the cross section for reson-

ance scattering to become smeared. Furthermore, the motion of the recoil nucleus in a liquid can certainly not be taken as free.

Thus, the observed cross section for resonance scattering is due to nuclei which a) successfully lose the recoil obtained by β-decay during the lifetime of the level at 4.4 Mev (or else this recoil is small), and b) do not change the direction of motion during the lifetime of the level at 1.38 Mev in Mg^{24}.

Since the recoil due to β-decay and slowing-down of the nucleus can only diminish the effect, using the value of σ_{max} which has been obtained and Equation (15) it is possible only to set a lower limit on the width of the level

$$\Gamma > 1{,}6 \cdot 10^{-4} \text{ ev}$$

APPENDIX

Calculation of the Geometric Corrections

The dependence of the cross section for resonance scattering on the angle between the γ-rays is given by Equation (18). We average the scattering cross section over solid angle and calculate this quantity for a point at the center of the source

$$\overline{\sigma_{Mg,\,r}} = \frac{1}{\omega_1 \omega_2} \int \sigma_{max} \exp\left(-\frac{\varphi_1^2}{\Delta_\varphi^2}\right) d\Omega_1\, d\Omega_2, \tag{I}$$

where ω_1 and ω_2 are the solid angles subtended by the detectors at the first and second collimators by a point at the center of the source. We introduce a coordinate system with origin at the center of the source and Oz axis directed perpendicularly to the plane containing the motion of the γ-quanta. Let a_1 and a_2 be the angular half widths of the slits in the plane xy; b_1 and b_2 the angular half widths of the slits in the direction Oz; α_1, α_2, β_1, β_2 are the corresponding values of the solid angles calculated from the axes of the first and second counters.

Since all angles are small and

$$a_1 \ll b_1; \quad a_2 \ll b_2,$$

we have

$$\omega_1 = 4a_1b_1; \quad \omega_2 = 4a_2b_2;$$
$$d\Omega_1 = d\alpha_1 \cdot d\beta_1; \quad d\Omega_2 = d\alpha_2 \cdot d\beta_2$$

and

$$\overline{\sigma_{Mg,\,r}} = \frac{\sigma_{max}}{16 a_1 a_2 b_1 b_2} \int_{-a_1}^{a_1} d\alpha_1 \int_{-b_1}^{b_1} d\beta_1 \int_{-a_2}^{a_2} d\alpha_2 \times \int_{-b_2}^{b_2} \exp\left(-\frac{\varphi_1^2}{\Delta_\varphi^2}\right) d\beta_2. \tag{II}$$

It is obvious that (to an accuracy including second-order terms) the angle φ_1 in these variables is

$$\varphi_1 = \varphi - \varphi_0 = \alpha_1 + \alpha_2 + \operatorname{ctg}\varphi_0 \frac{\beta_1^2 + \beta_2^2}{2} + \frac{\beta_1\beta_2}{\sin\varphi_0}.$$

The integral I in (II) can be calculated numerically.

In the present case $a_1 = a_2 = 0.025$; $b_1 = b_2 = 0.13$ and the integral $I = 0.55$. Whence

$$\overline{\sigma_{Mg,\,r}} = 0{,}55\,\sigma_{max}. \tag{III}$$

LITERATURE CITED

[1] K. Siegbahn, Beta and Gamma Spectroscopy (North-Holland Publishing Company, Amsterdam 1955), p. 521.

[2] E. Pollard and D. Altburger, Phys. Rev. 74, 926 (1948).

[3] V.F. Weisskopf, Phys. Rev. 83, 1073 (1951).

[4] H. Bethe, Nuclear Physics, Chapt. II (State Tech. Press, Moscow 1950), p. 139.

Received January 26, 1957

FORMATION OF POROSITY IN URANIUM UNDER THE ACTION OF THERMAL CYCLING

A.A. Bochvar and G.I. Tomson

In accelerated thermal cycling with a cycle of 50 sec period, considerable changes appear in uranium after 50-1000 cycles, depending upon the temperature range of the cycle. Cycling in the temperature range of the α-phase (with heating up to between 550 and 600°C) produces in textured uranium (containing about 0.1% carbon) a directional deformation and porosity, accompanied by a drop in density. After 5000 cycles, the drop in density amounts to 8%. Thermal cycling with $\alpha \rightleftharpoons \beta \rightleftharpoons \gamma$-transformations produces a pronounced distortion of the original shape of uranium specimens and intense porosity formation, with a considerable drop in density, which attains 30% after 1000 cycles.

In connection with the problem of heat resistance and developments in nuclear engineering, increasing importance attaches to the study of the behavior of metals under the action of thermal cycling.

It is known that uranium, possessing well pronounced anisotropy of its physicomechanical properties, undergoes dimensional and structural changes when subjected to repeated heating and cooling [1, 2]. The character and magnitude of these changes depend upon the preparation of the specimen. In addition, the magnitude of the changes is influenced by the parameters of thermal cycling: upper and lower temperatures of the cycle, rate of heating and cooling, time of exposure to the upper temperature and also the number of cycles.

In the present work, an investigation was made of the behavior of uranium on thermal cycling with a period of 50 sec in the temperature range of the α-phase and also in the temperature range comprising the α-β-γ-transformations.

Brief Description of Method of Thermal Cycling

The specimens were heated by the induction method using a high-frequency apparatus with tube generator. For producing the thermal cycles, the grid circuit of the generator tube included a relay which closed and opened the circuit after predetermined time intervals. For all the specimens, heating was continued for 32 sec and cooling for 18 sec, without delays at the upper and lower cycle temperatures. The number of cycles was recorded by a mechanical counter.

In view of the high chemical activity of uranium at elevated temperatures, the specimens were usually sealed in quartz ampoules in a vacuum of the order of $1 \cdot 10^{-3}$ mm Hg.

In some cases of thermal cycling in the temperature range of the α-phase, which will be discussed separately, the ampoules containing the specimens were filled with helium at a pressure of 1.3 atmos. All other experimental conditions remaining the same, the use of helium, due to the high thermal conductivity of the latter, had the effect of reducing the lower temperature of the cycle and altering the rates of heating and cooling of the specimens.

In thermal cycling in the α-phase range, the specimens were heated to 550-600°C, and the ampoules with the specimens cooled in running water; in cycling with phase transformations, the specimens were heated to 800°C and the ampoules with the specimens were cooled in air.

Thermal Cycling of Uranium in the Temperature Range of the α-Phase

The specimens in the form of cylinders of diameter 4-5 mm and length 4-5 mm were machined from rod extruded at 650°C with a compression of 90%, the direction of the longitudinal axis of the specimens coinciding with the extrusion direction. The uranium contained about 0.1% carbon.

Change in Dimensions of Uranium Specimens on Thermal Cycling in the α-Phase Range

No. of specimen	Length of specimen: original length l_0, mm	Length of specimen: final length l_f, mm	Length of specimen: change in length $\Delta l = \frac{l_f - l_0}{l_0} \cdot 100$ %	Diameter of specimen: original diameter d_0, mm	Diameter of specimen: final diameter d_f, mm	Diameter of specimen: change in diameter $\Delta d = \frac{d_f - d_0}{d_0} \cdot 100$ %	No. of cycles	Duration of test, hours
1	4.02	4.26	6.0	4.11	4.02	−2.2	250	3.5
2	4.03	4.78	18.5	4.11	3.94	−4.1	500	7.0
3	4.00	4.89	22.0	4.11	3.86	−6.1	1000	14.0
4	4.07	5.30	31.0	4.06	3.77	−7.1	2000	28.0

Remarks: 1. Conditions of thermal cycling: heating to 550-600°C – 32 sec; cooling – 18 sec. 2. The changes in dimensions shown cannot be used for calculating the density because a high value would be obtained for the volume, due to the roughness of the specimens.

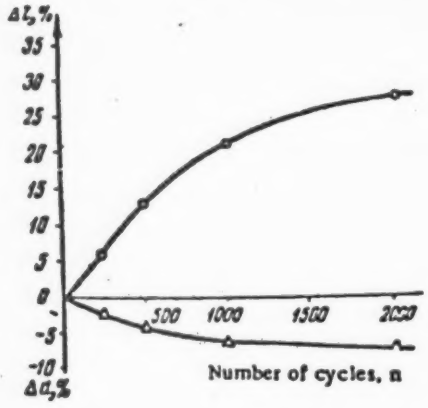

Fig. 1. Influence of number of cycles on change in length (Δl%) and diameter (Δd%) of uranium specimens having a preferred orientation.

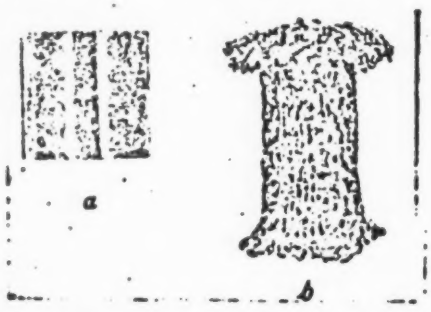

Fig. 3. External appearance of uranium specimen with preferred orientation (a) before and (b) after 5000 thermal cycles in helium in the range 100-550°C (x 4.5).

Fig. 2. External appearance of uranium specimens with preferred orientation before and after thermal cycling in the α-phase range (x2). a) Specimen not subjected to thermal cycling; b, c, d, e) specimens after 250, 500, 1000 and 2000 cycles, respectively.

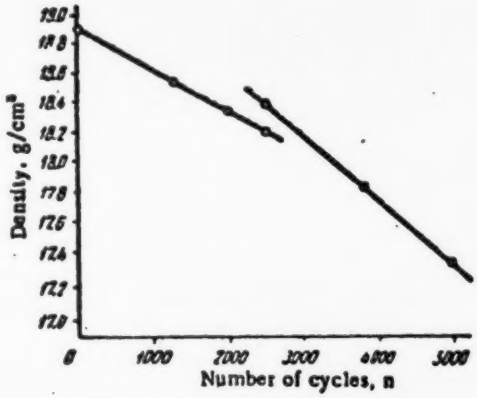

Fig. 4. Influence of number of cycles on density of uranium specimen during thermal cycling in helium in the range 100-500°C. The interruption at 2500 cycles is due to the removal of a friable surface layer from the specimen in the preparation of the polished section.

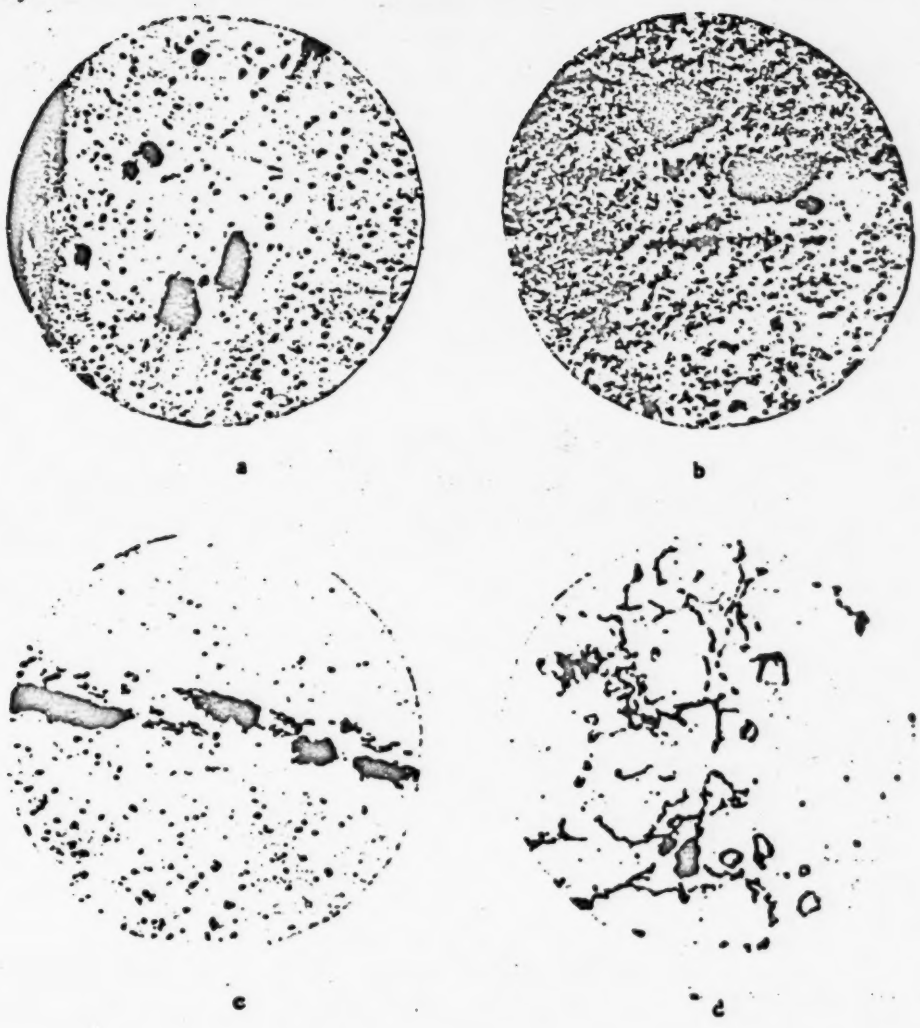

Fig. 5. Formation of porosity in uranium on thermal cycling in helium in the range 100-550°C: a) pores after 1000 cycles (x70); b) pores after 1000 cycles, etched specimen (x115); c) pores and microscopic cracks after 5000 cycles (x115); d) microscopic cracks after 5000 cycles (x600).

The dimensions of the specimens changed on thermal cycling.

The experimental results are shown in the table and Figure 1 shows graphically the dependence of the change in dimensions of the specimens upon the number of cycles.

Figure 2 shows the external appearance of the specimens before and after thermal cycling.

As will be seen from the data given, on thermal cycling in the above-mentioned conditions, considerable deformation occurs in uranium specimens in the direction of the previous working of the metal, this deformation attaining +31% after 2000 cycles (28 hours). In addition, a reduction in density on cycling was observed; after 2000 cycles, this reduction was 0.5%.

In the case of specimens which were in a helium atmosphere during thermal cycling, some distortion of

the geometrical shape was observed in addition to the "growth" (Figure 3), this distortion increasing with the number of cycles; the drop in density was also greater (Figure 4). Thus, after 2000 cycles, the reduction in density was already 3% and after 5000 cycles it was 8%.

When these specimens were examined metallographically, pores and microscopic cracks were seen (Figure 5).

Thermal Cycling of Uranium with $\alpha \rightleftharpoons \beta \rightleftharpoons \gamma$-Transformations

The specimens in the form of cylinders of diameter 5 mm and length 5 mm were machined from rod extruded in the γ-phase range and oil-quenched. The uranium contained about 0.1% carbon.

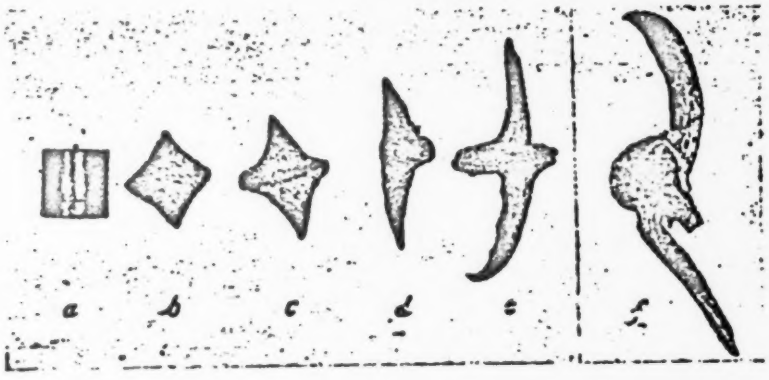

Fig. 6. External appearance of uranium specimens before and after thermal cycling with $\alpha \rightleftharpoons \beta \rightleftharpoons \gamma$-transformations (×2.4): a) specimen not subjected to thermal cycling; b, c, d, e, f) specimens after 50, 100, 187, 250 and 1000 cycles, respectively.

The number of cycles varied from 50 to 1000.

Considerable distortion of the original shape of the specimens occurred on thermal cycling. Figure 6 shows the external appearance of uranium specimens after various numbers of cycles. At the same time as the distortion of the shape, porosity formation was observed accompanied by a reduction in density. The photomicrographs (Figure 7) illustrate the formation and development of pores. It is clear from these figures that an increase in the number of cycles is accompanied by an increase in the area occupied by the pores. In addition, there is a change in shape of the pores; after 50 cycles, the cross section of the pores in the plane of the polished section is circular; after 250 cycles it is elliptical. It is characteristic that the pores are deformed in the direction of "growth" of the specimen. This is well seen in Figure 8 showing at low magnification the distribution of the pores in a specimen after 250 cycles.

Figure 9 shows plots characterizing the process of formation and development of porosity in uranium on thermal cycling with phase transformations. The curves were constructed from the data of a distribution series obtained by the method of quantitative metallography [3]. The measurements were made on mechanically polished specimens.

The number of pores per unit area of polished section N' was determined by means of the formula

$$N' = \frac{\sum_1^p N_p}{p \cdot \frac{\pi d_p^2}{4}},$$

where p is the number of fields of view; $\sum_1^p N_p$ is the total number of pores counted in the fields of view and

Fig. 7. Formation of porosity in uranium on thermal cycling with $\alpha \rightleftharpoons \beta \rightleftharpoons \gamma$-transformations. Unetched specimens: a) starting condition of specimen (×200); b, c, d, e) specimens after 50, 100, 250 and 1000 cycles, respectively (×86).

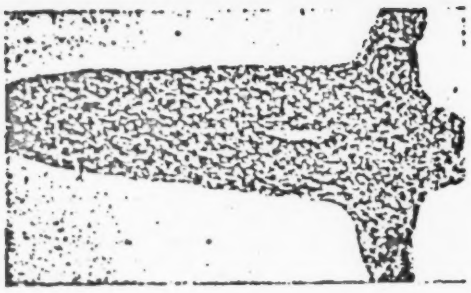

Fig. 8. Distribution of pores in surface of polished specimen of uranium after 250 cycles with $\alpha \rightleftharpoons \beta \rightleftharpoons \gamma$-transformations, specimen electrolytically polished (×10).

d_p is the diameter of a field of view in mm.

The area of the pores per unit area of polished section, i.e., the relative area of the pores S', was determined in a similar manner:

$$S' = \frac{\sum_1^p S_p}{p \cdot \frac{\pi d_p^2}{4}},$$

where $\sum_1^p S_p$ is the total area of the pores counted in the fields of view in mm².

The statistical curves of Figures 9 and 10 were constructed on the basis of $p = 25$ for $d_p = 0.5$ mm.

Figure 10 shows the change in density of specimens on thermal cycling (the curve was constructed on the basis of data obtained by hydrostatic weighing). The plot also shows a curve characterizing the dependence of the volume of the pores formed upon the number of cycles; in constructing this curve, it was conditionally assumed that the dimension of a pore in a direction perpendicular to the surface of the polished section was equal to the observed width of the pore. As will be seen in Figure 10, the statistical data correspond to the data obtained by direct measurement of the density, and characterize in an identical manner the process of porosity formation in uranium on thermal cycling.

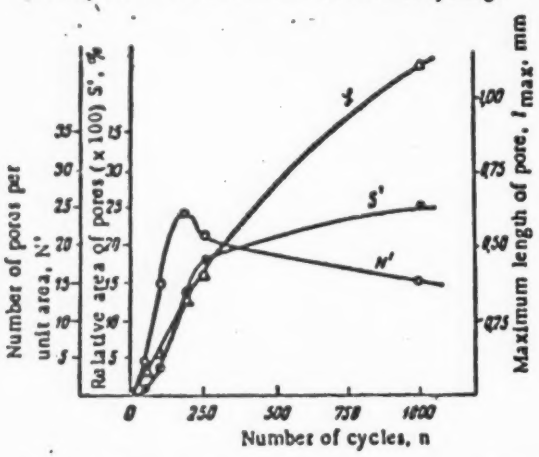

Fig. 9. Influence of number of cycles on porosity of uranium specimen on thermal cycling with $\alpha \rightleftharpoons \beta \rightleftharpoons \gamma$-transformations.

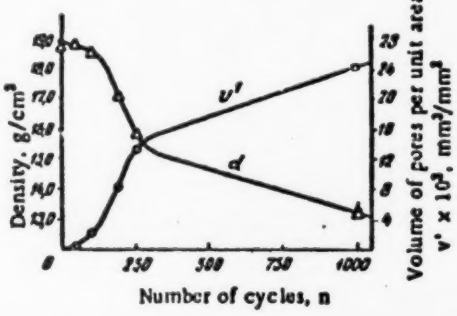

Fig. 10. Influence of number of cycles on density and porosity of uranium specimen on thermal cycling with $\alpha \rightleftharpoons \beta \rightleftharpoons \gamma$-transformations.

The reduction in the number of pores with increase in number of cycles (Figure 9), accompanied by a continued diminution in density (Figure 10), may be due to coalescence of the pores during thermal cycling.

SUMMARY

Substantial changes occur in uranium during rapid, repeated temperature changes in the α-phase region. In textured uranium, these changes which are characterized by a directional deformation and porosity formation with corresponding reduction in density, appear after 250-1000 cycles, corresponding to 3.5-14 hours thermal cycling.

Cycling with two-phase transformations produces pronounced distortion of the shape of uranium specimens.

In this case, porosity formation, accompanied by a drop in density, is far more intensive than in the case of thermal cycling in the α-phase temperature range.

LITERATURE CITED

[1] S.T. Konobeevsky, N.F. Pravdyuk and V.I. Kutaltsev, Investigations in the Field of Geology, Chemistry and Metallurgy, Papers read by the Soviet Delegation at the International Conference on Peaceful Uses of Atomic Energy (Acad. Sci. USSR Press, 1955), p. 263.

[2] Chiswick and Kelman, Metallurgy of Nuclear Energy and the Effect of Radiation on Materials, Papers read by Foreign Scientists at the International Conference on Peaceful Uses of Atomic Energy (Metallurg Press, 1955), p. 612.

[3] M.E. Blanter, Methods of Investigating Metals and Evaluation of Experimental Data (Metallurg Press, 1952).

Received February 19, 1957

BLANK
PAGE

EXPERIMENTAL INVESTIGATION OF INJECTION EFFICIENCY IN A BETATRON

V.N. Logunov, E.P. Ovchinnikov and V.D. Rusanov

Experiments are described which have been carried outon the synchrotron of the Institute of Physics Acad. Sci. USSR (30 Mev electrons) for the purpose of investigating the physical effects involved in electron trapping in betatron acceleration. A detailed study was made of the effects on injection efficiency arising as a result of variable magnetic and electric fields which were artificially produced inside the acceleration chamber at the instant of time corresponding to electron injection. It is shown that both the auxiliary magnetic field, the effect of which on the particle may be compared with the effect of a rotational electric field (Kerst hypothesis), as well as the field of the "artificial" space charge can have a strong effect on the γ-radiation intensity only at small emission currents. However, qualitative estimates show that the effect of induction contraction, in accordance with the Kerst hypothesis, must be small compared with the Coulomb interaction in normal betatron operation. It is also shown that, in general, artificial methods such as these are ineffective in increasing intensity. It is suggested that only methods which allow a considerable change in the stabilizing forces of the magnetic field can lead to a significant increase in yield since the majority of betatrons operate under conditions approximating "limiting current." In conclusion, several models are presented to represent the possible role of the Coulomb interaction in the particle-trapping process in a stationary betatron orbit.

Most of the present hypotheses concerning particle trapping in betatron acceleration can be divided into two groups: those based on self-induction of the nonstationary current in the chamber [1-4] and those which are based on the interaction of the electrons with the Coulomb field of the space charge [5-7].

The present paper is devoted to a description of experiments in which the mechanisms proposed in these two cases of collective trapping were investigated.

Magnetic Contractor

The simulation of the contraction of the instantaneous electron orbit, due to self induction of the nonstationary current in the chamber, was realized by means of a rapid variation in the magnitude of the central magnetic flux Φ at the instant corresponding to the injection of electrons into the accelerator chamber. The device which provided this change in the magnitude of Φ was a supplementary winding, wound on the central core of the betatron, to which was applied a current pulse with a duration of several microseconds. Devices of this type are usually called contractors in accelerator terminology. The literature contains descriptions of a considerable number of attempts to increase the yield of bremsstrahlung γ-radiation of the betatron by means of contractors [8, 9]. However, in all cases described in these papers, in addition to the change in the central magnetic flux there was a change in the radial rate-of-decay of magnetic field in the region of the stationary betatron orbit because of the choice of location of the contractor winding (Figure 1, I, II).

Since a change in n leads to a decay or growth of the free betatron oscillations, it is impossible to draw any definite conclusion as to the effect of the contractor. The location of the contractor winding chosen in the

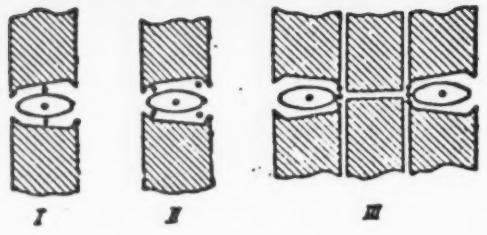

Fig. 1. Types of contractors used by different authors I) Adams; II) Wideroe; III) the authors of the present work.

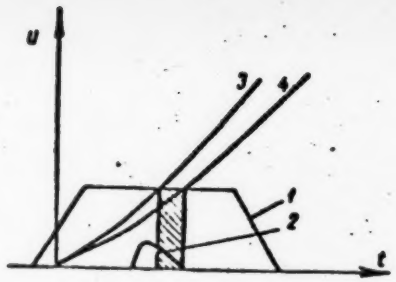

Fig. 2. Relative position of the voltage pulse in the injector and the current pulse in the contractor winding: 1) injection pulse; 2) contractor pulse; 3,4) limits of the trapping region.

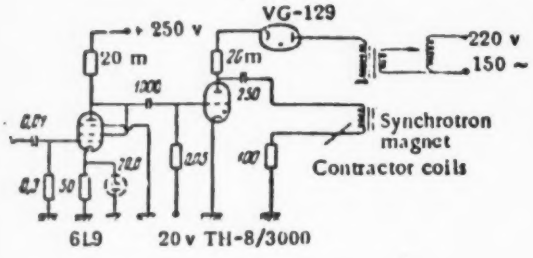

Fig. 3. Schematic diagram of the contractor.

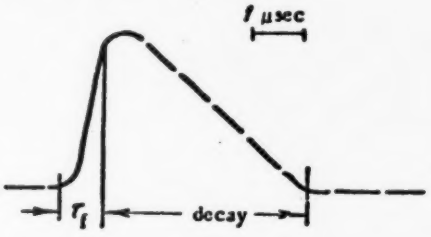

Fig. 4. Shape of the current pulse in the contractor winding.

present work (Figure 1, III) makes it possible to study the effect of induction contraction of the electron orbit on electron trapping without complications due to spurious effects.

When there are electrons in the chamber the pulsing of the magnetic field of the contractor can give rise to a reversible process. To make this an irreversible process, it is necessary that the current in the contractor winding be decreasing at injection. In Figure 2 is shown the relative location in time of the pulses corresponding to trapping during the horizontal portion of the injection pulse.

A schematic diagram of the contractor is shown in Figure 3. The shape of the current pulse in the contractor winding is shown in Figure 4.

In these experiments measurements were made of the intensity of the bremsstrahlung γ-radiation as a function of the position of the contractor current pulse in time with respect to a fixed injection pulse. The relative position of the pulses in time was observed on an oscilloscope.

Curves were taken of the function $I_{out} = f(t_{cont}, I_{emis})$ (where I_{out} is the intensity of the bremsstrahlung γ-radiation in relative units; t_{cont} is the time delay of the pulse in the contractor winding with respect to the time at which the magnetic field passes through zero; and I_{emis} is the emission current in the injector) for a large range of values of I_{emis} for trapping at the leading edge, the trailing edge, and the flat part of the injection pulse (Figures 5, 6, 7). The amplitude and shape of the pulses were kept fixed in each experiment. In addition, at each value of I_{emis} control points were measured with the contractor disconnected, that is, the corresponding value of the intensity was established. The function $I_{out} = f(t_{cont}, I_{emis})$ is a curve with one maximum or several maxima displaced in time with respect to each other. The maximum intensity corresponds to a contractor pulse position such that the current in the contractor winding is diminishing at the time of trapping. If the current pulse is displaced along the abscissa axis in the direction of larger t the intensity becomes virtually zero up to values $t \sim 20$-30 μsec (starting at this point the yield of bremsstrahlung γ-radiation increases gradually). Consideration of the curves in Figures 5, 6 and 7 indicates that the contractor efficiency falls off with increasing I_{emis}. On the other hand, in going over to high emission currents it is found that the contractor

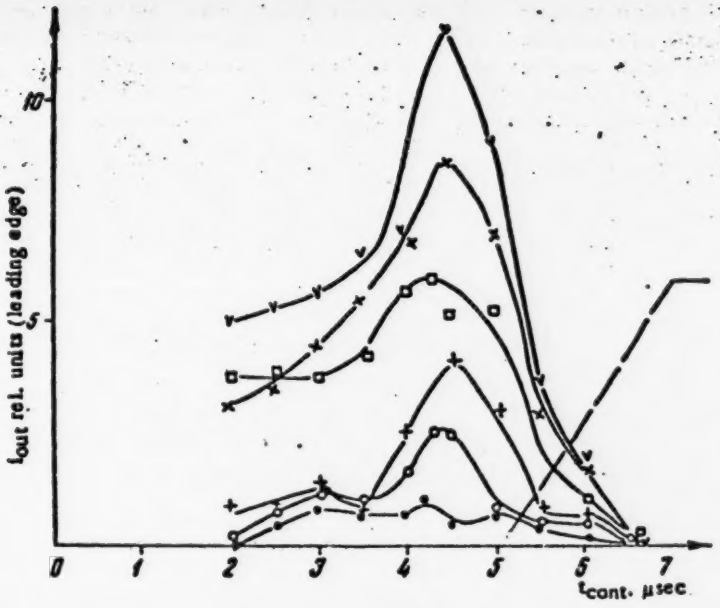

Fig. 5. Curves obtained for operation on the increasing part of the injector voltage pulse. U_{inj} = 11 kv; I_{emis}: ●) ~10 μamp, O) 16 μamp; +) 23 μamp; x) 6.4 μamp; V) 90 μamp; □) 300 μamp.

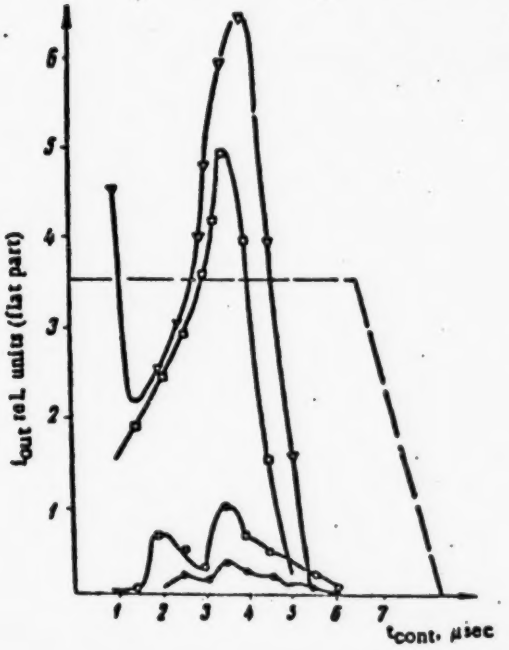

Fig. 6. Curves taken for operation on the flat part of the injector voltage pulse. U_{inj} = 11 kv; I_{emis}: ●) 36 μamp; O) 60 μamp; ▽) 260 μamp; □) 480 μamp.

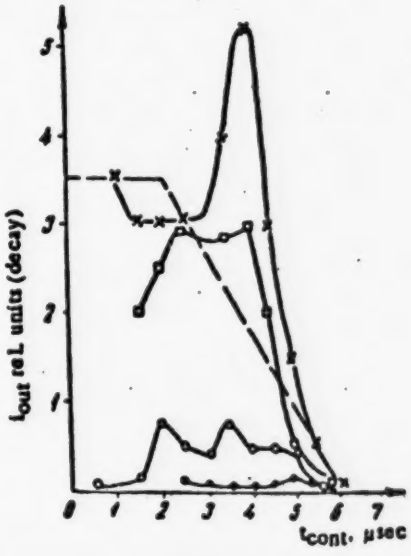

Fig. 7. Curves corresponding to operations at the trailing edge of the injector voltage pulse. U_{inj} = 11 kv; I_{emis}: ●) 24 μamp; O) 76 μamp; x) 250 μamp; □) 500 μamp.

Fig. 5-7. Curves showing the yield of bremsstrahlung γ-radiation as a function of the switching time of the current pulse in the contractor taken at different values of the injector emission current.

is more effective for operation at the leading edge of the injection pulse. From this point of view it is interesting to compare the behavior of the function $i_{out} = f(i_{emis})$ in the case of trapping at the leading edge (Figure 8a) and at the tail of the injection pulse (Figure 8b) with and without the contractor in operation. The experiments which have been carried out indicate qualitatively the possibility, in principle, of contraction of the electron orbit at the instant of injection due to self-induction of the electron current circulating in the chamber.

The rate-of-rise of the current in the contractor, corresponding to maximum trapping efficiency, was 1.3 amp/μsec.

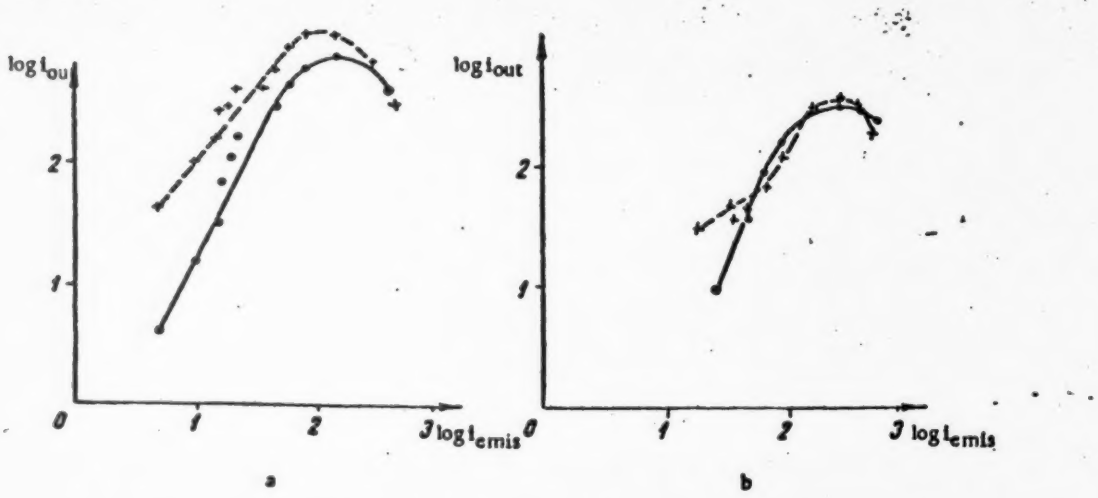

Fig. 8. Yield of bremsstrahlung γ-radiation as a function of emission current of the injector without the contractor (—) and with the contractor (– – –). U_{inj} = 11 kv; a) front; b) back.

Direct measurements of the circulating current in the chamber at the instant of injection indicates that the maximum value of the rate-of-rise of this current is 0.1 amp/μsec [10]. From this it follows that the contraction of the instantaneous orbits due to self-induction of the circulating current made up of accelerated electrons is small.

Electric Contractor

To study the effect of the Coulomb field on trapping efficiency at the instant of injection a space charge cloud in the form of a radially directed electron beam was introduced into the accelerator chamber by means of an auxiliary end-injector; we call this device an electric contractor. When this auxiliary injector is in operation an electron cloud, localized in azimuth, is produced in the chamber.

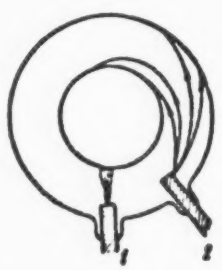

Fig. 9. Diagram showing the location of the electric contractor in the accelerator chamber: 1) end-injector; 2) main injector.

The arrangement of the electric contractor in the chamber is shown in Figure 9. In this case, the main injector is located at a smaller radius than the end-injector. Voltage pulses from different pulse generators are applied to both injectors. A trapezoidal pulse is applied to the main injector and a pulse in the form of half a sinusoid is applied to the end-injector.

In the experiment the dependence of the bremsstrahlung γ-radiation was studied as a function of the time at which the electric contractor was energized. The time behavior of both pulses was observed on a cathode ray oscilloscope. The parameters of the function $i_{out} = f(t_{cont})$ were the emission current in the electric contractor ($i_{emis\,con}$) and the emission current in the main injector (i_{emis}). The results of the measurements are shown in Figures 10, 11 and 12. The experiments indicate that the trap-

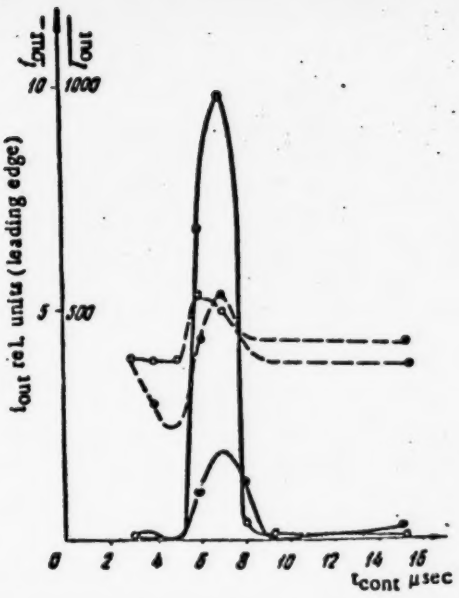

Fig. 10. Two series of curves showing the intensity of the bremsstrahlung γ-radiation as a function of the time at which the electric contractor is pulsed. Injection voltage of main injector ~11 kv, amplitude of voltage pulse in electric contractor ~4.5 kv. The curves were taken for the following values of the main-injector current: I_{emis} = 270 μamp (dotted curves: O) $I_{emis\,con}$ = 5 μamp, ●) $I_{emis\,con}$ = 15 μamp) and I_{emis} = 36 μamp (solid curves: ●) $I_{emis\,con}$ = 10 μamp, O) $I_{emis\,con}$ = 70 μamp).

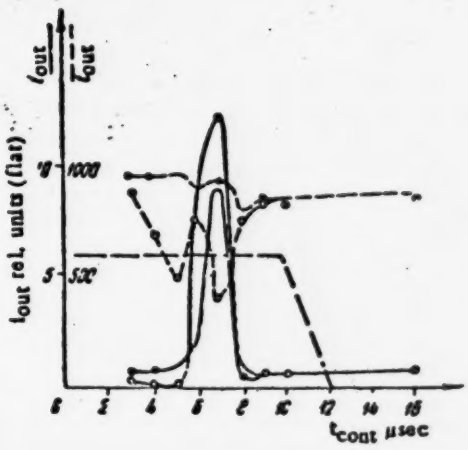

Fig. 11. Two series of curves showing the intensity of the bremsstrahlung γ-radiation as a function of the time at which the electric contractor is pulsed. Voltage of the injection voltage of the main injector ~11 kv, amplitude of voltage pulse in electric ontractor ~4.5 kv. The curves were taken for an emission current of ~40 μamp in the main injector (solid curves: ●) $I_{emis\,con}$ = 10 μamp, O) $I_{emis\,con}$ = 60 μamp) and ~370 μamp (dotted curves: ●) $I_{emis\,con}$ = 5 μamp, O) $I_{emis\,con}$ = 80 μamp): the curves were taken for operation at the flat part of the voltage pulse in the main injector.

ping factor increases strongly at small emission currents of the main injector. Under these conditions the intensity is increased by a factor of 40 to 50 when the electric contractor is used.

When only the electric contractor was energized (main injector disconnected) the intensity was not affected.. When the filament voltage of the electric contractor was reduced it had no further effect on the trapping process.

If the electric contractor was placed in front of the main injector, an increase in intensity (maximum of 3-4 times) was observed only at very small emission currents in the main injector.

With increasing emission of the main injector, the effect of the electric contractor was generally reduced and at normal operating current values its effect becomes null or even negative. On the other hand, an increase of the current in the end-injector had more pronounced effect in general.

Finally, it should be noted that the electric contractor is more effective at normal operating values of the emission current in the main injector when the leading edge of the injector pulse is used (although the effect here is still small at these values of the emission current).

An attempt at an exact mathematical description of the behavior of the electric contractor meets with a number of difficulties, mainly those involved in estimating the distribution of the space charge which acts on the particles in flight. However, it is possible to offer some qualitative considerations regarding the interaction of a charge cloud which is localized in azimuth with an electron which passes through it. If it is assumed that the density of the charge cloud diminishes in time, the energy loss of particles which pass through the cloud can be estimated roughly from the expression

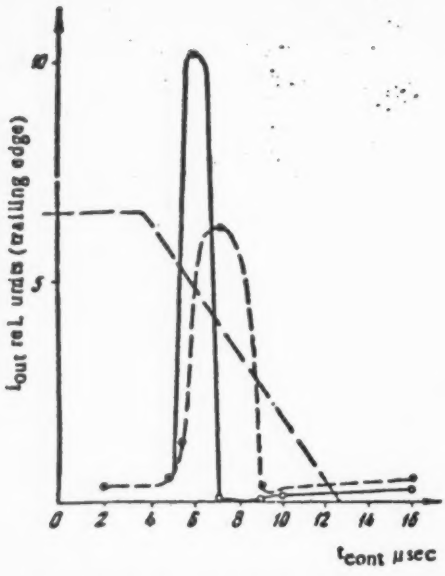

Fig. 12. The intensity of the bremsstrahlung γ-radiation as a function of the time at which the electric contractor is pulsed, obtained for operation at the trailing edge of the injection voltage pulse in the main injector. U_{inj} = 11 kv; $U_{inj\,con}$ = 4.5 kv; I_{emis} = 60 μamp; $I_{emis\,con}$: ●) 7.5 μamp, ○) 240 μamp.

$$|\Delta W| = 2\frac{\alpha}{v} e Q \ln\frac{R}{a}, \qquad (1)$$

where α is the rate at which the space charge diminishes in time; v is the initial velocity of an electron along an orbit of radius R; a is a linear dimension of the cloud; Q is the total charge of the cloud.

An estimate of the contraction per revolution of the electron orbit for these parameters yields the value ~0.3 mm. Thus, it is apparent that a charge of variable density which is artificially introduced into the chamber can lead to an increase in the efficiency of particle trapping in a betatron accelerator. An estimate of the decay of the fast betatron oscillations due to the reduction in the density in the space charge gives (for the given parameters) a value ~0.1 mm/rev or even less. The possibility of resonance attenuation due to the appearance of the first harmonic in the azimuthal density distribution of the space charge is also very small.

Thus, the effect of the electric contractor can roughly be attributed to the retardation of electrons and to the decay of fast betatron oscillations.

DISCUSSION OF RESULTS

1. On the basis of the experiments which have been carried out it has been established that the use of a magnetic contractor or an electric contractor can increase the trapping efficiency only in the region of small emission currents where the trapping is usually accomplished by virtue of adiabatic contraction of the instantaneous electron orbit and inhibition of the free betatron oscillations. In this case the intensity of the bremsstrahlung γ-radiation increases by a factor of 20 or 30 and even more. On the other hand, in the region of high-emission currents, that is, at those current values which correspond to "collective trapping mechanisms," both methods of artificial contraction of the electron orbit become ineffective. It is obvious that the maximum of the curve $I_{out} = f(I_{emis})$ is determined by the defocusing properties of the space charge in the accelerator chamber. A rough estimate of the limiting current which can be constrained by the stabilizing forces of the magnetic field can be made on the basis of the following expression

$$I_{lim} = a\frac{\pi r^2 (1-n) U v}{30 c R^2}, \qquad (2)$$

where r is the distance from the injector to the equilibrium orbit; U is the injector voltage; v is the electron velocity at injection; R is the radius of the equilibrium orbit. The correction factor a takes into account the electronic "background" in the accelerator chamber.

A direct measurement of the current circulating in the chamber by means of an induction method gives satisfactory agreement with this estimate. Thus, attempts at artificial enhancement of the contraction of the instantaneous orbit at the instant of injection cannot lead to a noticeable increase in the intensity as compared with the maximum which can be achieved without the use of the auxiliary equipment. On the other hand, any method which increases the value of the limiting charge at the instant of injection will lead to improved operation of the betatron. A significant increase in the intensity of the γ-radiation of the betatron is possible only

if the stabilizing force of the magnetic field is increased or if the space charge inside the accelerator chamber is compensated.

2. A comparison of the induction-trapping hypothesis with experiment indicates that this mechanism, if it exists at all, has a very small effect and is not important. Thus, the magnetic contractor has a noticeable effect at a rate-of-rise of 1.3 amp/μsec while the maximum rate-of-rise in the chamber as measured by an induction method [10] was found to be less than 0.1 amp/μsec.

A rough estimate of the orbit contraction per revolution in accordance with the Kerst formula

$$dR = -R\frac{eL\frac{di}{dt}}{2(1-n)W} \tag{3}$$

(where L is the inductance of a loop at a radius of the equilibrium orbit; W is the energy of the injected electrons) indicates that at normal operating currents the quantity dR is very close to the quantity which corresponds to an adiabatic process.

3. In experiments with an electric contractor it has been established that an enhancement of the trapping efficiency occurs mainly as a result of a reduction in the time required for localization in azimuth of the space charge. Furthermore, the effect of this supplementary space charge is greater at higher voltages in the main injector. Similar experiments carried out with an ordinary contractor also indicate that the trapping efficiency is greatest at the leading edge of the injection pulse. Finally, it has been established that a reduction in the decay length of the injection pulse increases the output yield (for operation in the collective trapping region) in spite of the fact that the trapping time is reduced in this case [11].

It follows that the increase in the efficiency of collective trapping is related to the decay of the space charge in time. This conclusion is based on the fact that, as is well known, there is always a considerable nonuniformity in the azimuthal distribution of space charge in the betatron chamber. Consequently, an electron passing through a nonuniform region during the decay time loses energy; this phenomena leads to capture in a stationary orbit.

The decay of the space charge can occur not only with a reduction in the voltage at the cathode of the injector but even when this voltage remains constant or even when it is increased. As a matter of fact, at the instant of time which precedes the formation of the circulating current in the chamber the beam from the injector falls upon the inner wall of the chamber (the leading edge of the injector pulse) or upon the outer wall (the trailing edge and flat part) thus producing a strong space charge.

With the appearance of the nonstationary circular current in the chamber this space charge diminishes quickly.

The authors wish to take this opportunity to express their gratitude to Corr. Mem. Acad. Sci. USSR V.I. Veksler and Dr. of Math-Phys. Sciences M.S. Rabinovich for many discussions of the results of this work and valuable critical comments. The authors also wish to thank their colleagues who operated the 30-Mev synchrotron of the Institute of Physics Acad. Sci. USSR.

LITERATURE CITED

[1] D.W. Kerst, Phys. Rev. 74, 503 (1948).

[2] R. Wideroe, Z. Ang. Phys. 5, 5, 187 (1953).

[3] P.A. Ryazin, Electron Trapping in Betatron Accelerators (Report to the All-Union Conference on High-Energy Particle Physics, 1956).

[4] D.W. Kerst, G.D. Adams, H.W. Koch and C.S. Robinson, Rev. Sci. Instr. 21, 462-480 (1950).

[5] R. Wideroe, J. Appl. Phys. 22, 362 (1951).

[6] S.E. Barden, Proc. Phys. Soc. 64B, 85 (1951).

[7] V.S. Melikhov, Dissertation (Tomsk Polytechnic Inst. 1954).

[8] G.D. Adams, Rev. Sci. Instr. 19, 607-608 (1948).

[9] D.W. Kerst, G.D. Adams, H.W. Koch and C.S. Robinson, Phys. Rev. 78, 297 (1950).

[10] V.N. Loginov, E.P. Ovchinnikov, V.D. Rusanov and S.S. Semenov, J. Tech. Phys. (in press).

[11] V.N. Loginov, E.P. Ovchinnikov, V.D. Rusanov and M.S. Rabinovich, Investigation of the Betatron Regime in a 30 Mev Synchrotron (Report to the All-Union Conference on High-Energy Particle Physics, 1956).

Received November 2, 1956

ON THE TRANSFORMATION OF β-PARTICLE ENERGIES TO ELECTRIC ENERGY IN GERMANIUM CRYSTALS WITH p-n JUNCTIONS

B.M. Vul, V.S. Vavilov, L.S. Smirnov, G.N. Galkin, V.M. Patskevich and A.V. Spitsyn

We present the results of an investigation performed in 1955 on the transformation of the energy of fast electrons into electric energy by germanium crystals with p-n junctions, as well as data on the efficiency of this transformation and its dependence on the absorbed radiation flux and total dose. It is found that the basic factor reducing the efficiency of transformation is the increase of the recombination rate of electrons and holes on recombination levels of structural defects arising as a result of the irradiation. Changes in the equilibrium electric conductivity and carrier mobilities play a secondary role. A method is indicated for reestablishing the initial properties of crystals by heating them. Ionization curves are given for monoenergetic electron beams in germanium.

During the past few years several works have been published on the direct transformation of radioactive decay energy to electric energy with the aid of semiconductor devices with p-n junctions [1-3]. The theory of semiconductor energy transformers is essentially similar to the theory of p-n junction photocells [2-5].

We have performed experiments to determine the efficiency for transformation of β-particle energies in n-type germanium crystals with p-n junctions obtained by alloying with indium [5].

The β-particle source used was Sr^{90}-Y^{90}. The total activities of the initial sources were 50, 100, and 200 μc. The β sources were prepared in the form of 8 mm diameter tablets of strontium sulfate whose activities were 50 and 100 μc and strontium carbonate whose activity was 200 μc.

Figure 1 shows the β-spectra of the 50 and 200 μc sources. The spectra were obtained by M.V. Viskova. The energy incident on the germanium crystal was determined from measurements of the β-spectra and the total β-particle current. It was found that the radioactivity used was lower by a factor of 5 than the intrinsic radioactivity, due to self-absorption and the geometric configuration of the transformer.

We also performed measurements in which the semiconductor was irradiated by artificially accelerated electrons with energies from 400 to 1150 kev. In this case the electron beam intensity corresponded to a β-source whose activity is several tenths of a curie. The efficiency of transformation of radiant energy, which may be defined as the ratio between the electric power delivered to a matched load and the radiant energy flux incident on the semiconductor, depends on the average energy, ϵ, expended in the formation of one excess pair of current carriers, the fraction α of carriers that reaches the p-n junction (this fraction is always less than one due to recombination on the surface and in the volume), and a factor accounting for the reflection and absorption of β-particles and the geometry of the energy transformer. The magnitude of ϵ was determined in a separate experiment [6] and was found to be 3.7 ± 0.4 ev. In the energy transformers we used α attained a value of 0.65. In choosing the geometry of the transformer, the spatial distribution of the ionization in the crystal is of great importance.

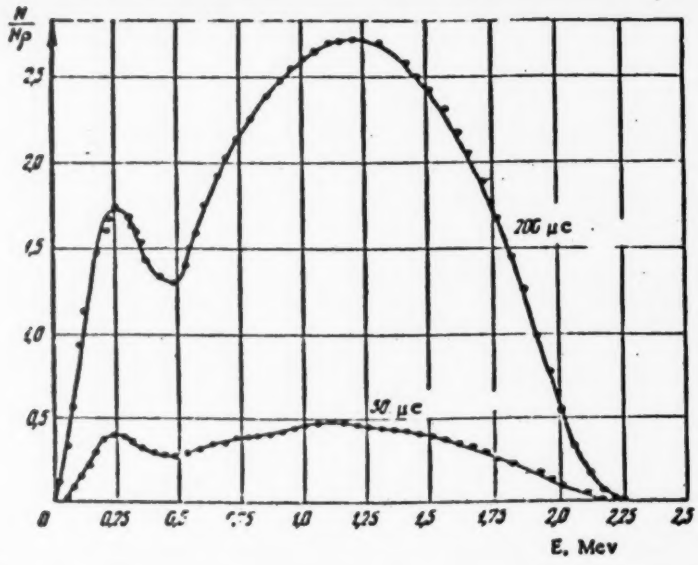

Fig. 1. β-spectra of the 50 and 200 μc Sr^{90}-Y^{90} sources. N/Hρ is the number of particles per unit time in a given interval of Hρ (where H is the magnetic field strength of the spectrometer, and ρ is the radius of curvature of the β-particle orbit).

From measurements of the relative ionization produced by an electron beam in a narrow gap between two germanium plates, we constructed ionization curves for electrons with energies from 420 to 920 kev (Figure 2). Since the mean β-energy emitted by thick Sr^{90}-Y^{90} sources is of the order of 1000 kev, the fundamental ionization region for these sources enters to a depth of about 0.6 mm, as can be seen from the curves of Figure 2.

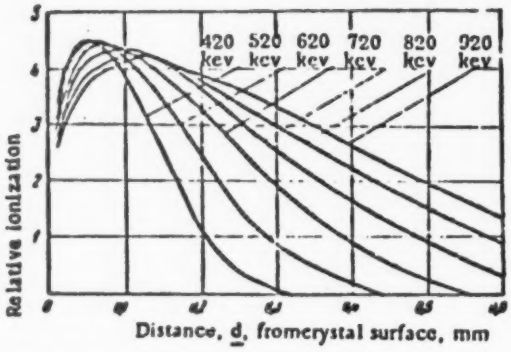

Fig. 2. Ionization curves in germanium for parallel electron beams with energies from 420 to 920 kev incident purpendicular to the surface of the crystal.

The efficiency of transformation was found from the load characteristics (Figure 3). For the 200 μc β-source the efficiency of the transformer was 0.06% for an emf of 13 mv, and a short-circuit current of 41 μa.

Figure 4 shows the load characteristics for irradiation by monoenergetic electrons. The maximum efficiency of the transformer in this case was 0.72% for an emf of 0.115 v, and a short-circuit current of 2.6 ma.

The dependence of the transformer efficiency on the incident radiant energy flux P_i for the first few moments of irradiation is shown in Figure 5.

The experimentally observed fact that the transformation efficiency stops increasing for high electron fluxes (of the order of 0.1 w/cm^2), is clearly related to an increase in the recombination rate [5]. When fast electrons pass through a crystal some lattice sites are left empty and some atoms enter the spaces between the sites, i.e., Frenkel's defects are produced. The energy threshold for formation of defects in germanium has been measured and is equal to 500 ± ± 20 kev [7].

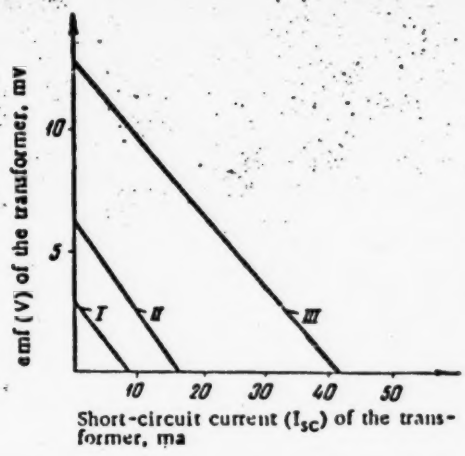

Fig. 3. Load characteristics for a germanium crystal with a p-n junction irradiated by β-particles from Sr^{90}-Y^{90} sources with activities of (I) 50 μc; (II) 100 μc; (III) 200 μc, at the beginning of irradiation.

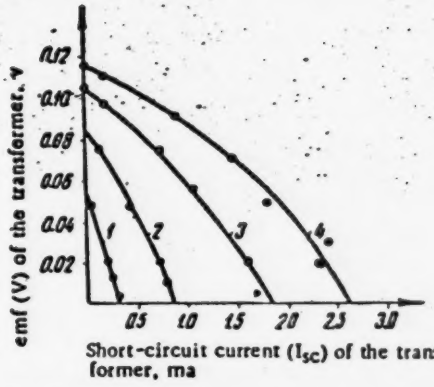

Fig. 4. Load characteristics for a germanium crystal with a p-n junction irradiated by 480-kev electrons. P_i is the energy flux of the incident radiation, and η is the efficiency of the transformer. 1) $P_i = 3.84 \cdot 10^{-3}$ w/cm², η - 0.22%; 2) $P_i = 9.6 \cdot 10^{-3}$ w/cm², η - 0.43%; 3) $P_i = 1.92 \cdot 10^{-2}$ w/cm², η = 0.63%; 4) $P_i = 2.88 \cdot 10^{-2}$ w/cm², η = 0.72%.

Defects in crystals influence electron motion, and are manifested by changes in the conductivity of the crystal and the lifetime of excess current carriers.

We have studied the variation of the emf V_0 and the short-circuit current I_{sc} of germanium crystals with p-n junction as a function of the total β-particle radiation dose. The results of the measurements are shown in Figures 6 and 7. In addition, we performed direct measurements of the effective lifetime of excess carriers τ_{eff} in germanium bars as a function of the time of constant intensity irradiation. The lifetime of excess carriers was measured by a bridge method [8].

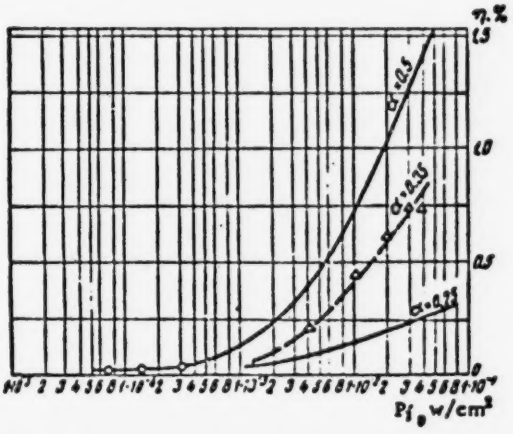

Fig. 5. The initial values of the efficiency η of energy transformation by germanium crystals with p-n junctions, given as a function of the energy flux P_i of the incident radiation for different values of α. The solid curves are the theoretical ones for α = 0.5 and α = 0.25, the dotted one is for α = 0.35. The experimental points are: Δ) electrons of energy E = 500 kev, and O) β-rays from Sr^{90}-Y^{90}.

As the irradiation time is increased, V_0, I_{sc}, τ_{eff} and the efficiency of the transformer all decrease. The increase of V_0 and I_{sc} which is observed for 1-2 hours after the start of irradiation in air is not related to electron bombardment of the surface, but is due to the presence of ozone, which decreases the surface recombination rate.

The primary reason for the drop in the efficiency of transformation when germanium is bombarded by electrons is the reduction of the effective carrier lifetime due to recombination centers which are stable at room temperature being formed in the volume of the crystal; these recombination centers arise as a result of the destruction of the crystal lattice by the fast electrons. The changes in resistivity and carrier mobility play an insignificant role in this process. Thus, for instance, when the radiation defect concentration is increased to $5 \cdot 10^{12}$ cm^{-3}, the resistivity of a germanium crystal whose original resistivity is 3 ohm/cm changes by 5%, and the lifetime τ_{eff} drops from 500 to 100 μsec.

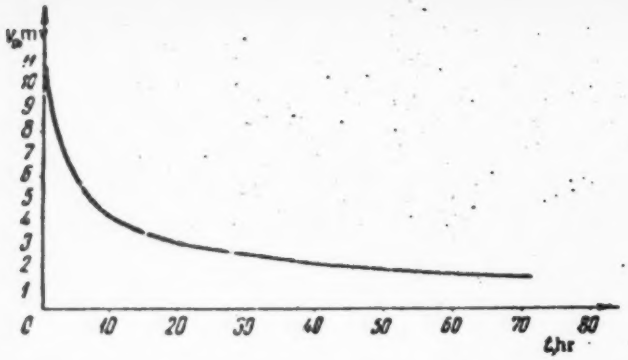

Fig. 6. The dependence of the emf V_θ of a germanium transformer on the β-ray irradiation time, using a 200 μc Sr^{90}-Y^{90} source.

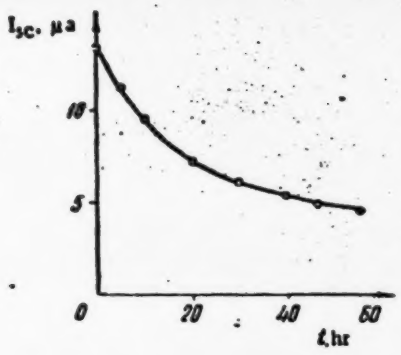

Fig. 7. The dependence of the short-circuit current I_{sc} of a germanium transformer on the β-ray irradiation time from a 100 μc Sr^{90}-Y^{90} source.

The decrease in the electric conductivity and lifetime of excess carriers due to irradiation by fast electrons have the same threshold energy of about 500 kev. If we know the number of defects formed in a germanium rod by radiation, and if we know the decrease in the lifetime, we can find θ, the effective cross section for recombination capture of an electron by a defect. We found θ to be $1 \cdot 10^{-16}$ cm^2 [9].

At room temperature the initial properties of a crystal that has been subjected to radiation are reestablished very slowly [10], and therefore one may not count on continuous self-regeneration of germanium energy transformers operating under sufficiently intense irradiation.

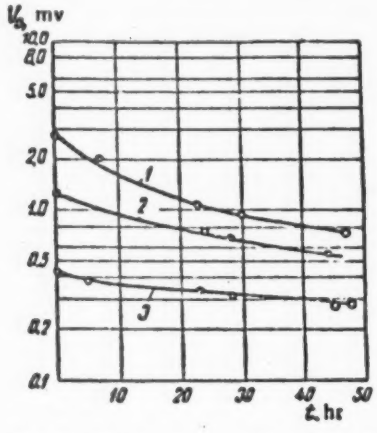

Fig. 8. The dependence of the emf V_θ of a germanium transformer on the β-ray irradiation time from a 100 μc Sr^{90}-Y^{90} source without a filter (1) and with germanium filters of thickness 0.3 mm (2) and 0.5 mm (3).

Radiation damage which reduces the carrier lifetime in germanium crystals can at least partially be removed by annealing. We have subjected germanium crystals with p-n junctions (obtained by alloying with indium) to slow annealing (84 hours at a temperature of 140 ± 5°C) after they have undergone fast-electron bombardment. The annealing process almost completely reestablished the initial values of V_θ and I_{sc}. Annealing at higher temperatures is impossible, since indium melts at 157°C.

It is not helpful to decrease the β-particle energy by absorbers, since these absorb primarily slow electrons, which carry a large part of the energy. Experiments in which the β-energy from a 100 μc Sr^{90}-Y^{90} source was lowered by means of a germanium filter showed that a 0.3 mm thick absorber doubles the irradiation time t necessary to reduce V_θ by a factor of 2. The initial emf, however, also drops by a factor of 2.

A 0.5 mm thick filter increases t by a factor of 5 and reduces the initial emf by a factor of 6. The results of these measurements are shown in Figure 8.

The data obtained on the changes in germanium crystal under the action of fast-electron irradiation showed that an energy transformer consisting of a germanium crystal with a p-n junction and a Sr^{90}-Y^{90} β-source cannot reasonably be used as a long-term source of electric energy.

According to the data in the literature [2, 3], silicon β-transformers have higher efficiencies than ger-

manium, but the number of defects caused by β-radiation in silicon is much greater than the number in germanium, so that the efficiency of transformation drops rapidly as the dose of radiation is increased.

A stable source of electric energy may be obtained from a combination of a semiconductor in which p-n junctions with low saturation currents can be established, and a source of low-energy β-radiation whose maximum energy is less than the threshold for formation of defects in the semiconductor (for instance, germanium with Tl^{204} or Pm^{147}, or silicon with Ni^{63}).

The use of very low-energy β-sources (for instance tritium) is not very helpful due to the low specific power and the high self-absorption.

Experiments on preparing p-n junctions by thermal diffusion methods show that for such junctions the transformation of β-energy is even less efficient than for alloyed junctions, since the lifetime of minority carriers in the crystals is lower.

The authors express their sincere gratitude to P.Ia. Glazunov who took part in the experiments with the artificially accelerated electrons, and to P.N. Kodochigov for his valuable help in the preparation and examination of the Sr^{90}-Y^{90} samples.

LITERATURE CITED

[1] P. Rappaport, Phys. Rev. 93, 246 (1954).

[2] W. Pfann and W. Roosbroeck, J. Appl. Phys. 25, 1422 (1954).

[3] E.G. Linder, P. Rappaport and Dzh. Dzh. Loferski, Applications of Radioactive Isotopes to Industry, Medicine and Agriculture, Reports of Foreign Scientists to the International Conference on the Peaceful Uses of Atomic Energy, Geneva 1955 (Acad. Sci. USSR Press, 1956), p. 21.

[4] S.M. Ryvkin, J. Tech. Phys. 25, 21 (1955).

[5] V.S. Vavilov and L.S. Smirnov, Radio Technology and Electronics 1, 1147 (1956).

[6] V.S. Vavilov, L.S. Smirnov and V.M. Patskevich, Proc. Acad. Sci. USSR (in press).

[7] V.S. Vavilov, L.S. Smirnov, G.N. Galkin, A.V. Spitsyn and V.M. Patskevich, J. Tech. Phys. 26, 1865 (1956).

[8] S.V. Bogdanov and B.D. Kopylovskii, PTE No. 1, 66 (1956).

[9] L.S. Smirnov and V.S. Vavilov, J. Tech. Phys. 27, 427 (1957).

[10] R. Fletcher and W. Brown, Phys. Rev. 92, 585 (1953).

Received January 18, 1957

BLANK
PAGE

RADIATION FROM A CYLINDRICAL SOURCE

E.E. Kovalev

We consider the radiation from a cylindrical source, treating one without self-absorption in the first section, and one with self-absorption in the second one.

We obtain an analytical expression for the γ-radiation yield in the radial direction from a nonabsorbing cylindrical source. This is given in terms of tabulated functions only. This expression can be used to calculate the γ-radiation yield from nonabsorbing cylindrical sources (cylindrical condensers filled with radioactive gas, certain types of γ-sources, neutron sources, etc.). It can be used for self-absorbing sources if this effect is accounted for by a self-absorption factor. The second section of this article is devoted to a calculation of the self-absorption factor for a cylindrical source. Expressions for this factor are obtained for sources with different absorption coefficients and height-to-diameter ratios, and the values are given in tabular form. The data presented in this article can be used in practice for calculation of the γ-radiation yield from cylindrical sources, which are widely used in practice.

Various shapes of γ-sources have found wide application in science and technology. Independent of its use, a fundamental characteristic of a source is its γ-radiation yield, that is, the γ-dose rate from the source at a given point.

In general the γ-radiation yield is determined by the following basic factors: the γ-ray energy, the specific or total source activity, the geometry (size and shape of the source and distance from a given point), self-absorption, and multiple scattering within the source. Calculation of the effects due to these factors is in general quite difficult.

In this article, we restrict our considerations to the influence of geometry and self-absorption on the γ-radiation yield, and shall first consider the radiation yield from a nonabsorbing cylindrical source, and then from one with self-absorption.

Radiation from a Nonabsorbing Cylindrical Source

Although cylindrical γ-ray sources are widely used in practice, the literature does not yet contain an expression for the γ-radiation yield in the radial direction from a solid circular cylindrical source. It has been asserted [1-5] that the expression for the γ-radiation yield from a solid cylindrical source without self-absorption contains an integral which can only be calculated numerically. It has also been asserted [1, 2] that for points located on the surface or the axis of the cylindrical source the integration can be performed and leads to analytic expressions.

We shall consider below an arbitrary point in the radial direction.

In this case the γ-dose rate at A (Figure 1), a distance b from the axis of the cylinder, is given by

$$P_0 = 2P_\gamma q \int_0^h \int_0^R \int_0^\pi \frac{dz\rho\, d\rho\, d\varphi}{z^2 + \rho^2 + b^2 - 2\rho b \cos\varphi},$$

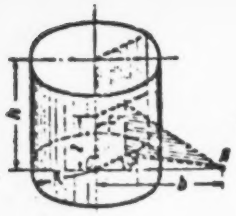

Fig. 1. For the calculation of the radiation yield at a given point an arbitrary distance from the cylindrical axis.

where Γ_γ is the γ-ray dose rate at a unit distance from a source of unit activity, and q is the specific activity of the source (the remaining notation is given in Figure 1). Integrating over φ and ρ, and then integrating by parts, we obtain

$$P_\rho = \pi P_\gamma q \left\{ 2h(1-\ln h) - h\ln 2 + h\ln[h^2 + \right.$$
$$+R^2 - b^2 + \sqrt{h^4 + 2h^2(R^2+b^2) + (b^2-R^2)^2}] - h - \qquad (1)$$
$$-(b^2-R^2)\int_0^h \frac{dz}{\sqrt{z^4 + 2z^2(R^2+b^2) + (b^2-R^2)^2}} -$$
$$\left. -\int_0^h \frac{z^2\,dz}{\sqrt{z^4 + 2z^2(R^2+b^2) + (b^2-R^2)^2}} \right\}.$$

Let us consider the integral

$$I_1 = \int_0^h \frac{dz}{\sqrt{z^4 + 2z^2(R^2+b^2) + (b^2-R^2)^2}}.$$

It is known that an integral of this type can be reduced to an elliptic integral of the first kind $F(\varphi, k)$, if $k^2 \leq 1$. In our case $k = 2\sqrt{Rb}/(R+b)$. Obviously $k^2 \leq 1$ for all values of b and R. Thus

$$I_1 = \frac{1}{b+R} F(\varphi, k),$$

where $\varphi = \operatorname{arctg} \frac{h}{b-R}$.

Let us now consider the integral

$$I_2 = \int_0^h \frac{z^2\,dz}{\sqrt{z^4 + 2z^2(R^2+b^2) + (b^2-R^2)^2}} = \int_0^h \sqrt{\frac{z^2+(b-R)^2}{z^2+(b+R)^2}}\cdot dz - (b-R)^2 I_1.$$

The integral

$$I_3 = \int_0^h \sqrt{\frac{z^2+(b-R)^2}{z^2+(b+R)^2}}\,dz$$

in this expression can be reduced to an elliptic integral of the third kind $\Pi(\varphi, n, k)$, if $k^2 \leq 1$.

Thus

$$I_3 = \frac{(b-R)^2}{b+R}\cdot \Pi(\varphi, n, k),$$

where $n = -1$.

Inserting the expressions for I_1 and I_2 into Equation (1), we obtain an expression for the γ-ray dose rate for an arbitrary radial point, this expression involving elliptic integrals of the first and third kinds. It should be noted, however, that in practice it is inconvenient to make use of the elliptic integral of the third kind, since this integral is not tabulated. It is therefore useful to have the expression relating the elliptic integral of the third kind with those of the first and second kinds, namely

$$\Pi(\varphi, n, k) = \frac{1}{1-k^2}\left[\operatorname{tg}\varphi\sqrt{1-k^2\sin^2\varphi} - E(\varphi, k) + (1-k^2)F(\varphi, k)\right]. \qquad (2)$$

if $n = -1$, and where $E(\varphi, k)$ is the elliptic integral of the second kind. Using Relation (2) one arrives simply at the final expression for the γ-radiation yield in the radial direction from a cylindrical source:

$$P_0 = \pi P_\gamma q h \left\{ 1 + \right.$$

$$+ \ln \frac{h^2 + R^2 - b^2 + \sqrt{h^4 + 2h^2(R^2 + b^2) + (b^2 - R^2)^2}}{2h^2} -$$

$$\left. - \frac{b-R}{h} F(\varphi, k) - \frac{b+R}{h} \left[\operatorname{tg} \varphi \sqrt{1 - k^2 \sin^2 \varphi} - E(\varphi, k) \right] \right\}. \qquad (3)$$

We note that this expression contains only tabulated functions, which makes it possible to avoid numerical and graphical integrations which are commonly used in such cases.

Let us now consider two special cases: 1) $b = R$ (the given point is on the surface of the cylinder), and 2) $b = 0$ (the given point is on the cylindrical axis).

Case 1: $(b = R)$

$$P_0 = \pi P_\gamma q R \left\{ \frac{h}{R} \left(1 - \ln \frac{2h}{R} \right) + \right.$$

$$+ \frac{h}{R} \ln \left[\frac{h}{R} + \sqrt{\left(\frac{h}{R} \right)^2 + 4} \right] +$$

$$\left. + 2 - \sqrt{\left(\frac{h}{R} \right)^2 + 4} \right\} \equiv \pi P_\gamma q R \Phi \left(\frac{h}{R} \right). \qquad (4)$$

It is clear that a point on the surface halfway up a cylinder of height $H = 2h$, experiences a γ-ray dose rate given by

$$P_H = 2\pi P_\gamma q R \Phi \left(\frac{h}{R} \right). \qquad (4a)$$

It can be shown that $\lim \Phi(h/R) = 2$ as $h/R \to \infty$, and thus for an infinitely long cylinder the γ-ray radiation rate at its surface is given by

$$P_\infty = 4\pi P_\gamma q R.$$

This relation may be used for cylindrical sources with $h/R \geq 10$, and the maximum error will be no greater than 5%. Equation (4) can also be used to find the γ-ray dose rate at an arbitrary point on the surface of the cylinder. Thus

$$P(h, R, x) = \pi P_\gamma q R \left[\Phi \left(\frac{h+x}{R} \right) - \Phi \left(\frac{x}{R} \right) \right], \qquad (4b)$$

if the given point is located on the extension of the cylindrical surface a distance $\underline{x}$ from the base, and

$$P(h, R, x) = \pi P_\gamma q R \left[\Phi \left(\frac{h-x}{R} \right) + \Phi \left(\frac{x}{R} \right) \right], \qquad (4c)$$

if the given point is located on the cylindrical surface a distance $\underline{x}$ from the base.

We note a particular property of Equation (4). It can be shown that

$$\Phi \left(\frac{h}{R} \right) \Big|_{\frac{h}{R} = 1,4} = \frac{h}{R}.$$

In this case Equation (4a) becomes

$$P_H = 2\pi P_\gamma q h = P_\gamma \frac{Q}{H^2}.$$

where $Q = 2\pi R^2 hq$ is the total source activity. This relation leads to the following conclusion: if $h/R = 1.4$, then the γ-ray dose rate at a point on the surface halfway up the cylinder is the same as if the total activity of the source were located at its geometric center.

Case 2: ($b = 0$)

$$P_0 = \pi P_\gamma q h \left[\ln\left(1 + \frac{R^2}{h^2}\right) + 2\frac{R}{h} \operatorname{arctg} \frac{h}{R} \right]. \tag{5}$$

This expression can be used when the given point lies on the axis (or its extension) at an arbitrary distance x from the base:

$$P(h, R, x) = \pi P_\gamma q \left\{ (h \mp x) \left[\ln\left(1 + \frac{R^2}{(h \mp x)^2}\right) + 2\frac{R}{h \mp x} \operatorname{arctg} \frac{h \mp x}{R} \right] \pm x \left[\ln\left(1 + \frac{R^2}{x^2}\right) + 2\frac{R}{x} \operatorname{arctg} \frac{x}{R} \right] \right\}.$$

Expressions of this type are obtained by using the superposition principle, which is valid in our case since self-absorption and multiple scattering of the γ-radiation in the source is not taken into account. This principle can also be applied to Equation (3).

Thus the expressions presented above can be used to determine the radiation yield from a cylindrical source with no self-absorption.

Radiation of a Cylindrical Source with Self-Absorption

The γ-radiation yield from extended sources depends, in general, to a great extent on the absorption of the radiation in the source itself (self-absorption). In many cases it is necessary to calculate the effect of self-absorption on the γ-radiation yield. We shall do this for a finite cylindrical source. We note that this problem has not yet been solved [3, 6, 7].

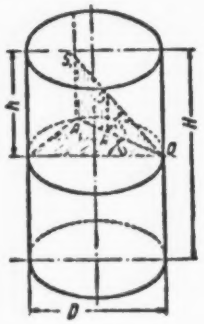

Fig. 2. For the derivation of the equation for the self-absorption factor in a cylindrical source.

Let us define the self-absorption factor as the ratio of the radiation yield from an extended source with self-absorption to the radiation yield from a nonabsorbing source. We shall make the following assumptions: a) the radioactive substance is distributed homogeneously through the volume of the cylinder; b) the γ-radiation from the source is monoenergetic; c) the radiation absorption is described by an exponential. The last assumption means that we are neglecting multiple Compton scattering in the source itself. It is quite difficult to take account of this effect, and requires separate consideration.

Let us introduce the following notation (Figure 2): f is the self-absorption factor; P is the γ-ray dose rate at the point O with self-absorption taken into account; P_0 is this dose rate at O neglecting self-absorption (the expression for P_0 has been given in the first section of this article); D is the diameter of the cylinder; H is its height ($H = 2h$); μ is the absorption coefficient of γ-radiation in the source material; O is the origin of the x, θ, φ spherical coordinate system, $OS = x$, and $OS_1 = x_1$. With the assumptions made, the self-absorption factor for a finite cylindrical source is by definition.

$$f = \frac{P}{P_0} = \frac{4P_\gamma q \int_0^{\pi/2} \int_0^{\pi/2} \int_0^{x_1(\theta,\varphi)} \frac{x^2 e^{-\mu x} \cos\varphi \, d\varphi \, d\theta}{x^2} dx}{4P_\gamma q \int_0^{\pi/2} \int_0^{\pi/2} \int_0^{x_1(\theta,\varphi)} \frac{x^2 \cos\varphi \, d\varphi \, d\theta}{x^2} dx}. \tag{6}$$

After performing the integration in the denominator and integrating the numerator over x, Equation (6) becomes

$$f=\left(\frac{2}{\mu D}\right)\frac{1-\frac{2}{\pi}\int_0^{\pi/2}\int_0^{\pi/2}\cos\varphi\, e^{-\mu x_1(\theta,\varphi)}\,d\varphi\,d\theta}{\frac{H}{D}\left(1-\ln\frac{2H}{D}\right)+\frac{H}{D}\ln\left(\frac{H}{D}+\sqrt{\left(\frac{H}{D}\right)^2+4}\right)+2-\sqrt{\left(\frac{H}{D}\right)^2+4}}. \tag{7}$$

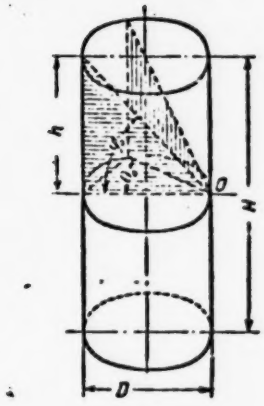

Fig. 3. The limiting angles θ_0 and φ_0 for a finite cylindrical source.

We take account of the finite height of the cylinder in Equations (6) and (7) in the upper limit for integration over x:

$$x_1=x_1(\theta,\ \varphi).$$

It is clear that in integrating over φ we must consider two cases (Figure 3), namely 1) $\varphi \le \varphi_0$ and 2) $\varphi \ge \varphi_0$, where $\varphi_0 = \arctan\frac{H}{2D}$. In the first case integration over x is taken from 0 to the intersection of OS with the side surface of the cylinder (point S_1 in Figure 2). This means that

$$x_1=D\frac{\cos\theta}{\cos\varphi}.$$

In the second case we must separate two regions of integration over θ:

The Self-Absorption Factor f for a Finite Cylindrical Source

μD \ H/D	0.25	0.50	0.75	1.00	1.25	1.50	1.75	2.00	2.25	2.50	∞
0	1.000	1.000	1.000	1.000	1.000	1.000	1.000	1.000	1.000	1.000	1.000
0.1	0.975	0.967	0.962	0.958	0.955	0.952	0.950	0.947	0.945	0.942	0.853
0.2	0.950	0.934	0.925	0.920	0.916	0.912	0.908	0.904	0.900	0.898	0.797
0.3	0.931	0.903	0.892	0.884	0.878	0.871	0.866	0.863	0.856	0.852	0.753
0.4	0.912	0.880	0.861	0.856	0.844	0.838	0.831	0.826	0.820	0.812	0.713
0.5	0.893	0.852	0.832	0.825	0.815	0.808	0.800	0.793	0.780	0.780	0.676
0.6	0.875	0.832	0.811	0.800	0.784	0.777	0.770	0.762	0.754	0.744	0.640
0.7	0.859	0.811	0.787	0.773	0.758	0.750	0.740	0.730	0.721	0.714	0.609
0.8	0.841	0.790	0.766	0.750	0.734	0.723	0.713	0.700	0.692	0.686	0.578
0.9	0.824	0.771	0.743	0.730	0.713	0.698	0.690	0.673	0.666	0.656	0.552
1.0	0.809	0.752	0.724	0.704	0.690	0.676	0.662	0.648	0.638	0.631	0.528
1.5	0.743	0.668	0.632	0.614	0.593	0.576	0.562	0.543	0.533	0.522	0.432
2.0	0.688	0.604	0.558	0.532	0.513	0.496	0.479	0.461	0.450	0.437	0.369
2.5	0.640	0.544	0.499	0.472	0.454	0.437	0.418	0.403	0.390	0.376	0.312
3.0	0.596	0.496	0.449	0.421	0.404	0.386	0.371	0.355	0.340	0.327	0.274
3.5	0.557	0.452	0.406	0.377	0.361	0.343	0.329	0.313	0.303	0.290	0.243
4.0	0.527	0.417	0.370	0.339	0.324	0.308	0.294	0.279	0.272	0.260	0.217
5.0	0.478	0.359	0.311	0.283	0.266	0.252	0.242	0.231	0.223	0.220	0.179
6.0	0.432	0.318	0.272	0.244	0.225	0.212	0.204	0.196	0.191	0.187	0.152
7.0	0.395	0.286	0.239	0.212	0.195	0.184	0.177	0.170	0.166	0.162	0.132
8.0	0.364	0.258	0.212	0.188	0.173	0.164	0.154	0.151	0.147	0.144	0.117
9.0	0.336	0.231	0.191	0.169	0.155	0.147	0.141	0.136	0.132	0.129	0.105
10	0.311	0.209	0.171	0.153	0.140	0.133	0.127	0.123	0.119	0.117	0.095
12	0.267	0.181	0.149	0.132	0.121	0.115	0.110	0.106	0.103	0.101	0.082
14	0.232	0.156	0.129	0.114	0.105	0.099	0.095	0.092	0.089	0.087	0.071
16	0.200	0.137	0.112	0.100	0.092	0.087	0.083	0.080	0.078	0.076	0.062
18	0.178	0.121	0.100	0.088	0.081	0.077	0.074	0.071	0.069	0.068	0.055
20	0.159	0.108	0.089	0.079	0.072	0.068	0.066	0.063	0.063	0.062	0.049
30	0.107	0.073	0.060	0.053	0.049	0.046	0.044	0.043	0.041	0.040	0.033
40	0.081	0.055	0.045	0.040	0.037	0.035	0.033	0.032	0.031	0.031	0.025
50	0.065	0.044	0.036	0.032	0.030	0.028	0.027	0.026	0.025	0.024	0.020
100	0.032	0.022	0.018	0.016	0.015	0.014	0.013	0.013	0.013	0.012	0.010

a) $\theta \leq \theta_0$,

b) $\theta \geq \theta_0$,

where $\theta_0 = \arccos \frac{H}{2D \tan \varphi}$.

In case a) the intersection point of OS, which is given in terms of the angles θ and φ, with the surface of the cylinder is in the plane of the top of the cylinder. Therefore the upper limit of integration over x is given by

$$x_1 = \frac{H}{2 \sin \varphi}.$$

In case b) the intersection point defining the upper limit of integration over x is again on the side surface of the cylinder, so that

$$x_1 = D \frac{\cos \theta}{\cos \varphi}.$$

After all these considerations, and after choosing the upper limit of integration over x, the integral in the numerator of Equation (7) can be written

$$\int_0^{\pi/2} \int_0^{\pi/2} \cos \varphi \cdot e^{-\mu x_1(\theta, \varphi)} \, d\varphi \, d\theta = \int_0^{\varphi_0} \int_0^{\pi/2} \cos \varphi \cdot e^{-\mu D \frac{\cos \theta}{\cos \varphi}} \, d\varphi \, d\theta +$$

$$+ \int_{\varphi_0}^{\pi/2} \int_0^{\theta_0} \cos \varphi \cdot e^{-\frac{\mu H}{2 \sin \varphi}} \, d\varphi \, d\theta + \int_{\varphi_0}^{\pi/2} \int_{\theta_0}^{\pi/2} \cos \varphi \cdot e^{-\mu D \frac{\cos \theta}{\cos \varphi}} \, d\varphi \, d\theta. \qquad (8)$$

The values of θ_0 and φ_0 depend on H/D.

Equations (7) and (8) give the self-absorption factor for a finite cylindrical source. The results of the calculation are shown in the table.

The tabulated results lead to the following conclusions:

1. The self-absorption factor for a finite cylinder and a given value of μD decreases as H/D increases. This can be explained by the increase in the relative role of the so-called "oblique" rays as H/D increases. This also explains why for large H/D the self-absorption factor decreases more rapidly with μD.

2. The self-absorption factor for a finite cylinder with a given value of μD approaches the value of f for an infinite cylinder as H/D is increased. Comparison of the results for finite and infinite cylinders* shows that with an accuracy of 5% the data for a cylinder with $H/D = \infty$ can be used for a cylinder with $H/D \geq 2.5$ for practically arbitrary μD (if conversion is used to account for purely geometrical factors).

3. As H/D is decreased the region in which one may neglect self-absorption ($f \approx 1$) for a finite cylindrical source moves towards higher values of μD.

LITERATURE CITED

[1] Radium Dosage, The Manchester System (Livingstone Ltd, Edinburgh 1947).

[2] R. Plesch, Strahlenther 97, 277 (1955).

[3] R.D. Evans and R.O. Evans, Rev. Mod. Phys. 20, 305 (1948).

[4] W. Mayneord, Brit. J. Radiology, Suppl. 2, 150 (1950).

[5] W. Mayneord and W.K. Sinclair, Advances in Biological and Medical Physics 3, 1 (Academic Press, Inc., New York 1953).

*The values of the self-absorption factor for an infinitely long cylindrical source are given in the last column of the table.

[6] W. Dixon, Nucleonics 8, No. 4, 68 (1951).

[7] E. Field, Nucleonics 11, No. 9, 66 (1953).

Received November 14, 1956

BLANK
PAGE

ATOMIC MASSES OF THE ISOTOPES C^{13}, N^{14}, N^{15}

R.A. Demirkhanov, T.I. Gutkin and V.V. Dorokhov

We present the results of new mass-spectrographic measurements of the atomic masses of C^{13}, N^{14} and N^{15}. We show the "internal consistency" for the mass values of these isotopes obtained from different sets of mass doublets. The measurements were performed under conditions eliminating systematic errors. We describe the method for precision adjustment of the ion-optical system. The values obtained for the masses of C^{13}, N^{14} and N^{15} are 13.007491 ± $3 \cdot 10^{-6}$ amu, 14.007527 ± $4 \cdot 10^{-6}$ amu and 15.004890 ± ± $5 \cdot 10^{-6}$ amu, which is in good agreement with the values recently published by Nier and co-workers. This data is higher than the average data obtained from nuclear reactions and by statistical analysis. The difference in the values is explained by the inexact measurement of the Q-values used in calculating the masses of the parent isotopes n_0, H, D, He^4 and C^{12}, and of the isotopes C^{13}, N^{14} and N^{15}.

INTRODUCTION

One of the fundamental ways of showing the absence of systematic errors in mass-spectrographic measurements of isotope masses is by so-called "internal consistency." This means that the mass values for a given isotope obtained by using different mass doublets in different combinations are in good agreement with each other. Up to the present time, internal consistency has not been obtained for the atomic masses of N^{14}, C^{13} or N^{15} [1]. The reason for this was the presence of systematic errors.

As a result of special investigations recently performed [2], it was established that systematic errors which destroy internal consistency can be caused both by insufficiently accurate adjustment of the ion-optical system, and by the action of the beam space charge and the fringing fields of the magnetic and electric lenses.

In the present work we present the results of new measurements of the atomic mass of N^{14}, which were performed under conditions in which the above factors were to a great extent eliminated or accounted for. In order to compare the results of our measurements with the values of the N^{14} mass obtained from nuclear reactions, we measured the atomic masses also of C^{13} and N^{15}. The experiments used gas mixtures enriched in these rare isotopes.

Adjustment of the Apparatus

In double-focusing mass-spectrographs, the parameters of the electric and magnetic lenses are related by [3]

$$r_{om}\left[(1-\cos\Phi_m)+\frac{l_{2m}}{r_{om}}\sin\Phi_m\right]+$$
$$+\left(\cos\Phi_m-\frac{l_{2m}}{r_{om}}\sin\Phi_m\right)\times$$
$$\times\left[r_{oe}(1-\cos\sqrt{2}\,\Phi_e)+l_{2e}\sqrt{2}\sin\sqrt{2}\,\Phi_e\right]=0,$$

where r_{om} is the radius of curvature of an ion in the magnetic lens; Φ_m is the angle subtended by the magnetic field; l_{2m} is the distance of the "image" from the edge of the magnetic field; r_{oe} is the radius of curvature

of an ion in the electric lens; Φ_e is the angle subtended by the electric lens; and l_{2e} is the distance of the electric lens "image" from the edge of the field.

In our instrument [4], when the principal points of the electric and magnetic cylindrical lenses are symmetrically located and when $\Phi_m = 60°$ and $\sqrt{2}\Phi_e = 90°$, then in order to obtain velocity focusing it is necessary that $r_{oe} = r_{om}$ and the angle of incidence of the beam on the electric and magnetic lenses be 90°.

It is not possible to attain these conditions with sufficient accuracy by mechanical adjustment of the instrument. Small deviations from a 90° angle may be unnoticed, since even for very narrow slits the beam will pass through the ion-optical system (because of the appropriate choice of the accelerating potential and the voltage applied to the cylindrical lens).

In this case the mean radius of curvature of the beam will differ from the calculated one, thus destroying velocity focusing (Figure 1).

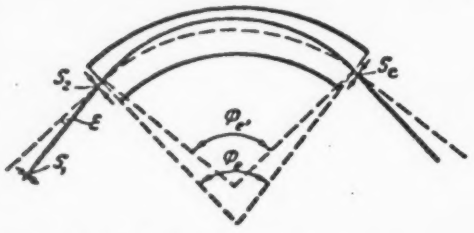

Fig. 1. Path of an ion beam in an unadjusted system.

The precision adjustment of the apparatus was attained in the following way. In addition to the 30μ aperture slit S_2 at the entrance to the electric lens, we placed another diaphragm with a slit S_e (of width 90μ and height 6 mm) at the exit from the electric lens. In order to avoid polarization, this diaphragm was heated. During the adjustment time, two 30μ thick tantalum wires, well insulated from each other and from the condenser casing, and with a separation of 150μ were attached at the center of the electric lens symmetrically with respect to its central surface. Each of these wires was attached to a vacuum-sealed lead, which in turn was attached to a low-current meter. During the adjustment the current on the wire was about $2 \cdot 10^{-8}$ amp. The fact that the wires were so thin and that they were so close together caused the field to be hardly altered by them even in the immediate neighborhood of the wires.

The measurement of the total beam current was performed with the aid of a special detector located near the image from the electric lens. The design of this system was such that the detector was inserted into the beam only during measurement.

As has been shown elsewhere [4], the velocity distribution of the ions in the beam for a plasma ion source is of the order of 2-6 v. For such a velocity distribution and for an accelerating voltage of 40 kev, the thickness of the central part of the beam is no greater than 60μ. Because the beam is so narrow and the current density is relatively high, its position can be rather well established with the aid of the above-mentioned wires.

The apparatus was adjusted in the following way. For a given accelerating voltage U_B, the voltage U_K applied to the plates of the electric lens was chosen so that after passing through slits S_2 and S_e, the beam would give a maximum current at the detector.

When the position of the beam is fixed, the potential across the plates of the electric lens is changed by an amount ΔU_K until the beam at the center is between the wires. The distance ΔY through which the beam has moved is then determined from ΔU_K by the relation

$$\Delta Y = r_{oe}\beta(1 - \cos\sqrt{2}\Phi_e) - \frac{\varepsilon_{1e}}{\sqrt{2}} r_{oe} \sin\sqrt{2}\Phi_e,$$

where

$$\beta = \frac{\Delta U_K}{U_K}.$$

When U_K is changed by ΔU_K, the beam passes between the wires so that $\Delta Y = 0$. From this we obtain the angle ε_{1e}:

$$\varepsilon_{1e} = \frac{\sqrt{2}\beta(1-\cos\sqrt{2}\Phi_e)}{\sin\sqrt{2}\Phi_e}.$$

Thus if we know ε_{1e} for a given l_{1e} (distance from slit S_1 to the aperture slit S_2), we can determine the distance Δx through which the input slit with the ion source must be moved perpendicular to the direction of the beam. Only in this way will the trajectory of the ion beam rigorously satisfy the requirements of double focusing.

EXPERIMENTAL RESULTS

The isotope N^{14}. The mass of N^{14} was measured from the following doublets:

$$N^{14}H_2 - O^{16},\ N_2^{14} - C^{13}O^{16},\ N^{14} - C^{12}H_2,$$
$$N_2^{14} - C^{13}N^{14}H_2,\ N^{14}H_2 - C^{12}H_4,$$
$$C^{12}O^{16} - C^{13}N^{14}H_2.$$

The values of ΔM obtained from these doublets are shown in Table 1.*

TABLE 1

Doublet	ΔM in 10^{-3} amu	Mean value
$N^{14} - C^{13}H_2$	12.574 ± 8	12.578 ± 4
$N^{14}H_2 - C^{13}H_4$	12.586 ± 7	
$N_2^{14} - C^{13}N^{14}H_2$	12.574 ± 4	
$N^{14}H_2 - O^{16}$	23.802 ± 16	23.808 ± 8
$C^{13}O^{16} - C^{13}N^{14}H_2$	23.815 ± 6	
$C^{12}O^{16} - N_2^{14}$	11.241 ± 5	$11\ 241 \pm 5$

TABLE 2

Doublet	Atomic mass of C_{12}
$N^{14} - C^{13}H_2$ ($M = 14$) $N^{14}H_2 - C^{13}H_4$ ($M = 16$) $N_2^{14} - C^{13}N^{14}H_2$ ($M = 28$)	14.007526 ± 6
$N^{14}H_2 - O^{16}$ ($M = 16$) $C^{13}O^{16} - C^{13}N^{14}H_2$ ($M = 28$)	14.007524 ± 8
$C^{13}O^{16} - N_2^{14}$ ($M = 28$)	14.007530 ± 5
Mean value	14.007527 ± 3

TABLE 3

Doublet	ΔM in 10^{-3} amu
$O^{16}H - N^{15}H_2$	13.037 ± 9
$N^{14}H_2 - N^{15}H_2$	10.781 ± 8
$C^{13}H_2 - N^{15}$	23.356 ± 5
$N^{14}H - N^{15}$	10.784 ± 5

TABLE 4

Doublet	Atomic mass of C_{12} amu
$C^{13}H - C^{13}$	13.007488 ± 6
$C^{13}H_4 - C^{13}H_3$	13.007494 ± 6
$C^{13}H_3 - C^{13}H_4$	13.007491 ± 7
Mean value	13.007491 ± 3

TABLE 5

Doublet	ΔM in 10^{-3} amu	Mean value of ΔM for all measurements in 10^{-3} amu
$C^{13}H - C^{13}$	$4,474 \pm 4$	$4,471 \pm 3$
$C^{13}H_2 - C^{13}H_3$	$4,468 \pm 5$	
$C^{13}H_4 - C^{12}H_3$	$4,471 \pm 9$	

TABLE 6

Doublet	Atomic mass of N_{15}, amu
$C^{13}H_2 - N^{15}$	15.004890 ± 7
$N^{14}H - N^{15}$	15.004885 ± 6
$N^{14}H_2 - N^{15}H_2$	15.004888 ± 9
$O^{16}H - N^{15}H_2$	15.004895 ± 9
Mean value	$15\ 004890 \pm 4$

The atomic mass of N^{14} as determined from these doublets is presented in Table 2. In calculating the atomic mass of N^{14}, we used the masses of C^{12}

*In all the tables the experimental error is given in 10^{-3} amu.

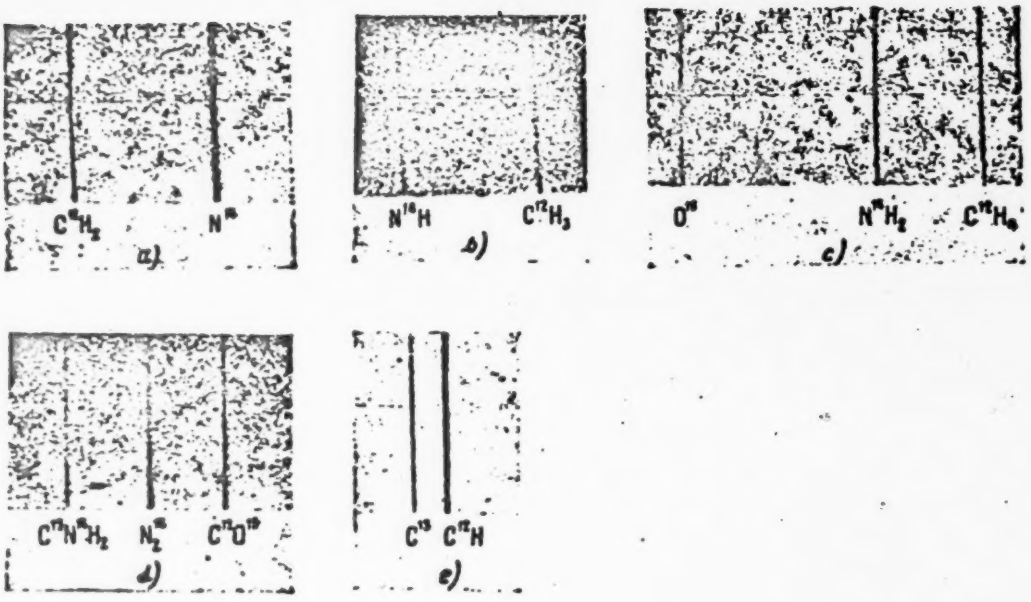

Fig. 2. Photographs of mass-spectrographic doublets: a) the doublet $C^{12}H_2-N^{14}$ (x55); b) the doublet $N^{14}H-C^{12}H_3$ (x65); c) the triplet $O^{16}-N^{14}H_2-C^{12}H_4$ (x45); d) the triplet $C^{12}N^{14}H_2-N_2^{14}-C^{12}O^{16}$ (x65); e) the doublet $C^{13}-C^{12}H$ (x35).

and H as determined previously by the authors [4], namely

$$M(C^{12}) = 12.003820 \pm 5. \quad M(H) = 1.008142 \pm 1.$$

The isotope C^{13}. The atomic mass of C^{13} was measured by introducing into the gas discharge region of the source a mixture of helium and methane enriched to 5-6% of C^{13}.

The atomic mass of C^{13} was determined from the doublets

$$C^{12}H - C^{13} \quad C^{13}H_3 - C^{12}H_6 \text{ and } C^{13}H_4 - C^{12}H_5.$$

The values of ΔM for these doublets are shown in Table 3.

The values of the atomic mass of C^{13} obtained from these doublets are shown in Table 4.

The isotope N^{15}. The atomic mass of N^{15} was measured by filling the ion source with a mixture of He^4 (80%), NH_3 (10%), CH_4 (10%) and using the following set of doublets:

$$N^{15}H_2 - O^{16}H, \; N^{15}H_2 - N^{14}H_3,$$
$$N^{15} - C^{12}H_3, \; N^{15} - N^{14}H.$$

The values of ΔM for these doublets are shown in Table 5.

The corresponding values for the atomic mass of N^{15} are shown in Table 6.

Several mass-spectrograph photographs of the doublets are shown in Figure 2.

DISCUSSION OF THE RESULTS

Tables 7 and 8 show the atomic masses of C^{13}, N^{14} and N^{15} as recently obtained both by mass-spectro-

graphic means and from nuclear reaction data. It is seen from Table 7 that the results of the present work are in good agreement with those of Nier and co-workers [5], but they differ from those of Ewald [6] and of Ogata and Matsuda [7].

TABLE 7

Atomic Masses of C^{13}, N^{14} and N^{15} as Obtained by Mass-Spectrographic Measurements, amu

Author	$M(C^{13})$	$M(N^{14})$	$M(N^{15})$
Ewald (1951) [6]	13.007538 ± 14	14.007525 ± 15	15.004928 ± 20
Ogata and Matsuda (1953)[7]	13.007505 ± 12	14.007550 ± 5	15.004902 ± 9
Kettner (1955) [12]	13.007511 ± 11	14.007545 ± 8	15.004875 ± 5
Nier and co-workers (1956)[5]	13.007492 ± 0,9	14.0075263 ± 0,8	15.004873 ± 0,4
Our results	13.007491 ± 3	14.007527 ± 4	15.004890 ± 5

TABLE 8

Atomic Masses of C^{13}, N^{14} and N^{15} from Nuclear Reaction Data, amu

Author	$M(C^{13})$	$M(N^{14})$	$M(N^{15})$
Li (1951-1952) [8]	13.007473 ± 14	14.007515 ± 11	15.004863 ± 12
Wapstra (1955) [9]	13.007478 ± 5	14.007520 ± 3	15.004862 ± 5
Drummond (1955) [10]	13.0074935 ± 2,8	14.0075270 ± 2,2	15.004883 ± 5
Our results	13.007491 ± 3	14.007527 ± 4	15.004890 ± 5

TABLE 9

Type of reaction	$M(C^{13})$
$C^{13}(n, \gamma)C^{13}$	13.007472 ± 8
$C^{13}(d, p)C^{13}$	13.007475 ± 6
Our results	13.007491 ± 3

In addition (Table 8), our results and Nier's [5] are higher than the averaged values of Li [8] and Wapstra [9], as calculated from nuclear reactions, as well as those of Drummond [10], which are obtained by statistical analysis of mass-spectroscopic and nuclear-reaction data. We note the fact that both in the present work and in the most recent measurements of Nier, whose results agree within the limits of experimental error, the results obtained are all internally consistent. This agreement for the atomic masses of isotopes obtained independently on two separate instruments and with internal consistency gives reason to believe that this data is reliable.

In all probability the differences between the atomic masses of C^{13}, N^{14} and N^{15} as obtained in the present work and as calculated from nuclear reactions must be explained by the inaccurate measurements of the Q-values used in calculating both the masses of the parent isotopes n_0, H, D, He^4 and C^{12}, as well as the isotopes C^{13}, N^{14} and N^{15}. For instance, for good agreement between the Q-values for the $C^{12}(n, \gamma)C^{13}$ and $C^{12}(d, p)C^{13}$ reactions, the experimentally obtained and theoretically calculated values for the atomic mass of C^{13} differ by more than the statistical error of measurement (Table 9). This is explained by the different masses of the parent isotopes, in particular of C^{12} [4].

In those cases when the masses of the parent isotopes are in agreement, as for instance in the $O^{16}(n, \alpha)C^{13}$ reaction, there is unfortunately a large error in the measured Q-value, so large, as a matter of fact, that the atomic mass of C^{13} differs not only from our value but also from values obtained from nuclear reaction data.

For N^{14}, the somewhat high disagreement of the Q-values for the $O^{18}(d, \alpha)N^{14}$ reaction is compensated by the differences in the atomic masses of D and He^4, so that in the final analysis the disagreement in the N^{14} mass

TABLE 10

Q-Values for C^{13}

Reaction	Author	Q-value, Mev	Q-value as calculated from our data
$C^{13}(n, \gamma)C^{13}$	Kinsey (1953) [13]	4.949±0,006	4.948±0.006
$C^{13}(d, p)C^{13}$	Hatner (1951) [14]	2.722±0,003	2.722±0.006
$C^{13}(d, p)C^{13}$	Famularo (1953) [15]	2.722±0,004	2.722±0.006
$C^{13}(p, \gamma)N^{14}$	Lauritsen (1940) [16]	7.62±0,08	7.548±0.005
$C^{13}(d, n)N^{14}$	Mandeville (1950) [17]	5.17±0,05	5.322±0.006
$C^{13}(\alpha, n)O^{16}$	Jones (1951) [18]	2.06±0,16	2.214±0 005
$N^{13}(d, \alpha)C^{13}$	Malm (1951) [19]	7.681±0,009	7.694±0.007
$O^{16}(n, \alpha)C^{13}$	Huber (1951) [20]	−2,38±0,16	−2.214±0.006

TABLE 11*

Comparison of the Values for the Atomic Mass of C^{13}

Reaction	Author	Atomic mass of C_{13} in terms of other masses	Atomic mass of C_{13}
$C^{12}(n, \gamma)C^{13}$	Kinsey (1953) [13]	C^{12}+1.003670±6 (1.003671±6)	13.007473±8
$C^{13}(d, p)C^{13}$	Hatner (1951) [14]	C^{13}+1.003672±4 (1.003671±6)	13.007475±6
$C^{13}(d, p)C^{13}$	Famularo (1953) [15]	C^{13}+1.003672±4 (1.003671±6)	13.007475±6
$C^{13}(p, \gamma)N^{14}$	Lauritsen (1940) [16]	N^{14}−0.999962±80 (1.000036±5)	13.007558±80
$C^{13}(d, n)N^{14}$	Mandeville (1950) [17]	N^{14}−1.000202±50 (1.000036±5)	13.007318±50
$C^{13}(\alpha, n)O^{16}$	Jones (1951) [18]	O^{16}−2.992675±160 (2.992509±3)	13.007325±160
$N^{13}(d, \alpha)C^{13}$	Malm (1951) [19]	N^{13}−1.997382±9 (1.997399±6)	13.007480±10
$O^{16}(n, \alpha)C^{13}$	Huber (1951) [20]	O^{16}−2.992331±160 (2.992509±3)	13.007669±160
Our data			13.007491±3

TABLE 12

Q-Values for N^{14}

Reaction	Author	Q-value, Mev	Q-value as calculated from our data
$N^{14}(n, \gamma)N^{15}$	Kinsey (1953) [21]	10 832±0.008	10.822±0 008
$N^{14}(d, \alpha)C^{12}$	Holloway (1940) [22]	13.39±0.08	13.568±0.008
$N^{14}(d, p)N^{15}$	Mielkowsky (1952) [23]	8.613±0.011	8.596±0.007
$N^{14}(d, p)N^{15}$	van Patter (1954) [11]	8.614±0.007	8.596±0.007
$C^{13}(p, \gamma)N^{14}$	Lauritsen (1940) [16]	7.62±0.08	7.548±0.005
$C^{13}(d, n)N^{14}$	Mandeville (1950) [17]	5.17±0.05	5.322±0.005
$O^{16}(d, \alpha)N^{14}$	Famularo (1953) [15]	3.119±0.005	3.107±0 006
$O^{16}(d, \alpha)N^{14}$	van Patter (1954) [11]	3.115±0.002	3.107±0.006

lies within the limits of statistical error. The value of $M(N^{14})$ obtained from other reactions disagree among themselves, to a great extent, as well as with our data.

TABLE 13

Comparison of the Values for the Atomic Mass of N^{14}

Reaction	Author	Atomic mass of N_{14} in terms of other masses	Atomic mass of N_{14}
$N^{14}(n, \gamma)N^{15}$	Kinsey (1953) [21]	$N^{15}-0.997353\pm10$ (0.997363 ± 6)	14.007509 ± 11
$N^{14}(d, \alpha)C^{12}$	Holloway (1940) [22]	$C^{12}+2.003513\pm9$ (2.003707 ± 6)	14.007306 ± 10
$N^{14}(d, p)N^{15}$	Mileikowsky (1952) [23]	$N^{15}-0.997345\pm11$ (0.997363 ± 6)	14.007517 ± 11
$N^{14}(d, p)N^{15}$	van Patter (1954) [11]	$N^{15}-0.997344\pm8$ (0.997363 ± 6)	14.007518 ± 9
$C^{13}(p, \gamma)N^{14}$	Lauritsen (1940) [16]	$C^{13}+0.999962\pm80$ (1.000036 ± 5)	14.007440 ± 80
$C^{13}(d, n)N^{14}$	Mandeville (1950) [17]	$C^{13}+1.000202\pm50$ (1.000036 ± 5)	14.007680 ± 50
$O^{16}(d, \alpha)N^{14}$	Famularo (1953) [15]	$O^{16}-1.992482\pm5$ (1.992473 ± 4)	14.007518 ± 5
$O^{16}(d, \alpha)N^{14}$	van Patter (1954) [11]	$O^{16}-1.992478\pm3$ (1.992473 ± 4)	14.007522 ± 3
Our data			$14,007527\pm4$

TABLE 14

Q-Values for N^{15}

Reaction	Author	Q-value, Mev	Q-value as calculated from our data
$C^{12}(\alpha, p)N^{15}$	van Patter (1954) [11]	-4.961 ± 0.003	-4.972 ± 0.008
$N^{14}(n, \gamma)N^{15}$	Kinsey (1953) [21]	10.832 ± 0.008	10.822 ± 0.006
$N^{14}(d, p)N^{15}$	van Patter (1954) [11]	8.614 ± 0.007	8.596 ± 0.007
$N^{14}(d, p)N^{15}$	Mileikowsky (1952) [23]	8.613 ± 0.011	8.596 ± 0.007
$N^{15}(p, \alpha)C^{12}$	Li (1951) [8]	4.961 ± 0.003	4.972 ± 0.008
$N^{15}(d, \alpha)C^{13}$	Malm (1951) [19]	7.681 ± 0.009	7.694 ± 0.007
$N^{15}(d, n)O^{16}$	Worth (1950) [24]	10.900 ± 0.5	9.908 ± 0.005

TABLE 15

Comparison of the Values for the Atomic Mass of N^{15}

Reaction	Author	Atomic mass of N_{15} in terms of other masses	Atomic mass of N_{15}
$C^{12}(\alpha, p)N^{15}$	van Patter (1954) [11]	$C^{12}+3.001056\pm4$ (3.001070 ± 7)	15.004859 ± 6
$N^{14}(n, \gamma)N^{15}$	Kinsey (1953) [21]	$N^{14}+0.997353\pm8$ (0.997363 ± 6)	15.004873 ± 9
$N^{14}(d, p)N^{15}$	van Patter (1954) [11]	$N^{14}+0.997344\pm7$ (0.997363 ± 6)	15.004864 ± 8
$N^{14}(d, p)N^{15}$	Mileikowsky (1952) [23]	$N^{14}+0.997343\pm11$	15.004863 ± 11
$N^{15}(p, \alpha)C^{12}$	Li (1951) [8]	$C^{12}+3.001056\pm4$ (3.001070 ± 7)	15.004859 ± 6
$N^{15}(d, \alpha)C^{13}$	Malm (1951) [19]	$C^{13}+1.997382\pm9$ (1.997399 ± 6)	15.004860 ± 10
$N^{15}(d, n)O^{16}$	Worth (1950) [24]	$O^{16}-0.994044\pm500$ (0.995110 ± 5)	15.005956 ± 500
Our data			15.004890 ± 5

Tables 10, 12 and 14 give the Q-values as obtained from nuclear reactions [11] and as calculated from our data. As can be seen from Tables 11, 13 and 15, even when there is good agreement for the Q-values, due to the disagreement in the masses of the parent isotopes, the masses of the resulting isotopes do not agree.

Comparison of the results of various nuclear reactions show that the distribution of the isotope mass values as calculated from these reactions is quite high. The corresponding disagreements are well outside of the limits of statistical error.

The question of how to perform the averaging and how to choose the final data in order to determine isotope masses from nuclear reaction data requires further investigation.

In conclusion the authors express their gratitude to L.G. Gvertseteli and V.K. Tskhakaia for making available the enriched C^{13} isotope, as well as to P.S. Brostiuk and M.I. Dzkuia for practical help with the work.

LITERATURE CITED

[1] J. Mattauch and R. Bieri, Z. Naturforsch. 9a, 303 (1954).

[2] T.I. Gutkin, "Errors in the Mass-Spectrographic Method of Measuring Isotope Masses" (in press).

[3] J. Mattauch and R. Herzog, Z. Phys. 89, 786 (1934).

[4] R.A. Demirkhanov, T.I. Gutkin and V.V. Dorokhov, J. Atomic Energy No. 2, 21 (1956).*

[5] T. Scolman, K. Quisenberry and A. Nier, Phys. Rev. 102, 4, 1076 (1956).

[6] H. Ewald, Z. Naturforsch. 601, 293 (1951).

[7] K. Ogata and H. Matsuda, Phys. Rev. 89, 27 (1953).

[8] C. Li, W. Whaling, W. Fowler and C. Lauritsen, Phys. Rev. 83, 512 (1951).

[9] A. Wapstra, Physica 21, 5, 367 (1955).

[10] Drummond, Phys. Rev. 97, 1004 (1955).

[11] D. van Patter, Rev. Mod. Phys. 26, 4, 402 (1954).

[12] M. Kettner, Phys. Rev. 102, 1065 (1956).

[13] B. Kinsey and G. Bartholomew, Can. J. Phys. 31, 1051 (1953).

[14] E. Hatner, Brookhaven National Laboratory, BNL-117 (August, 1951).

[15] K. Famularo and G. Phillips, Phys. Rev. 91, 1195 (1953).

[16] C. Lauritsen and W. Fowler, Phys. Rev. 58, 133 (1940).

[17] C. Mandeville and C. Swann, Phys. Rev. 79, 787 (1950).

[18] G. Jones and D. Wilkinson, Proc. Phys. Soc. 64A, 756 (1951).

[19] R. Malm and W. Buechner, Phys. Rev. 81, 519 (1951).

[20] P. Huber, E. Baldinyer and W. Proctor, Helv. Phys. Acta 24, 302 (1951).

[21] B. Kinsey and G. Bartholomew, Can. J. Phys. 31, 537 (1953).

[22] M. Holloway and B. Moore, Phys. Rev. 58, 847 (1940).

[23] C. Mileikowsky and W. Whaling, Phys. Rev. 88, 1254 (1952).

[24] D.C. Worth, Phys. Rev. 78, 378 (1950).

Received December 29, 1956

*[Original Russian pagination. See C.B. Translation pagination.]

LETTERS TO THE EDITOR

A LINEAR-CYCLIC ACCELERATOR

D.M. Zorin, O.S. Milovanov and A.V. Shalnov

Current linear accelerators are technically highly developed instruments, but the acceleration length must be large and the high-frequency source power correspondingly high if high energies are required. This is because the accelerated particles pass through the high-frequency field only once. The high energy transfer obtainable in a linear accelerator would enable one to balance the radiation losses easily if it were used as a resonator in a cyclic accelerator. The use of a linear accelerator as a resonator in systems where the magnetic field increases with time (synchrotron) is difficult because very high rates of change of magnetic field are required.

In 1954 Valdner [1] proposed a design in which a linear accelerator was used repeatedly. This was termed a "linear-cyclic" accelerator (elutron). Like the microtron [2] it uses the multiple resonance principle, and differs from the microtron with sectional magnets previously proposed by Stringer [3], using a reversing magnetic system. The elutron design differs from the above in that high magnetic fields can be used (as will be shown below) and that the weight of the reversing system is reduced.

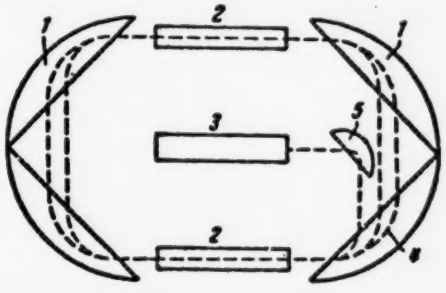

Scheme of the linear-cyclic accelerator: 1) magnetic deflectors; 2) linear accelerators; 3) injector linear accelerator; 4) electron trajectories; 5) magnetic deflector for particle injection.

The elutron contains two linear accelerators and a system of magnetic deflectors which cause particles of different energies to pass along the linear accelerator axes, and an injector which injects relativistic electrons into the orbit (see figure). The magnet system contains four magnets, each deflecting the beam through 90°. A uniform steady magnetic field acts normal to the orbit plane, the particle paths being at 45° to the edges of the magnetic deflectors. If the leakage field is neglected the relativistic particles describe a quarter-circle of radius

$$R = E/eH, \qquad (1)$$

where e is the electronic charge, H is the magnetic field strength, and E the total energy of an electron.

Particles of varying energies describe quarter-circles of radii defined by (1), and emerge as a broad beam from the first deflector. The second deflector is at 45° to the axis of this beam and turns it through 90°, focusing the particles into a narrow beam.

By using a second analogous system of magnetic deflectors, particles with various energies can be constrained to move in closed orbits arranged around the axes of the linear accelerators. If the accelerator is to accelerate particles of various energies, the speed of propagation of the accelerating wave in the waveguide must be equal to that of light. When such a system is used to accelerate particles there has to be a definite relation between the generator frequency and the time taken to traverse the orbit.

It may readily be shown that the requisite energy increment in an orbital accelerator is given by

$$\Delta E = \frac{em\lambda H}{\pi - 2}, \qquad (2)$$

where m is an integer, and λ is the generator wavelength.

This relation shows that the magnetic field strength depends on the energy increment in the linear accelerators and can be of the same order as in other accelerators.

A study of the accelerator's phase properties shows that the phase oscillation equation is similar to that for the microtron. The linear accelerators can be replaced by equivalent resonators.

Computations on the particle motions by Sternheimer's method [4] show that the motion in this system can be stable if the focusing properties of the leakage field and four quadrupole magnetic lenses at the linear accelerator inputs and outputs are used.

A deflector is used to inject electrons into the orbit.

The above linear-cyclic accelerator design is of definite interest. A preliminary theoretical analysis of the accelerator operation shows that a number of problems must be resolved by experiment. It is proposed to perform the experiments on a model under construction which would accelerate electrons to 20 Mev.

LITERATURE CITED

[1] O.A. Valdner, Affidavit (testifying to a refinement) No. 0608 (1954).

[2] V.I. Veksler, Proc. Acad. Sci. USSR 43, 8, 364 (1944).

[3] L. Shiff, Rev. Sci. Instr. 17, 6 (1946).

[4] R. Sternheimer, Rev. Sci. Instr. 23, 629 (1952).

Received November 9, 1956

THE NEUTRON-CAPTURE SEQUENCE IN ANTIMONY

A.N. Murin, V.D. Nefedov, D.K. Popov and V.I. Baranovsky

When antimony is irradiated in a sufficiently high neutron flux double neutron capture can occur.

$$Sb^{123} \xrightarrow{(n,\gamma)} Sb^{124} \xrightarrow[(T=60\ days]{(n,\gamma)} Sb^{125} (T=2{,}7 years \qquad (1)$$

Sb^{125} decays by β-emission to Te^{125m} (58 days) which is an isomer of stable Te^{125} [1]. Antimony specimens irradiated for a year (to allow enough Te^{125m} to accumulate) gave Te^{125m} on working-up. Stable Te was used as carrier. Tellurium metal was separated from antimony by reduction with stannous chloride. A high Te^{125m} activity was observed in the separated tellurium, identified from the half-life (57 ± 4 days), from its accumulation in the antimony, and from the absorption curve in aluminium for the internal conversion electrons, which agreed with the published one [2]. Thus, we may assume the above double capture sequence as proven.

An attempt was made to estimate the capture cross section of Sb^{124} for pile neutrons. The decay rates of Sb^{124} and Sb^{125} at the end of irradiation were determined by the defined solid angle method (the latter from the Te^{125m} activity). The activation cross section for Sb^{124} calculated in this way was about $2 \cdot 10^3$ barn.

LITERATURE CITED

[1] G. Seaborg, I. Perlman and J. Hollender, Table of Isotopes (Foreign Lit. Press, Moscow 1956).

[2] G. Friedlander, M. Goldhaber and G. Scharff-Goldhaber, Phys. Rev. 74, 981 (1948).

Received January 26, 1957

EXPERIMENTAL DETERMINATION OF THE YIELD OF γ-RADIATION FROM EXTENDED SOURCES

E.E. Kovalev, V.I. Popov, L.N. Smirenny and Yu.S. Khokhlov

In many cases, it is necessary to know the yield of γ-radiation from sources of different shapes and often of fairly large dimensions ("extended sources" of γ-radiation). Such a problem arises, e.g., in the use of sources of γ-radiation for irradiation, in designing shields for apparatus used in the radiochemical industry, etc.

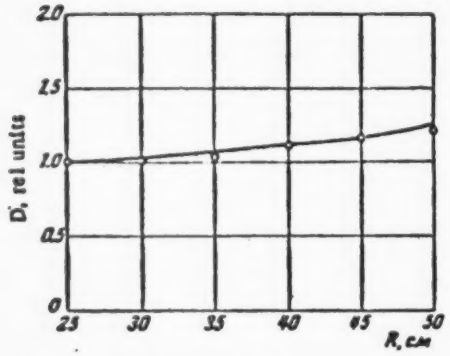

Fig. 1. Modeling of a source distributed over a circumference. The solid line curve was obtained by calculation; the points represent experimental results.

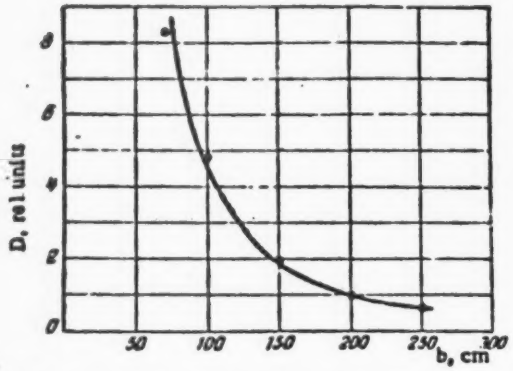

Fig. 2. Modeling of a hollow cylindrical source. The solid line curve was obtained by calculation; the points represent experimental results.

The variety of shapes, dimensions and conditions of use of extended sources necessitates suitable experiments in each particular case. It is obvious that this may be difficult. Indeed, a number of factors which determine the yield of γ-radiators are operative jointly. In many cases, where it is necessary to take into account, for instance, the influence of the geometric factor, it is equally necessary to allow for the effect of self-absorption and multiple scattering of the γ-radiation in the source. This means that actual extended sources cannot be used for determining experimentally the manner in which the factors influencing the yield of γ-radiation depend upon the parameters of the source.

In the method proposed, which is based on the construction of a model of the extended source, the influence of any one factor on the yield of γ-radiation can be investigated individually by experiment. The method can be applied to any extended or distributed source, provided it is possible to find a differential element (volume, surface, etc.), the movement of which in space reproduces the total volume of the extended source or the surface of the distributed source.

It is of particular interest to know the yield of γ-radiation of extended or distributed sources which are solids or figures of revolution.

We shall consider in the first place the model of an extended source without self-absorption or multiple scattering.

For a given extended source, there is a differential element of volume, the rotation of which about the axis of the source will reproduce the total volume of the source. If the element of vol-

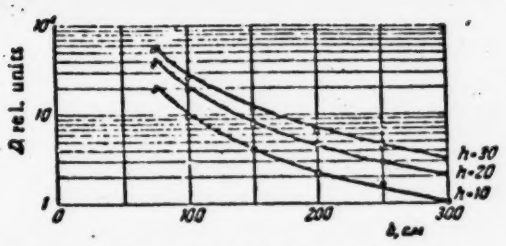

Fig. 3. Modeling of a solid cylindrical source. Solid line curves obtained by calculation; the points represent experimental results.

ume is selected so that self-absorption and multiple scattering of γ-radiation in it can be neglected (and obviously this can always be done), the model of the body of revolution will be free from these factors. The yield of γ-radiation from such a body of revolution will be determined solely by the geometric factor.

The application of this model method to some sample forms of source will be considered. If the radioactive substance is distributed uniformly over a circumference or a cylindrical surface, models of such sources can be made in the first place by the rotation of a point source and in the second case by that of a line source of a length equal to the height of the cylinder. A model of a solid cylindrical source without self-absorption and multiple scattering, can be made by rotating a cylindrical sector of small angle of aperture about the axis of the cylinder. The angle is selected so that self-absorption and multiple scattering of the γ-radiation in the cylindrical sector can be ignored. Furthermore, if the activity of the element of revolution is equal to the total activity of the modeled source, the dose of γ-radiation at any point for a given interval of time will be the same in both cases. It is also obvious that the dose of γ-radiation does not depend upon the number of revolutions or the speed of rotation of the model if, during the period of measurement of the dose, a whole number of revolutions is made and the rotation is uniform.

The model method may also be employed for investigating the influence of self-absorption and multiple scattering on the yield of γ-radiation from an extended source. In this case, the rotation of the model, for example a cylindrical sector, should take place in a cylindrical container of corresponding dimensions, filled with an absorbent and scattering inactive medium.

The experiments we have made to assess the model method have given satisfactory results and confirmed the possibility of utilizing the method in practice. Figure 1 shows the results of making a model of a source distributed over a circumference. The dose of γ-radiation was measured at a distance b = 100 cm from the center of rotation in the plane of rotation. Co^{60} was used as source of γ-radiation. For comparison, Figure 1 shows the calculated curve for the dose of γ-radiation from a source distributed over a circumference plotted against the radius R of the circumference. In both cases, the unit is the dose of γ-radiation at the point b = = 100 cm for R = 25 cm. It will be seen from Figure 1, the agreement between these results is perfectly satisfactory within the limits of experimental error, which was about 5% in all the experiments described.

Figure 2 shows similar results for a source distributed over a cylindrical surface (hollow cylinder). In this case, the model was made by rotation of a line source (a thin-walled tube, diameter 2 mm, filled with a solution of a salt of Co^{60} in water) of a length equal to the height of the cylinder (h = 50 cm) about the axis of a cylinder of radius R = 50 cm. For comparison, Figure 2 gives the calculated curve for the dose of γ-radiation from a hollow cylindrical source (h = 50 cm, R = 50 cm) plotted against distance to the center of the source. In this case also, satisfactory agreement may be observed between the experimental results and calculation.

Finally, Figure 3 compares the experimental results with the calculated values of the dose of γ-radiation for a solid cylindrical source (R = 50 cm) without self-absorption. In this case, the model was made by means of a vessel in the form of a cylindrical sector made of plexiglass, having an angle of aperture of about 1.5° and a radius of 50 cm. This vessel was filled with a solution of a salt of Co^{60} in water. The calculated curves show the dependence of the dose of γ-radiation upon the distance b to the axis of the cylinder in the basal plane of the cylinder for different values of its height h. The unit is the dose of γ-radiation for b = 300 cm and h = = 10 cm. In this case also, the agreement between the experimental data and the calculated results can be regarded as satisfactory.

Received April 21, 1956

THE EFFECT OF EXTENT OF PLANE SOURCE ON THE ATTENUATION OF γ-RAYS IN SHIELDING

E.E. Kovalev and D.P. Osanov

All sources of γ-radiation that are encountered in practice are to some degree extended sources, that is, they often possess appreciable dimensions. To such sources of radiation may be referred the core of a reactor, elements of the cooling system of the reactor, apparatus employed in radiochemistry and so on.

Although the emission of radiation from sources of this type, at least for the more simple geometri is known, the law for attenuation of γ-radiation from extended sources with consideration of multiple scattering in shielding, has not up to now been established [1]. It is of interest, to theoretically evaluate the effect of the extent of a source on the attenuation of γ-radiation. This is particularly desirable because the law of attenuation for a point source yields the lowest rate of reduction of radiation dose rate in shielding, and therefore the consideration of the effect of source geometry will allow a decrease in shield thickness [2].

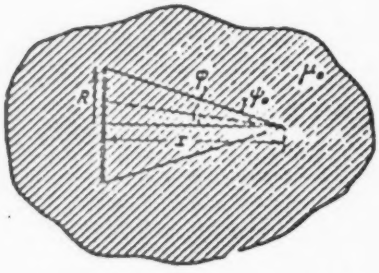

Fig. 1. Calculation of attenuation of γ-radiation from a disc with multiple scattering in the shield considered.

The basic difficulty of a theoretical consideration of γ-ray attenuation from a geometric source, with consideration of multiple scattering in shielding, is occasioned by the circumstance that the build-up factor, B, is a complicated function of the quantity $\mu_0 x$ (μ_0 is the absorption coefficient for γ-radiation, that is, the sum of macroscopic cross sections for photoelectric effect, Compton effect, and pair production, and x is the thickness of shield), the atomic number of the shield material Z, and of hν, the γ-ray energy. In some cases there are no analytical expressions for radiation emission of geometric sources even without consideration of multiple scattering.

For several source geometries there are analytical expressions not only for emission of γ-rays, but also for the law of attenuation (without consideration of multiple scattering) of γ-rays in shielding. (Line, disc and some other sources.) It is possible to theoretically analyze the attenuation of γ-rays for these sources with consideration of source geometry and multiple Compton scattering in shielding, if the complex relation $B = B(\mu_0 x, Z, h\nu)$ can be stated in analytical form.

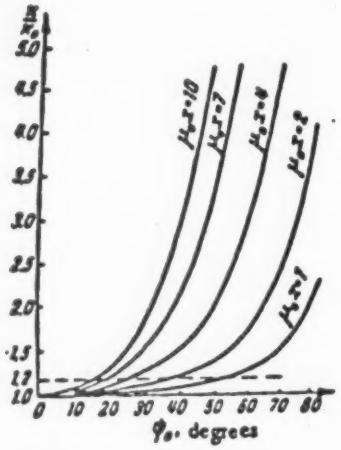

Fig. 2. Relative attenuation factor for γ-radiation for various thicknesses of shielding materials with low and medium Z.

A series of works [3, 4] give approximated analytical expressions, for the build-up factor of point isotropic sources in infinite media, of the linear form ($B = B \cdot \mu_0 x$) and of the exponential form ($B = B(\mu_0 x)^3$) functions of the shield thickness. Representation of the build-up factor by a linear function of the shield thickness is justifiable for small thicknesses, intermediate and heavy elements, and energies of radiation from 1 to 4 Mev [5]. In light elements the build-up factor rises more rapidly than is represented by a linear function. In these cases it is pos-

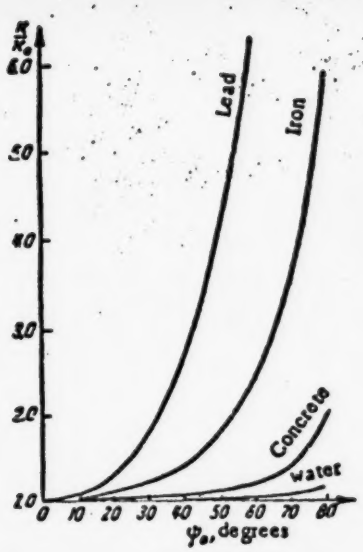

Fig. 3. Relative attenuation factor for γ-rays of 0.5 Mev energy in various shielding materials. Shield thickness x = 5 cm.

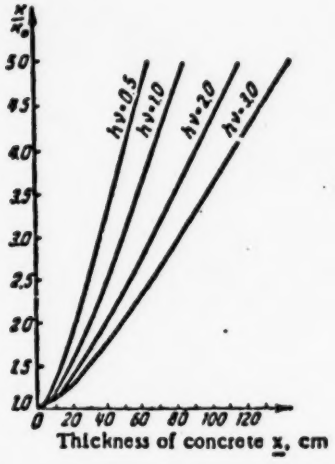

Fig. 4. Relative attenuation factor for γ-rays of various energies vs. concrete thickness $\varphi_0 = 50°$.

sible to use the exponential of the form $B = \beta(\mu_0 x)^{\beta}$, where β, as above, depends on the energy and on the atomic number of the material. However, both of these expressions are correct only for small values of $\mu_0 x$ and are usable in small intervals of values of Z and hν.

A more universal expression for build-up factor is the form

$$B = \sum_{i=1}^{i=n} A_i e^{-\alpha_i \mu_0 x}, \qquad (1)$$

where $A_i = A_i(h\nu, Z)$; $\alpha_i = \alpha_i(h\nu, Z)$.

It has been established [6], that it is possible, without great loss of accuracy to limit the evaluation to only two terms of this summation

$$B = A_1 e^{-\alpha_1 \mu_0 x} + A_2 e^{-\alpha_2 \mu_0 x}, \qquad (2)$$

where

$$A_2 = 1 - A_1.$$

An approach of this type ensures a wide interval of values for Z, $\mu_0 x$ and hν in which the build-up factors apply [5].

Below are given the results of our theoretical analysis of the effect of extent of a plane source, in the form of an infinite thin disc, on the attenuation of γ-radiation in shielding with consideration of multiple scattering. For this we used an expression for the build-up factor in the form of a sum of exponentials.

Let us examine the emitting disc of radius R, immersed in an infinite absorbing and scattering medium with absorption coefficient of μ_0 (Figure 1), whose extent is measured by the angle φ.

The γ-dose rate P, at a point a distance x from the disc and lying on the normal to the disc at its center, with multiple scattering considered, can be represented in the following form:

$$P = 2\pi P_\gamma \eta \int_0^{\varphi_0} \operatorname{tg} \psi e^{-\mu_0 x \sec \psi} B(\mu_0 x \sec \psi)\, d\psi, \qquad (3)$$

where P_γ is the γ-isotope constant; η is the surface activity density.

Since in this case both the source and given point are in an infinite medium, we can use the analytical expression for build-up factor B in the form of a sum of exponentials. Introducing (2) and (3) and using the exponential integral functions $E_i(-x)$, we get:

$$P = 2\pi P_\gamma \eta \{A_1 [E_i(-\mu' x \sec \psi_0) - E_i(-\mu' x)] + (1 - A_1)[E_i(-\mu'' x \sec \psi_0) - E_i(-\mu'' x)]\}, \qquad (4)$$

where $\mu' = (1 + \alpha_1)\mu_0$ and $\mu'' = (1 + \alpha_2)\mu_0$.

In the special case when $B = 1$ ($\alpha_1 = \alpha_2 = 0$) which corresponds to neglect of multiple scattering, we ob-

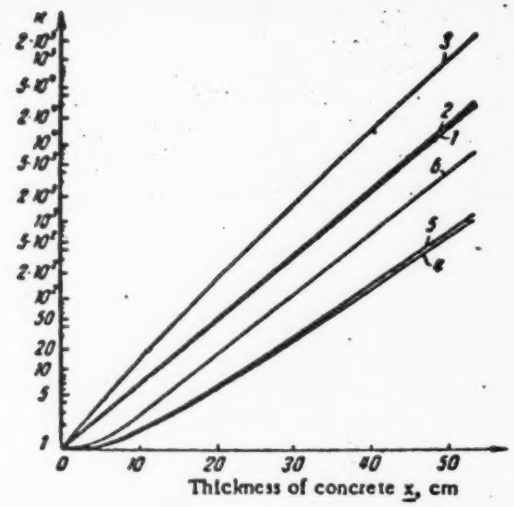

Fig. 5. Attenuation factor as a function of concrete thickness for point source and disc emitter.

tain the well-known formula for emission of a disc immersed in absorbing medium [1]. Defining the attenuation factor k in the shielding as the ratio of γ-dose rate at the given point without shielding, to the dose rate at the same point with shielding, we can write

$$k = \frac{\ln \sec \psi_0}{A_1 [E_i(-\mu' x \sec \psi_0) - E_i(-\mu' x)] + (1-A_1)[E_i(-\mu'' x \sec \psi_0) - E_i(-\mu'' x)]}. \qquad (5)$$

This expression contains the tabulated functions $E_i(-x)$ and the tabulated values A_1, α_1 and α_2 [6].

We evaluated[by means of Equation (5)] the attenuation factors for several materials (water, concrete, iron and lead) with energies of γ-rays from 0.5 to 3.0 Mev. The results of the calculations are shown in Figures 2 to 5. Along the ordinates of Figures 2 to 4 are plotted the relationships of attenuation factors k for a disc to the attenuation factors k_0 for a point source, with multiple scattering considered in both cases. This ratio will further be called the relative attenuation factor. Introduction of the value k/k_0 gives the opportunity to plot curves for various $\mu_0 x$ to one scale, which is convenient for comparisons and evaluations of effect of extent of the source disc. This also allows (using the plotted curves and the well-known values of attenuation factors for point sources) the simple identification of attenuation factors for the source disc (for point source $k/k_0 \equiv 1$). In addition, this choice of coordinates allowed plotting one graph for all shielding materials with low and medium values of Z, since the dependence of attenuation factor on atomic number of the material (up to Z = 26 inclusive) and on energy of γ-radiation (in the interval $h\nu$ from 0.5 to 3.0 Mev) was found to be invalid. Maximum divergence of values of relative attenuation factors, for various materials and energies in the indicated range, does not exceed 15% for large angles ψ_0. This condition allows the use, in practice, of the same graph for most shielding materials.

With the aid of Figure 2 it is possible to draw some conclusions on the effect of extent of the source on the attenuation factor for γ-rays in shielding. Let us consider in the following that the effect of extent of the source is tangible if the relative attenuation factor $k/k_0 \geq 1.2$, that is, if the attenuation of the γ-radiation from a disc is 20% greater than the attenuation of the radiation from a point source. From the curves of Figure 2, we see that the effect of source extent is tangible for shield thicknesses $\mu_0 x = 1$ when $\psi_0 \geq 55°$, for $\mu_0 x = 2$ when $\psi_0 \geq 40°$ and etc. Conversely, for values of angle ψ_0 less than indicated above, the source disc can be considered as a point source. So, for example, for shield thickness $\mu_0 x = 10$ and angle $\psi_0 = 45°$, $k/k_0 = 4$. This means that the attenuation of the radiation from a disc, viewed from a point at distance $\mu_0 x = 10$ from its center at an angle of $\psi_0 = 45°$, is 4 times greater than the attenuation of γ-radiation from a point source. On the other hand, for $\mu_0 x = 2$ and $\psi_0 = 30°$, $k/k_0 = 1.1$, that is the attenuation of the radiation from a disc

is almost identical with the attenuation of γ-radiation from a point source.

In Figure 3 are shown curves of relative attenuation factors for γ-rays of 0.5 Mev energy, in various shielding materials of equal thickness (5 cm).

In Figure 4 are shown curves of relative attenuation factors of γ-rays with various energies hν versus thickness of concrete. All curves are for the angle $\phi_0 = 50°$.

The nature of the curves of Figures 2 to 4 can be explained in the following manner. As the disc dimensions increase (increase of ϕ_0) the relative importance of so-called "slant" rays increases. The greater attenuation of slant rays produces the effect that the attenuation factor for the disc overall increases as compared to a point source. Also the relative attenuation factor increases as ϕ_0 increases. Inclusion of the effect of multiple scattering always results in a reduction of the attenuation factor. But the effect of multiple scattering on the attenuation of γ-rays from a disc source is different from the effect on attenuation of rays from a point source. In the disc case there are slant rays which pass through relatively large distances in shielding, which results in increased effect of multiple scattering. Therefore, the relative attenuation factor, with multiple scattering considered, grows smaller, and the more so as the build-up factor for the medium increases and as the γ-ray energy increases.

With these considerations it is easy to explain the trend of the curves in Figures 3 and 4. It is indeed true that the relative attenuation factor for equal thicknesses of different shielding materials is smaller the greater the build-up factor for the material (Figure 3), and the greater the energy of the γ-rays (Figure 4).

In Figure 5 the curves of the attenuation factor of a disc and a point source are compared and the effect of multiple scattering on both attenuation factors is shown. The curves are for concrete shield material and γ-ray energies of 0.5 Mev, and are plotted on a semilogarithmic scale. The calculations were carried out according to the following formulas:

a) for point source without consideration of multiple scattering (Curve 1)

$$k = e \exp(\mu_0 x);$$

b) for disc source, subtended from the given detector point by the angle ϕ_0, without consideration of multiple scattering (Curve 2 for $\phi_0 = 10°$ and Curve 3 for $\phi_0 = 60°$)

$$k = \frac{\ln \sec \phi_0}{E_1(-\mu_0 x \sec \phi_0) - E_1(-\mu_0 x)};$$

c) for point source with consideration of multiple scattering (Curve 4)

$$k = e^{\mu_0 x}/B.$$

For a disc subtended by the angle φ, taking multiple scattering into consideration (Curve 5 for $\phi_0 = 10°$, and Curve 6 for $\phi_0 = 60°$) the Formula (5) was used.

Comparison of corresponding curves (1 with 3 and 4 with 6) for $\phi = 60°$, shows that the effect of the extent of a plane source is exhibited by the rise in the attenuation factor to four times the value of the attenuation factor for a point source, at concrete thickness of x = 20cm, and its further uninterrupted rise. In the same manner it is seen that with $\phi_0 = 10°$ the attenuation of γ-rays from a disc follows the law of γ-ray attenuation for a point source for any shield thickness. In addition, a comparison of Curves 1 and 4, and Curves 3 and 6 shows that the effect of multiple scattering on the attenuation factor in the case of a disc corresponding to an angle of $\phi_0 = 60°$, because of the slant rays, is 10 to 15% higher than for a point source, and coincides with the point source at $\phi_0 = 10°$.

In this manner, the curves of Figure 5 clearly affirm that the extent of a plane source affects the attenuation factor for γ-rays in two opposite ways: the presence of slant rays in itself increases the attenuation factor as compared to a point source, and the multiple scattering of slant rays lessens the attenuation factor considerably more strongly than in the case of a point source.

The results shown above may be used for the evaluation of the effect of geometric extent of a source on the attenuation of γ-rays with consideration of multiple scattering in the shielding, and in some cases (for emitters having disc geometry), for the introduction of the proper corrections in practical calculations of shielding for γ-radiation.

The authors thank G.M. Domidenko and C.F. Ryzhenko for aid in making the calculations.

LITERATURE CITED

[1] G.V. Gorshkov, "Gamma Radiation from Radioactive Objects" (Publishing House LGU, 1956).

[2] N.G. Gusev, Handbook of Radioactive Emissions and Shielding (Medical Govt. Publishing House, 1956).

[3] L. Spencer, Phys. Rev. 88, 793 (1952).

[4] U. Fano, J. Res. Nat. Bur. Standards 51, 95 (1953).

[5] H. Goldstein and J.E. Wilkins, Calculation of the Penetration of Gamma Rays, USAEC (NYO-3075), 1954.

[6] J. Taylor, Application of γ-Ray Build-Up Data to Shield Design, WARD, RM-217 (1954).

Received December 4, 1956

NEW DESIGNS FOR EXTRACTION COLUMNS WITH INJECTION

C.M. Karpacheva, L.P. Khorkhorina and S.F. Medvedev*

The development of extraction technology, the separation and extraction of substances from solution, has created the task for designers of producing high output extraction apparatus.

A detailed survey of existing foreign apparatus was presented in a series of articles by Pratt [1] and Treibl [2, 3].

Injection and packed extraction columns are attractive by their simplicity and low cost of operation, but in many cases the extraction effectiveness in such columns is not satisfactory, and the height of the column necessary for the process is often considerable thus incurring increased capital costs. Because of this, it is, in many cases, necessary to make a choice of design in favor of mechanical separators.

In shell type, injection extraction columns, the mass transfer surface is formed as a result of the dispersion of one of the liquids.

In glass columns it is possible to observe how, in the region of the injector, small drops (fog) are formed, and how, as they rise, they combine and grow larger, thus sharply reducing the mass transfer surface and, consequently, the effectiveness of the process.

The process of extraction in injection columns was studied by many investigators [4-15], who showed that these columns work very effectively within a small region, 200-300 mm high, of the injector, that is, at the moment of dispersion of the liquid. Above this region the performance of the column becomes less effective.

In the injection columns already built [1] it was not possible to obtain more than two perfect plates, at a height of 15 m.

It should be mentioned that the effectiveness of the column along its height is strongly dependent on the viscosity and surface tension of the dispersed liquid. For viscous liquids the coalescence is slowed down; therefore injection columns can have relatively high effectiveness at heights of even several meters.

The creation of an extractor in which not only the high effectiveness near the injector at the time of dispersion could be used, but one in which the effectiveness is maintained at greater heights (or lengths) of the extractor, is a very interesting problem. The solution to the problem was found with the aid of a column with cross flow of liquids; this column we called a stage extraction column. Another solution of the problem is found in a column with several injectors and "reversal" of phases.

A. Stage Column

Extraction columns usually work on the principle of counter flow [1, 2]: the heavy liquid enters the column at the top and leaves at the bottom, the light liquid rises to the top. In some mechanical extractors of the mixing-settling type, cross flow is used, that is, the aqueous solution consecutively passes through several mixers and in each one comes in contact with fresh batches of solvent. A comparable principle was used in the stage column we developed, the schematic of which is shown in Figure 1. The original solution passes consecutively through all the stages (elements) of the column, each one of them receiving fresh extracting agent from

*In testing of the columns the following were participants: Engineers K.A. Dyanina, E.P. Rodionov and L.M. Maltsev.

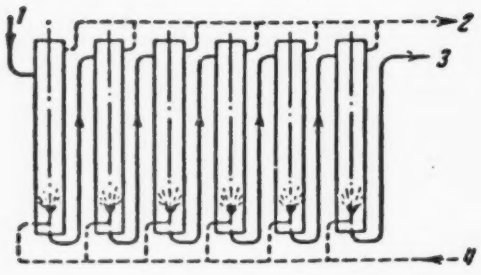

Fig. 1. Six stage column: 1) intake of aqueous solution; 2) outlet for organic solution; 3) outlet for aqueous solution; 4) intake of organic solution.

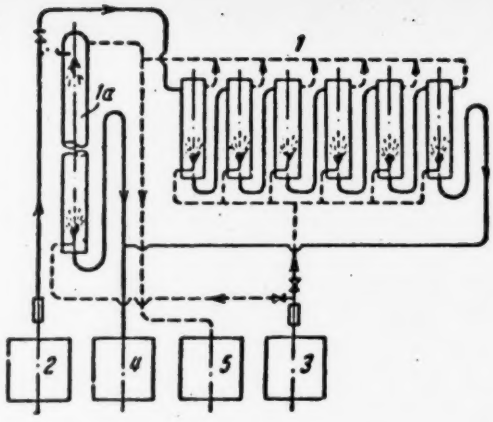

Fig. 2. Scheme for testing the columns: 1) six stage column; 1a) two injector column; 2, 3) feed tanks; 4, 5) storage volumes-containers.

one common collector through the injectors. Having passed one stage, the solvent is gathered in another collector. If we designate V_{org} as the volume of solvent passing to the extractor, and N as the number of stages in the column, then each stage will receive V_{org}/N solvent. Each element or stage of the column is approximately equal to a perfect plate.

Experiments were carried out according to the scheme shown in Figure 2. Initial aqueous solution of uranyl nitrate or acetic acid entered column 1 from feed tank 2. The extracting agent was introduced into the bottom of the column from feed tank 3. A gauge pressure up to 0.8 atmospheres was maintained constantly in the feed tanks. The aqueous solution emerging at the end of the process was collected in container 4; the extracting agent, saturated with acetic acid or uranium, in container 5. In testing the stage column, regulation of the intake flow of aqueous solution was done by valves at the entrance to the first stage or at the exit from the last stage. The regulation of extracting agent intake is more complicated since, besides the required constant, sum quantity of flow, the intake of each stage must be maintained constant within the limits of ± 10%.

The effectiveness of the column's operation was checked by sampling initial and final solutions after steady state operation had been established. Samples were collected every 15-20 minutes.

Tests were conducted of glass and metal columns of 23 mm diameter, composed of 1, 2 and 6 elements (see Figure 1). The overall height of each stage was 200 mm, and its working section was 150 mm high. The extraction was effected by diethyl esters from aqueous solutions of acetic acid or uranium. Initial acid concentration was 2 mole/liter. The aqueous solution from which the uranium was extracted was composed as follows: NH_4NO_3 – 7.5 mole/liter, $UO_2(NO_3)_2$ – 1.0 mole/liter, HNO_3 – 0.2 mole/liter.

The over-all ratio of currents $n = V_{org}/V_{aq}$ for the six stage column was taken as equal to 3; each stage received one sixth of the ester current, equal to V_{org}/N, and consequently, the ratio of currents for one stage (element) was $n_1 = V_{org}/V_{aq} = 0.5$.

The same ratio of currents, $n_1 = 0.5$ was used in testing the two stage column and the single-column element. The total volume of solutions through both phases was 9-10 m^3/m^2 hr.

It was confirmed that each stage of the single, two and six stage columns is equal to the theoretical, that is, equal to or less than 150 mm. In this manner the design of the new injection column appeared to be quite effective.

The basic merit of the newly developed stage column consists of its small over-all size and its simplicity of construction.

A disadvantage, particularly noticeable when running the column at low rates, is the plugging-up of the

injectors which forces stopping of the column. With the aid of filters, the plugging of the injectors can be eliminated.

As was pointed out earlier, the column was tested on light solvents with low viscosities and surface tensions. Its adaptation to viscous solvents like kerosene or tributylphosphate (TBP) will require some changes. Experiments on injection columns (see below) have shown that working with TBP thinned with ether or kerosene, the size of drops when rising grew slowly, therefore at a height of 3-4 m it is possible to obtain not one but 2-3 perfect plates (see table). In this case for a column with 5-6 plates two elements will be enough provided they are very high.

B. Column with Several Injectors and Phase Reversal

Another version of column with high effectiveness is the double injector type and four injection columns, shown in Figures 3 and 4. The distinguishing feature of these columns is the presence of two continuous and two dispersed phases. Below, where the continuous phase is aqueous, the extracting agent is fed through an injector, and at the upper part of the column, the solution is dispersed through an injector, the solvent acting as the continuous phase. There is no information on the use of such columns in industry. Treibl [3] describes similar columns as patented designs, but does not indicate that they are actually in use anywhere.

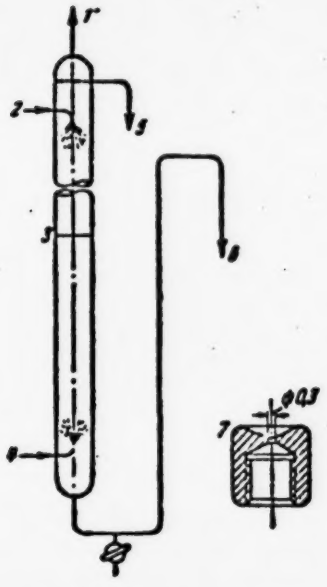

Fig. 3. Two injector column: 1) vent; 2) solution intake; 3) phase separation line; 4) solvent intake; 5) organic solution removal; 6) aqueous solution removal; 7) injector nozzle.

Fig. 4. Four injector column.

Recently published material [16] on an injection column with two injectors is so sketchy that it is not possible to put together a clear picture of the operation of this column and to compare it with another.

We tested columns 3 and 6 m high, 25 mm in diameter, with two injectors.

The diameter of the injector nozzle was 0.3 mm (Figure 3).

Tests of the columns were made with the following systems:

1. Water-acetic acid – mixture of tributylphosphate with a saturated hydrocarbon* or ester fraction. The acetic acid content in water solution was 2 mole/liter.

*$\overline{t_{boil}}$ = 170-270°C.

Test No.	Tested system	Process	Column height, m	Rate m^3/m^2 hr	% Extraction	No. perfect plates	EPPH* m
1	Water-acetic acid – 30% mixture TBP + 70% ester	Extraction	6	7	99.7	6	1
2			3	7	99.2	5	0.6
3	Water-uranylnitrate – 40% TBP + 60% kerosene	Extraction	3	6.5	96.8	1.9	1.6
4			3	6.5	96.8	1.9	1.6
5			3	6.5	98.7	2	1.5
6	Water-uranylnitrate – 30% TBP + 70% ester	Extraction	3	6.5	99.2	2.7	1.1
7			3	6.5	99.97	3	1
8	Water-uranylnitrate – 40% TBP + 60% kerosene	Re-extraction	6	6	97.3	6	1
9			6	12	97.3	4.5	1.3
10			6	12	99.6	6	1

*Equivalent perfect plate height.

2. Water-uranylnitrate-nitric acid -- mixture of TBP with the same thinners. The concentration of $UO_2(NO_3)_2$ in the initial aqueous solution was equal to 1.3 mole/liter; HNO_3 – 2 mole/liter.

The tests were conducted with the same scheme (Figure 2). The solutions were fed into a two injector column 1a. When extraction of uranylnitrate or CH_3COOH from the mixture into the water was performed, feed tank 2 was filled with distilled water or weak HNO_3 (~ 0.05N).

From the table it is seen that when extracting acetic acid in three and six meter double injector columns we succeeded in obtaining 5 and 6 plates respectively. When extracting uranylnitrate in a three meter column, the number of plates was 2-3 (with various compositions of extracting agent) and in test No. 7 practically total extraction was achieved. On the six meter column the number of perfect plates in the re-extraction process for uranylnitrate was 5-6. In this manner, by installing an additional injector and using phase reversal, we were able to reach effective operation of the injection column at heights equaling 6 plates; the minimum height of a perfect plate in this case was 0.6-1 m.

For comparison, using the same systems and rates, we tested packed columns of the same diameter and height. It was established that they have about the same EPPH as the two injector columns.

Two, three and four injector columns can be used in processes where the organic phase after extraction is additionally washed with clean water or some solution, or the aqueous phase is subjected to additional controlling extraction with fresh extracting agent.

In this case (i.e., the basic column having two injectors) an additional injector is placed at the top for washing through of the extracting agent, and an additional injector is placed at the bottom for complementary extraction (Figure 4). This allows increasing the height of the column another 2-3 plates at the lower and upper ends.

LITERATURE CITED

[1] H.R.C. Pratt, Ind. Chem. 30, No. 356, 357, 359 (1954); 31, 361, 369, 370 (1955).

[2] R.E. Treybal, Liquid Extraction (McGraw Hill, New York 1951).

[3] R.E. Treybal, Mass Transfer Operations (McGraw Hill, New York 1955).

[4] R.M. Kreager and C.J. Geankoplis, Ind. Eng. Chem. 45, 2156 (1953).

[5] W.Jr. Licht and J.B. Conway, Ind. Eng. Chem. 42, 1151 (1950).

[6] T.K. Sherwood, J.E.Evans and J. Longcor, Ind. Eng. Chem. 31, 1144 (1939).

[7] F.B. West and A.C. Robinson, Ind. Eng. Chem. 43, 234 (1951).

[8] M.L. Newman, Ind. Eng. Chem. 44, 2457 (1952).

[9] F.E. Gier and J.O. Hougen, Ind. Eng. Chem. 45, 1362 (1953).

[10] C.J. Geankoplis and A.W. Hukson, Ind. Eng. Chem. 42, 1141 (1950).

[11] C.J. Geankoplis, P.L. Wells and E.L. Hawk, Ind.Eng. Chem. 43, 1848 (1951).

[12] F.H. Blanding and J.C. Elgin, Trans. Am. Inst. Chem. Engrs. 38, 305 (1942).

[13] J.M. Coulson and S.J. Skinner, J. Chem. Eng. Sci. 1, 197 (1952).

[14] H.F. Johnson and H. Bliss, Trans. Am. Inst. Chem. Engrs. 42, 331 (1946).

[15] G.M. Minard and A.I. Johnson, Chem. Eng. Progr. 48, 62 (1952).

[16] N.I. Galperin et al., Chemical Science and Industry 5 (1956).

Received August 1, 1956

BLANK
PAGE

SCIENCE CHRONICLE

ALL-UNION CONFERENCE ON RADIOCHEMISTRY

Radiochemical research has assumed large proportions in the Soviet Union. In order to provide an opportunity for the discussion of the main problems of radiochemistry and the directions in which this science is developing, an All-Union Conference was called for March 1957 in Leningrad. About six hundred scientific workers from various cities of our country took part in this conference. In the fifty papers presented at the conference, the main problems of theoretical radiochemistry and the chemistry of certain radioactive elements were considered. The topics included the forms in which small amounts of radioactive substances exist in solutions and solids, their behavior when coprecipitated with carriers, the laws of distribution between two immiscible phases, the chemistry of technetium, promethium, and the transplutonic elements (americium, curium, berkelium, californium, etc.).

The investigation of the state of radio elements in dilute solution and their behavior when coprecipitated with crystalline precipitates constitute the central problem of radiochemistry, on which Soviet scientists have been working since 1924 (V.G. Khlopin's school). The experimental material presented showed that work on this problem has developed successfully and has resulted in the necessity of re-examining some of the earlier views. As a result of numerous experimental investigations, I.E. Starik and co-workers established the existence of true colloids in the case of substances present in solution at high dilution. This result confirms the view, which was for a long time rejected, that radioactive substances found in nature in extremely low amount form true colloidal solutions when the solubility product has been attained. It was shown, moreover, that by a combination of various methods of investigating colloidal solutions it is possible to determine unequivocally the proportion of a substance present in solution, both in the ionized state, and also as true colloids or pseudocolloids.

Several investigators presented interesting data on the leaching of daughter radioactive substances from minerals and artificial salts, and hypotheses were advanced concerning the form in which radio-elements are present in solids (I.E. Starik and co-workers, V.I. Baranov, K.V. Zaborenko and co-workers).

New theoretical and experimental results were obtained on the coprecipitation of radio elements with crystalline precipitates. Several examples were given to show that anomalous mixed crystals are subject to laws that were previously considered to be valid only for true mixed crystals (V.I. Grebenshchikova, E.M. Ioffe). It follows that the method, used both here and abroad, of isomorphous coprecipitation for the determination of valency in substances present in solution in extremely small amounts may sometimes lead to incorrect conclusions. V.N. Bobrova pointed out that the mechanism of entrainment depends not only on experimental conditions, as was considered previously, but also on the properties of the macrocomponent.

Values of crystallization coefficients obtained by the classical methods of V.G. Khlopin have been utilized in many systems for the improvement of the technology of preparing pure reagents (G.I. Gorshtein).

From the paper of N.A. Rudnev and A.A. Bragina on the coprecipitation of thallium and gallium with sulfides it may be inferred that the mechanism of entrainment is very complex and depends on the nature of the adsorbent and the character of the aging of the precipitates.

A.A. Grinberg, in a paper on the importance of complex compounds for radiochemistry, examined the significance of complex-formation for the detailed description of the state of radio-element ions in solution. The part played by complex formation in processes of cocrystallization of radio elements with crystalline precipitates in their isolation from solutions and melts was noted for the first time (V.I. Grebenshchikova and E.M. Ioffe for solutions; V.R. Klokman for melts).

A.A. Grinberg pointed out that a critical analysis of data obtained in the study of anomalous mixed crystals suggests that the presence of complex ions in solution may sometimes provide the explanation of the absence of a lower limit of miscibility. R.V. Bryzgalova pointed out that by determining crystallization coefficients one may establish the minimum concentration of complex former at which complex ions begin to be formed from substances present in solution in amounts detectable by an impulse counter.

The conference discussed several problems concerned with the application of adsorption processes in chemical practice. In the papers and discussions on this topic the results of experimental and theoretical investigations on the following questions were presented:

1. Theory of ion exchange (paper by B.P. Nikolsky).

2. Chromatographic separation of rare earth and transuranic elements (papers by N.N. Tunitsky, B.K. Preobrazhensky, M.M. Senyavin, V.B. Dedov, A.K. Lavrukhina and co-workers, and others).

3. Determination of the state of radio elements in solution by the method of adsorption on glass and on ion-exchange resins (papers by A.V. Kositsyn, V.I. Paramonova and co-workers, Yu.B. Gerlit, A.N. Subbotina, and others).

4. Selective adsorption of some radio elements on ion-exchange resins, silica gel, and other porous adsorbents (B.P. Nikolsky and co-workers, D.N. Surazhesko).

In the papers on the chromatography of rare-earth elements, the main attention was devoted to the theoretical and experimental basis for the rapid separation of the rare-earth products of nuclear reactions. The results reported at the conference indicate that it is possible to separate two rare-earth elements completely in the space of five minutes (B.K. Preobrazhensky). A theoretical equation was proposed (N.N. Tunitsky) for determining the minimum time required for the separation of two rare-earth elements.

V.M. Vdovenko read a review paper entitled "Extraction Processes in the Study and Separation of Radio-Elements." Extraction is used extensively in radiochemical investigations, so that the study of processes of extracting the elements has acquired special importance. Contributions on the theoretical and experimental investigation of extraction processes were made by the following: A.V. Nikolaev – obtaining weighable amounts of cerium by extraction of Ce^{4+} with tributyl phosphate; I.A. Reformatsky and M.N. Ryzhov – extraction of americium and curium with tributyl phosphate; and also A.M. Rozen.

V.M. Vdovenko, L.N. Lazarev, A.A. Lipovsky and M.G. Kuzina reported the preparation of aniline uranyl triacetate, in the form of which uranium can be extracted with certain organic solvents. Taking the example of the distribution of uranyl nitrate between aqueous nitric acid and dibutyl ether, they showed that the formation of complex compounds has a very important effect on the extraction of radio elements.

In the examination of the chemical properties of individual radio elements, the greatest interest and the most lively discussions were aroused by the papers on the chemistry of technetium and americium. V.I. Spitsyn and A.F. Kuzina detailed the procedure for obtaining weighable amounts of technetium. Yu.B. Gerlit described the behavior of technetium ions in various valency states in acid, neutral and alkaline media.

In a review of the chemistry of americium, G.N. Yakovlev discussed methods of obtaining appreciable, weighable amounts of Am^{241} and Am^{243} and the future prospects in this field. He characterized the valency states of the element, and described methods of separating americium from transplutonic and rare-earth elements. He mentioned that americium has been studied more thoroughly than some long-known elements.

A.G. Rykov and A.A. Zaitsev reported their recent results on the reduction of Am^{V} and Am^{VI} by the radiolysis products of water subjected to the α-radiation of Am^{241}. As a result of an investigation of the kinetics of these reactions, it was shown that there is a relationship between the radiational yield of the reducing radiolysis products from water and the concentration of sulfate ions. A substantial difference was noted between the rates of reduction reactions of Am^{V} and Am^{VI}.

Interesting results on the chromatographic separation of berkelium and californium were reported by K.V. Filippova and L.I. Guseva. They obtained the best separation when they used ammonium hydroxyisobutyrate as eluent.

The conference passed a resolution on the directions of further investigation in radiochemistry, and the

question of the publication of a special journal "Radiochemistry" was raised. Part of the proceedings of the conference will be published in Inorganic Chemistry.

V.I. Grebenshchikova and A.M. Trofimov

THE USE OF RADIOACTIVE ISOTOPES IN BIOCHEMISTRY

(From the 2nd Conference on the Biochemistry of the Nervous System)

The second Conference on the Biochemistry of the Nervous System, convened by the Institute of Biochemistry, Academy of Sciences of the Ukrainian SSR, was held in Kiev from February 12 to 16 of this year.

Thirty-five papers were presented and discussed; these dealt with various aspects of the course of chemical processes in the brain and the relationship of these processes to the activity of the nervous system. The use of radioactive isotopes has deepened and broadened our knowledge in this field. More than half of the papers dealt with new data obtained with the aid of radioactive tracers.

Chemical processes in the brain have been studied with the aid of the radioisotopes P^{32}, S^{35} and C^{14}, in the form of inorganic phosphate (P^{32}), methionine and thiamine (S^{35}), acetic acid, glucose, glycine and tyrosine (C^{14}).

Great interest was aroused by the paper of Academician A.V. Palladin and his associates on "Investigations of the Proteins of the Nervous System" which contained new data on the protein composition of the brain and nerves. A.V. Palladin used the method of paper electrophoresis to demonstrate the presence of several protein substances in brain matter; the amounts and properties of these substances were found to differ in different regions of the nervous system. By introduction of methionine tagged with S^{35} into the animal organism it was shown that the different protein fractions differ considerably in their rates of renewal. It is probable that proteins differing in renewability differ in their significance in the activity of the central nervous system.

The paper by G.A. Nechaeva, N.V. Sadikov and V.A. Skvortsov on "Renewal of the Amino Acid Composition of the Proteins in the Brain in Different Functional States" described the use both of methionine and of glucine tagged with C^{14}. Variations of the incorporation of S^{35} and C^{14} into proteins, glutathione, glutamine and glutamic acid were found, indicating that the metabolic rate of these substances in the brain depend on its functional state. Renewability increases on stimulation and decreases in narcotic sleep.

K.I. Pogodaev and A.I. Mekhedova detected some intensification of the renewal rate of brain proteins 1-2 days after sleep lasting three days, induced by sodium amytal; this may be attributed to intensified resynthesis of the proteins.

B.I. Ibaikina and E.E. Goncharova devoted their paper to the little-studied question of the structure and physiological role of brain glycogen. It was found that only 20% of the glycogen in the brain is in a free state, most of it being bound with proteins and lipoids. Acetic acid and glucose containing C^{14} were used to show that C^{14} is included at different rates into different glycogen fractions. Free glycogen is renewed at the greatest rate, and the renewal rate increases still further in an animal stimulated by phenamine. The renewability of the glycogen bound with proteins and lipoids, however, remains unchanged. All this indicates a difference in the physiological role of free and bound glycogen in the brain; free glycogen is apparently used in brain metabolism as a source of energy.

M.I. Prokhorova and Z.N. Tupikova used the same radioactive tracers to demonstrate an increase of the specific activity of brain glycogen and a decrease of the amount of it present in a state of stimulation induced by phenamine. In narcotic sleep the amount of glycogen in the brain increases while its specific activity falls below the normal level. The changes in the amounts and specific activity of glucose in the brain are opposite to the corresponding changes in glycogen. The authors concluded that accumulation of carbohydrates in the brain during narcotic sleep is the result of a decreased rate of carbohydrate metabolism. From determinations

of the radioactivity of carbon dioxide expired by an animal (dog) it was found that under normal conditions the animal begins to utilize radioactive glucose 30-40 minutes after it has entered the organism, and the utilization reaches a maximum after 60 minutes. In an experimentally stimulated state utilization of glucose began considerably sooner, after 10-15 minutes, while it was retarded in narcotic sleep.

G.E. Vladimirov, T.N. Ivanova and N.I. Pravdina isolated from brain substance a new fraction of organic phosphorus compounds, which were formerly regarded as "impurities" in ribonucleic acid, determined by the widely used method of Schmidt and Tanhauser. These substances proved to be lipoproteins, and the most remarkable feature was the extremely high exchange rate of their constituent phosphorus. The great physiological significance of these lipoproteins is emphasized by the changes in their metabolic rates in relation to the functional state of the brain.

E.B. Skvirskaya and T.P. Silich made a comparative study of the phosphorus-containing substances in the nervous system by means of P^{32}, paper chromatography, and chemical analysis. The most important result of these investigations was that differences were found not only in the quantitative contents of the phosphorus compounds in various parts of the nervous system and in different structural portions of the nerve cells, but also in the metabolic rates of the same phosphorus compounds, depending on the morphological structures with which they are associated.

A.A. Smirnov and E.V. Chrikovskaya reported the results of an investigation important from the methodological aspect. Of the two commonest methods for isolation of the brain lipoids, the method of extraction by boiling solvents after preliminary treatment of the brain with trichloroacetic acid leads to loss of part of the lipoids, especially those with high specific phosphorus activity. It appears that this treatment causes destruction of acetalphosphatides. If brain tissue is extracted with organic solvents in the cold, without treatment with trichloroacetic acid, acetalphosphatides are preserved.

P.A. Kometiani and his associates synthesized phosphorylcholine and phosphorylethanolamine tagged with P^{32}. By comparing the rate of inclusion of P^{32} from these compounds into the brain phospholipids with the rate of inclusion of tagged inorganic phosphate, they showed that these phosphorus esters are involved in the synthesis of the corresponding phospholipids.

Very interesting data were presented by N.A. Verzhbinskaya in the paper on "Oxidative Phosphorylation in the Brains of Vertebrates in Vivo and Formation of a Barrier to Phosphorus in a Number of Vertebrates." N.A. Verzhbinskaya used P^{32} to study the rate of increase of the specific activity both of inorganic phosphate and of phosphorus in adenosine triphosphate (ATP) in the animal brain. On the basis of these experiments N.A. Verzhbinskaya was able to calculate the "conversion time" and "conversion rate" of macroergically bound ATP phosphorus in the brain of an intact animal. It was found that the conversion time (i.e., the time in which all the bound ATP phosphorus present in the brain is decomposed and resynthesized) is: for fishes, 75-90 minutes; for amphibians, 48 minutes; for reptiles, 14 minutes; and for mammals, only 8, 10 or 12 minutes. Such results could only be obtained with the use of radioactive tracers.

One of the sessions of the Conference was devoted to the topical question of brain metabolism in hypothermia, used in surgery in operations on the heart and lungs. The paper by G.E. Vladimirov and his associates on "The Influence of Hypothermia, in Conjunction with Arrested Circulation, on Metabolism in the Brain" gave the results of studies of carbohydrate, protein and phosphorus metabolism in the brain during hypothermia. Hypothermia results in a considerable decrease of phosphorus renewal in the organic phosphorus compounds. The renewal of substances which are significant from the energy aspect is inhibited to a smaller extent than the renewal of substances contained in tissue structures, such as lipoids, proteins and ribonucleic acid. G.I. Vladimirov emphasized that the use of glycine and tyrosine tagged with C^{14}, and of methionine tagged with S^{35}, showed a particularly sharp retardation of the renewal of the amino acids in the brain proteins in hypothermia.

R.V. Chagovets, E.V. Lakina, A.A. Rybina, R.S. Fidman and Ts.M. Shtutman made a comparative study of the effects of physical cooling, aminazine, sodium evipan, and the combined action of cooling and aminazine, on metabolic processes in nerve tissues. This extensive paper contains noteworthy data on the incorporation of thiamine (vitamin B_1) tagged with S^{35} in various organs and tissues of the organism. Prolonged cooling decreases the incorporation of thiamine in all the organs and tissues studied, with the exception of the brain and heart, in which the incorporation of thiamine increases under these conditions.

Three papers dealt with the effects of ionizing radiation on the chemical processes in the brain. The

paper by G.Ya. Gordiskaya and O.N. Barmina contained data on the action of internal β-irradiation on phosphorus and protein metabolism in the brain. In these investigations P^{32} was used simultaneously as a source of β-radiation and as a tracer for studying the rate of phosphorus metabolism. In some experiments methionine tagged with S^{35} was introduced together with P^{32}. It was found that the renewal rates of the organic phosphorus compounds and of the amino acids in the proteins varied with the dose of the β-radiation source present in the animal organism.

L.S. Cherkasova and her associates presented data on the effects of total exposure of animals to x-rays on some characteristics of brain metabolism. It was found that the renewal rate of energy-rich phosphorus compounds: adenosine triphosphate and creatine phosphate, decreases in these conditions.

P.F. Minaev presented data on changes in brain metabolism under the local action of x-rays. He advanced the very interesting view that the nervous system, and particularly the brain cortex, have not only high sensitivity but also high resistance to ionizing radiations.

A.A. Leontyeva's paper dealt with the effects of trauma on phosphorus metabolism. Operative trauma of the brain produced changes in the renewability of phosphorus compounds both in the traumatized and in the opposite hemisphere. In the traumatized hemisphere the relative specific activity of these substances remained different even 9 months and 1 year after the traumatization.

The proceedings of the Conference will be published by the Academy of Sciences, Ukrainian SSR as a separate volume.

G.Ya. Gorodisskaya

WITHIN THE SOVIET UNION

THE ATOMIC PAVILION OF THE ALL-UNION INDUSTRIAL EXHIBITION

(Section of Agriculture and Biology)

In the section "Agriculture and Biology" are shown the results of research on the biological effects of radiations on animal and plant organisms, and information is also provided on the use of the tracer atom technique in soil science, agrochemistry, and plant and animal physiology and biochemistry.

By means of the tracer atom technique it proved possible to determine for the first time how much phosphorus a plant assimilates from the soil and how much from fertilizers; i.e., to determine the conditions in which added fertilizers increase the utilization of the elements of natural soil fertility by the plant (Figure 1).

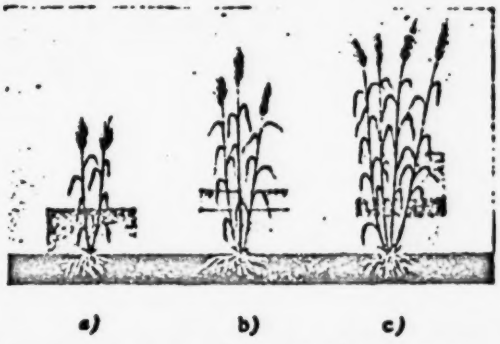

Fig. 1. Assimilation of phosphorus by plants: a) from the soil; b) from granulated fertilizers introduced with the seeds; c) from fertilizers introduced under the plow and into the rows.

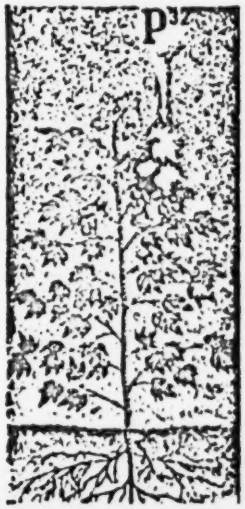

Fig. 2. Phosphorus distribution in foliar nutrition.

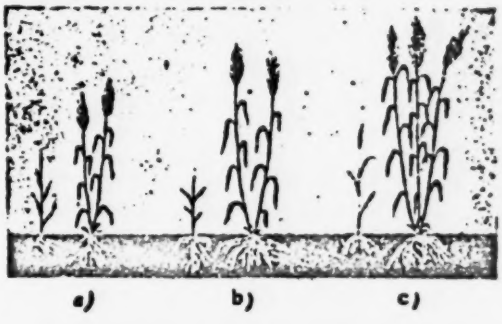

Fig. 3. Methods of supplying fertilizers to cereal crops: a) in rows; b) under the plow; c) in rows and under the plow.

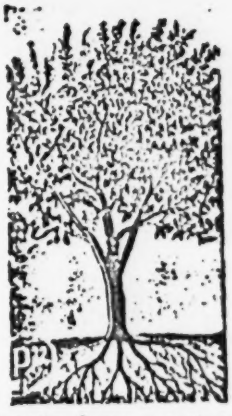

Fig. 4. Connection between roots and crown of a fruit tree.

This method also made possible a deeper study of foliar mineral nutrition in plants (Figure 2). Foliar

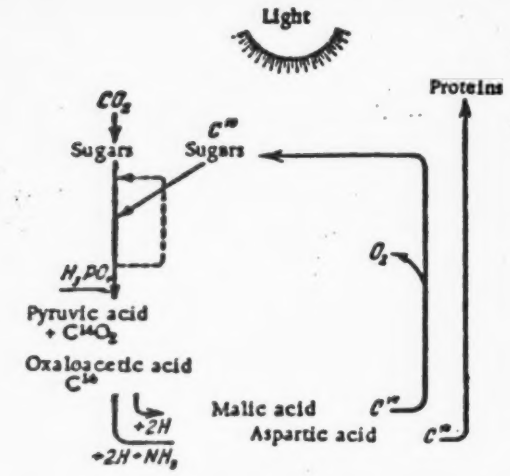

Fig. 5. Possible nutrition of plants by carbon dioxide through the root system (transfer of CO_2 through the roots to the leaves).

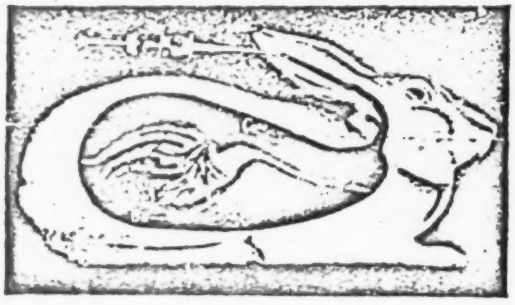

Fig. 6. Biosynthesis of vitamin B_{12}.

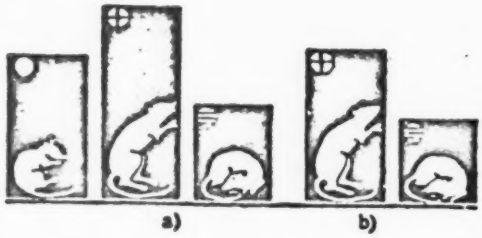

Fig. 7. Metabolic rates in the brain: a) inclusion of P^{32} into phospholipids; b) inclusion of S^{35} into sulfatides.

feeding of the cotton plant, sugar beet, and some other crops is used as an auxiliary method for regulating nutrition and metabolism in plants.

The question of the right times for introducing fertilizers has been further elucidated in experiments with the use of the isotope technique. Figure 3 shows the results of experiments with P^{32}, which indicate that a combination of the main addition of fertilizer before sowing with fertilizer added along the rows during sowing creates the best conditions for utilization of the nutrient substances both from the fertilizer and from the soil during all development stages of the plant.

Wide potentialities are also provided by tagged atoms for studies of the nature of the most important biochemical processes forming the basis of agriculture production. Photosynthesis is one such process. Experiments with C^{14} did not confirm earlier views concerning the primary products of photosynthesis. It has been shown that among the primary products are glyceric and phosphoglyceric acids; not only carbohydrates but proteins also can be the direct products of photosynthesis in plant leaves.

Radioactive isotopes such as P^{32}, C^{14}, etc., are successfully used for studying rates of translocation and metabolism in plants. On one of the stands it is shown how P^{32} is used to study the interconnection between the roots and tops of fruit trees (Figure 4). It has been shown with the aid of radioactive C^{14} that the translocation rate of assimilated substances is greatly diminished with decrease of temperature and in conditions of water deficiency (drought). In different climatic conditions, the assimilated products go to different parts of the same plant. For example, in the central belt of the USSR, the photosynthesis products formed in the leaves of the potato plant go mainly to the tubers, while in the Far North, in conditions of a long day and low soil temperature, they tend toward the stems and growing points; this leads to a low starch content in the potatoes and to a low yield.

Figure 5 shows the results of experiments with C^{14}, in which a totally new function of the root system was discovered – assimilation of carbon dioxide from the soil and its transfer to the leaves and other green parts of the plant.

The exhibition contains demonstrations of the use of radioactive isotopes (Co^{60}, S^{35}, P^{32} and C^{14}) for studying metabolism in the animal organism. Only a few individual examples of such investigations are shown on the stands. Figure 6 illustrates the synthesis of vitamin B_{12}.

It has been shown by means of Co^{60} that the vitamin is synthesized in the organism only by the intestinal microflora. By the use of S^{35} and P^{32} isotopes (Figure 7) it has been possible to determine how the renewal rates of proteins and the lipoid phosphorus fraction in the brain depend on the functional state of the organism. It was shown that renewal of proteins and of the lipoid phosphorus fraction is accelerated when the organism is stimulated, and suppressed during narcotic sleep.

By the use of radioactive tracers for studying the energy relationships of cell activity it has been shown that energy transfer in the cancerous cell is quite different from that in a normal cell. It has been shown with the use of tagged glucose that in the cancerous cell, where intensive respiration is accompanied by intensive glycolysis, the energy of both processes is always utilized in protein synthesis.

In 1957 considerable space will be devoted in the "Agriculture and Biology" section to work on the biological action of radiations on animal and plant organisms. For example, the stands will show the results of studies of the effects of ionizing radiations on fertility and heredity in mammals, work on the direct and indirect effects of radiation on the embryonic development of mice, and data on changes of spermatogenesis in monkeys as the result of sublethal x-ray irradiation.

Work on the sterilizing irradiation of potatoes and vegetables to prevent sprouting, and data on the disinfecting action of radiations which destroys pests on grain will also be shown.

Other exhibits will include models of equipment for irradiation of potatoes and sterilization of food products, of apparatus for studying photosynthesis and respiration under natural conditions, and useful portable equipment of great practical importance in agriculture.

The effects of ionizing radiations on plants, stimulating their growth and development, will also be demonstrated.

Considerable extensions will be made to the stand showing the use of isotopes for research on animal and bird breeding; the results of studies of calcium metabolism in hens with the use of Ca^{45}, investigations of the activity of the thyroid gland in animals with the use of I^{131}, and the use of S^{35} for studying the permeability of the skin of sheep to sulfur preparations, will be demonstrated.

The stand showing the use of radioisotopes for studying plant physiology will be completely renewed. The most interesting work on the biosynthesis of certain specific substances in plants will be shown. It has been shown by the use of C^{14} that the principal sites of catechin synthesis are young three-leaf shoots. The rate of catechin formation in adult and old leaves is 20-40 times less. Experiments with tagged compounds have demonstrated the exceptional role of the roots of the tobacco plant in nicotine synthesis.

R.A. Shirshova

STUDY OF THE DIFFUSION OF IRON IN OXIDES USING THE METHOD OF LABELED ATOMS

In the Surface Layer Structure Laboratory of the Institute of Physical Chemistry of the Academy of Sciences, USSR, Professor K.M. Gorbunova and V.I. Izvekov are making extensive use of radioactive isotopes in the study of the diffusion of metals in oxides.

The method of radioactive tracers has been used for investigating the diffusion of metals in oxides. It has proved to be much more convenient and reliable than the optical, microscopic, and other methods previously employed.

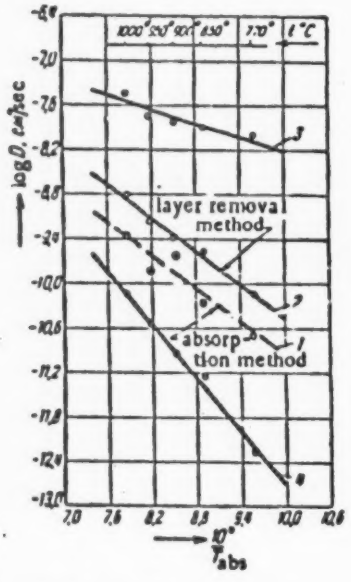

Determination of the activation energy of the diffusion of iron in TiO_2.

The rate of diffusion of cations in oxides is determined by the coefficient of diffusion $D = D_0 \cdot e^{-Q/RT}$, where D_0 is a pre-exponential factor, Q is the activation energy of diffusion and R and T are respectively the gas constant and the absolute temperature. In determining the coefficient of diffusion of iron, labeled with the radioactive tracer Fe^{59}, a β and γ radiator, in magnetite (Fe_3O_4), corundum (α-Al_2O_3) and rutile (TiO_2), the authors used two methods of investigation: absorption and the removal of layers.

In the absorption method, the diffusion constants can be calculated from the reduction in activity of the specimen, depending on the diffusion of iron in the oxide at the given temperature; this method of investigation is non-destructive. The second method is based on the determination of the variation of activity of the specimen in which the diffusion process has taken place, as a function of the depth of the layers removed. From the results of the measurements, curves were constructed showing the distribution of the diffused metal in the oxide specimen. The specimens were prepared by compressing powders of the oxides of aluminum, iron and titanium into tablet form (diameter 10 mm, thickness up to 5 mm) under a pressure of 200 atmos. The oxide tablets were then sintered for 50 hours at 1100-1400°C. The specimens thus obtained were homogenized for 25 hours under the conditions of the diffusion experiments.

The specimens were coated with a thin film of iron (thickness in tenths of a micron) containing Fe^{59} by vacuum sputtering [1].

Heating for diffusion was carried out in air or in a vacuum (10^{-3} mm Hg) for 5-358 hours at a temperature constant to an accuracy of ± 5°C. The temperature varied between 770 and 1200°C. The radioactive metal penetrated the specimen to a depth of from 200 to 500 microns.

For calculating the coefficients of diffusion by the absorption method, the equation proposed by Gruzin and Litvin [2] was used:

$$\frac{I_\beta I_{0\gamma}}{I_\gamma I_{0\beta}} = e^{\mu^2 Dt}(1 - \operatorname{erf} \mu \sqrt{Dt}), \qquad (1)$$

where $I_{0\beta}$ and $I_{0\gamma}$ are the initial β and γ activities of the specimen; I_β and I_γ, the β and γ activities of the specimen after the diffusion of iron during a period t; D, the coefficient of diffusion; μ, the coefficient of absorption, and $\operatorname{erf} \mu \sqrt{Dt}$ is the integral of error probability.

The coefficient of absorption μ was determined experimentally from the initial part of the absorption curve for β-radiation of Fe^{59} in aluminum and calculated according to the equation $N = N_0 \cdot e^{-\mu x}$, and for the oxides investigated, was found from the equation

$$\left(\frac{\mu}{\rho}\right)_{Al} = \left(\frac{\mu}{\rho}\right)_{Fe_3O_4} = \left(\frac{\mu}{\rho}\right)_{\alpha-Al_2O_3} = \left(\frac{\mu}{\rho}\right)_{TiO_2} \qquad (2)$$

The experimental data obtained by the method of layer removal were evaluated using the equation from Reference [3]:

$$N = \frac{N_0}{2\sqrt{\pi D t}} \cdot e^{-\frac{x^2}{4Dt}},$$

where N is the radioactivity of the iron after removal of a layer of thickness x; N_0 is the initial activity; t is the time of heating; D is the coefficient of diffusion.

The figure shows data relating to the calculation of the quantities Q and D_0 by the graphical method for the case of the diffusion of iron in TiO_2, during which the specimens were heated in a vacuum in the temperature range 770-1000°C. The straight line 1 was obtained by the absorption method, and the straight lines 2, 3 and 4 by the method of layer removal. Line 4 is based on the coefficients of diffusion calculated from the initial part of the curve for the distribution of activity in the specimen; Line 3 is based on results relating to deep layers.

It may be assumed that the high values of the diffusion coefficients and the lower value for the activation energy as determined from Curve 3 are due to the fact that these data were obtained for diffusion along the boundary grains. Averaging the results corresponding to the straight lines 3 and 4 gives values represented by the straight line 2, the slope of which is close to the slope of the straight line constructed on the basis of the data obtained by the absorption method.

The data corresponding to the diffusion of iron in α-Al_2O_3 and Fe_3O_4 were evaluated in a similar manner.

Further investigations on these lines and particularly the elucidation of the influence of impurities in the oxides on the rate of diffusion of the metal should assist in elucidating the mechanism of the action of alloying additions in increasing the oxidation resistance of alloys.

N.B. Mikheev

LITERATURE CITED

[1] V.L. Izvekov, Instruments and Technique of Experiment No. 2, 101, 1957.

[2] P.L. Gruzin and D.F. Litvin, Proc. Acad. Sci. USSR 94, 1, 41 (1954).

[3] W. Johnson, Trans. AIMEE 143, 107 (1941).

LOCATION OF THE AXIS OF A γ-RAY BEAM BY MEANS OF A SECTORED IONIZATION CHAMBER

In work with betatrons and synchrotrons, it is frequently necessary to locate quickly and accurately the axis of a beam of γ-rays. I.N. Usova (Laboratory for Accelerators and Photonuclear Reactions, Phys. Inst., Acad. Sci., USSR) has developed a very convenient method for locating the axis of such a beam; this method makes use of a so-called sectored ionization chamber.

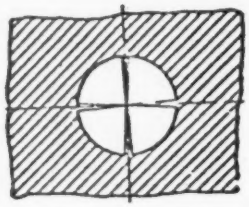

Fig. 1. Diagram showing the principle of operation of the sectored ionization chamber.

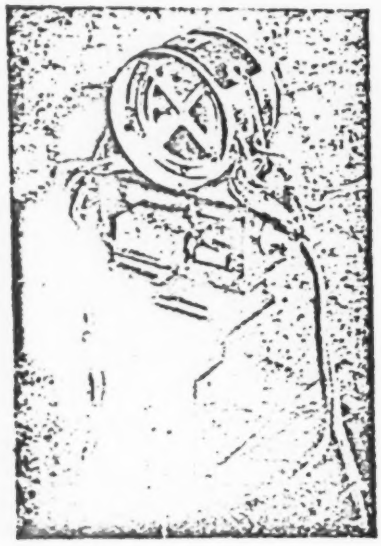

Fig. 2. Photograph of a sectored ionization chamber and the apparatus for positioning it in the beam. The electronic circuit is directly below the chamber. The front cover is removed.

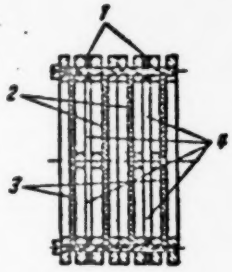

Fig. 3. Section of the sectored chamber; 1) guard rings; 2) collector electrodes; 3) high-voltage electrodes; 4) sectored working volumes.

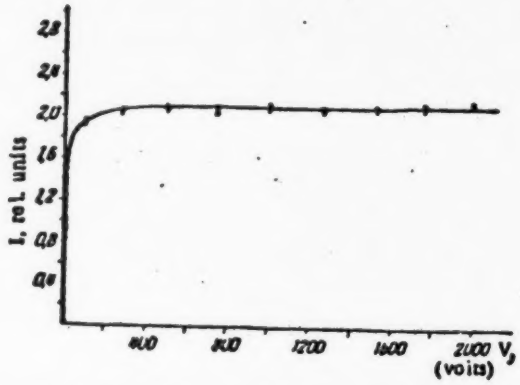

Fig. 4. Voltage-current characteristics of the sectored chamber.

The principle of operation of the chamber is illustrated in Figure 1. The four sectors cut from one solid block are the working volumes of four ionization chambers. The axially symmetric γ-ray beam from the accelerator is directed perpendicularly with re-

spect to the plane of the circle. The ionization currents from the four chambers are the same when the axis of the γ-ray beam coincides with the axis of the sectored chamber. The only requirement is that the dimensions of the chamber be comparable with the half-width of the intensity distribution of the beam. The axis of the beam is located by moving the chamber in the plane perpendicular to the beam axis and finding the point at which the currents from the working volumes are the same.

A general view of the setup used at the 265-Mev synchrotron of the Phys. Inst. Acad. Sci., USSR is shown in Figure 2. In the version used here the chamber is a cylinder 120 mm in diameter and 80 mm high. A double-layered air chamber of annular plexiglass rings and foil electrodes is mounted in a thin-walled aluminum case (Figure 3). Each layer contains two working volumes in the form of sectors cut out of the plexiglass slab. The cavities in one layer are displaced by an angle of 90° with respect to the cavities in the other layer. In each layer the two-sector working volumes have a common collector electrode and two separate high-voltage electrodes. Voltages of the same magnitude but opposite polarity are applied to the high-voltage electrodes. With this arrangement the differential ionization current of the two sectors is measured; this difference vanishes when the center of the chamber coincides with the axis of the beam.

Great care has been taken to ensure that the working volumes are identical and to eliminate spurious currents. All elements of the circuit connected with the collector electrode are covered with serazine and shielded from external electrostatic fields. Under operating conditions the spurious currents are less than $5 \cdot 10^{-15}$ amp, making it possible to measure differences up to 10^{-11} amp. The ionization current is determined from the charge which accumulates in a capacity. The collector electrode of each pair of sectors is connected to an unbalanced circuit (to an electrometer tube type 1E1P) located directly at the chamber. The high voltage is obtained from a standard power supply (VSE-2500). The operating point corresponds to a voltage of 1,000 volts (Figure 4).

The chamber can be positioned in the horizontal and vertical planes by means of two electric motors and a remote control system.

Special tests of the sectored chamber, carried out with a collimated source of γ-rays from a powerful Co^{60} source show that the working volumes are the same and that the chamber has good sensitivity.

Since the beginning of 1956 the sectored chamber has been used systematically at the 265 Mev synchrotron of the Phys. Inst. Acad. Sci. for locating the axis of the beam. The direction of the beam axis has been established with an accuracy better than 1'.

The sectored chamber can also be used for placing samples to be irradiated in the center of the beam. In this case the sample is rigidly attached to the chamber which is located at a distance in front of the sample being irradiated. The chamber does not have any significant effect on the transmission of the γ-ray beam since the amount of material in the working volume of the chamber is insignificant. It is also important that the reverse flux of γ-quanta and electrons scattered from the sample does not enter the chamber.

In operation with a sectored chamber (as with any thin-walled chamber) the background electrons in the γ-ray beam have an effect. There are different methods for reducing this effect but these involve either a considerable increase in the complexity of construction of the chamber or the use of thick walls. Hence it is important that there be nothing placed in the γ-ray beam between the chamber and the accelerator.

N.B. Delone

FOREIGN SCIENTIFIC AND TECHNICAL NEWS

DEVELOPMENT OF ATOMIC ENERGY IN ENGLAND

The rapidly decreasing coal resources in England, and the absence of petroleum resources, are forcing the leaders of English industry to look for new sources of energy; for this reason a great deal of attention is being devoted to the development of atomic energy in England.

The plans for construction of atomic electro-stations in England have over the past two years changed sharply toward intensification of the effort. The government program for development of atomic energy, that was adopted in February 1955, provided for construction of 12 atomic electro-stations of 1-2 million kw total power, and costing 300 million pounds sterling [2].

In 1956 this program was re-examined with consideration of the latest accomplishments of nuclear technology. The power of the projected electro-stations was increased to a total of 4-5 million kw, and their planned cost increased to 500 million pounds sterling. Recently the English government again re-examined the program and made a decision to build by 1965 between 16 and 19 atomic electro-stations of 6-7.5 million kw total power and costing 600-700 million pounds sterling [2].

Comparative Data of the English Atomic Electro-Stations [1, 8]

	Calder Hall	Hunterston	Bradwell	Berkeley
Thermal power, megawatt	2×180	2×625	2×540 (?)	—
Electrical power, megawatt	4×23	6×60	6×55+3×20	4×85
Fuel	Natural uranium			
Core dimensions (height/diameter) m	8.2/9.4	8.5/15.2	9.4/13.7	9.1/14.6
Number of channels	1696	3288	2600	3000
Grid spacing, cm	20.3	21	20.8	20.8
Weight of graphite, tons	2×1200	2×2150	—	—
Weight of uranium, tons	2×130	2×250	—	—
Shell dimensions (height/diameter), m	21.4/11.3	21.4 (sphere)	20.4 (sphere)	24.4/15.2
Shell wall thickness, cm	5.1	7.6	7.6	7.6
Gas pressure, atmos	7	10.5	9.1	8.7
Gas blower power, megawatt	2×5.44	2×12.6	—	—
Gas temperatures (inlet/outlet) °C	140/359	200/400	—	160/350
Wall temperature, °C	410	425	—	—
Number of heat exchangers	2×4	2×8	2×6	2×8
High pressure steam (atmos/°C)	14/312	41/371	53/373	21/320
Low pressure steam (atmos/°C)	4/176	11/354	14/373	4/320

By 1975 it is proposed to bring the power of the electro-stations up to 40-65 million kw, which will allow a saving of 100 to 150 million tons of coal per year [2]. (At the present time English industry uses approximately 215 million tons.)

The first stage of the program includes the construction of four atomic electro-stations of approximately 1 million kw total useful power. The construction of these electro-stations is to be completed toward 1960-1961. The design and construction of the atomic electro-stations has been assigned to four groups of industrial firms [1]:

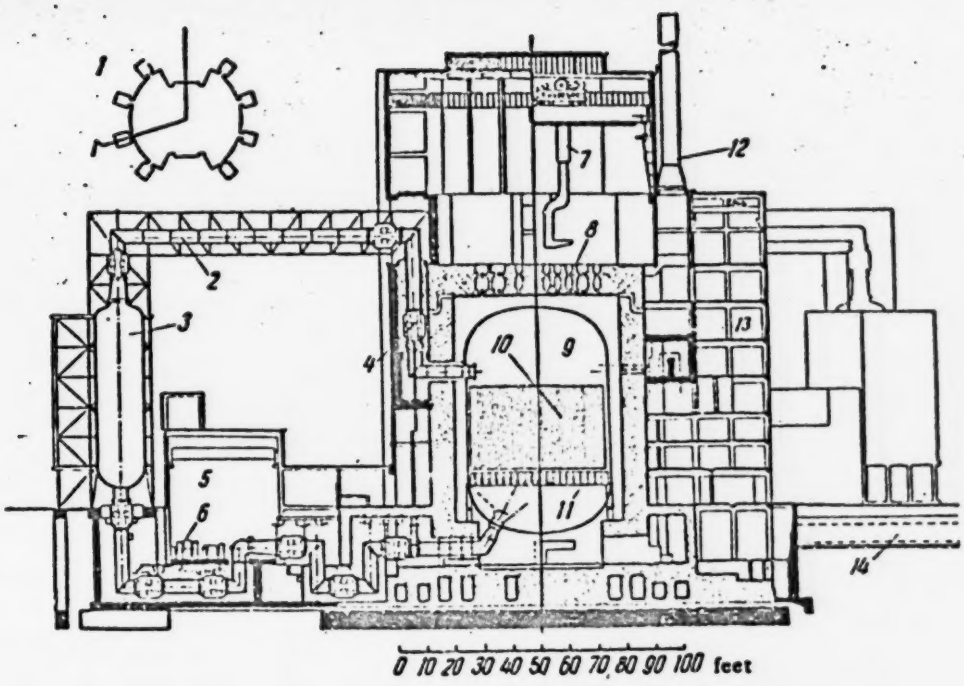

Fig. 1. Reactor for atomic electro-station at Berkeley: 1) plan view of the installation; 2) piping for CO_2; 3) heat exchanger; 4) valve; 5) gas blower area; 6) gas blower motor; 7) crane; 8) regulating rod mechanisms; 9) pressure shell; 10) core; 11) grid plate; 12) ventilation chimney; 13) offices and control rooms; 14) cables.

1) "Nuclear Power Plant Co." – building the electro-station at Bradwell, Essex;

2) "Associated Electrical Industries" – "John Thompson Nuclear Energy Co." – building the electro-station at Berkeley, Gloucestershire;

3) "General Electric Co." – "Simon-Carves Atomic Energy Group" – designing the largest of the four electro-stations – at Hunterston, Ayrshire, Scotland;

4) "English Electric" – "Babcock and Wilcox" – "Taylor Woodroy Nuclear Energy Group" – this group must build the atomic electro-station at Hinkley Point, Somersetshire.

In accordance with the chosen course of reactor building in England, all four electro-stations will be executed on the basis of one principal scheme: the source energy is a reactor loaded with natural uranium, with graphite moderator, cooled by carbon dioxide gas. (The station at Calder Hall and the industrial reactors at Chapel Cross are built on the basis of this same scheme.) However, from the engineering point of view, the new stations represent a step forward as compared to the Calder Hall station.

Comparative data of the three new stations is shown in the table.

The only thing known at present about the station at Hinkley Point is that it will have an electrical power output of 275 mw. The reactors will be enclosed by spherical shells and will have 8 heat exchangers each [1].

The basic departure of the projected stations from the one at Calder Hall lies in their assigned use. The reactor at the Calder Hall station is a double purpose one, that it, it is intended for production of plutonium and electrical energy (although at first the Calder Hall reactor was designed only for production of plutonium). The new stations must operate to the basic load on the electricity grid, in connection with which the periods of continuous reactor operation increase considerably (up to 80% of the installed and active time) with great-

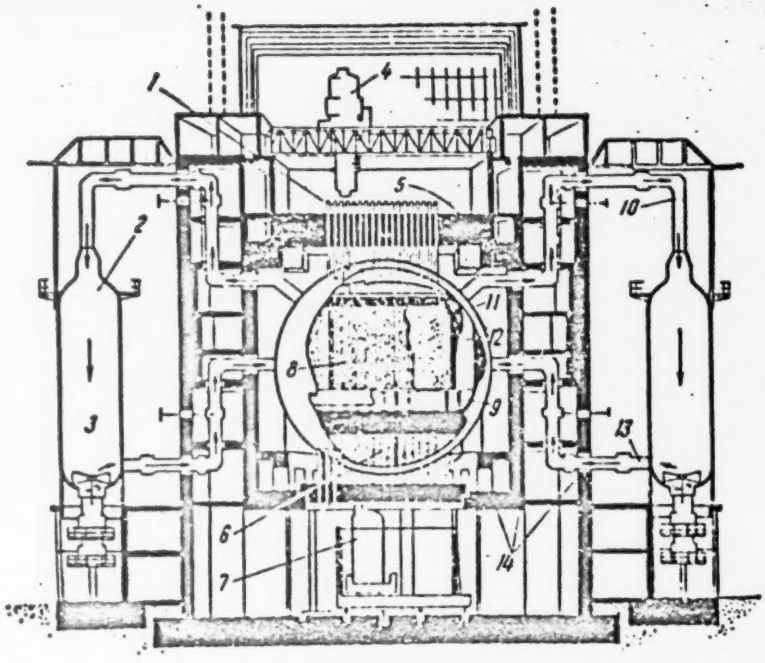

Fig. 2. Reactor for the atomic electro-station at Hunterston: 1) regulating rods; 2) heat exchanger; 3) gas blower; 4) machine for servicing the reactor; 5) upper concrete shield; 6) loading and unloading tubes; 7) loading and unloading machine; 8) core; 9) grid plate; 10) piping for heated gas; 11) outer shell under pressure; 12) inner shell; 13) piping for cooled gas; 14) concrete shielding.

er burn up of U^{235} and the Pu^{239} that is formed [8].

Another, no less important difference in the new stations is their great power and greater efficiency (no less than 28%). The increase in these parameters became possible through the use of a reactor of large dimensions and with a shell thickness of 7.6 cm, which allowed an increase in the core dimensions, and an increase in the gas pressure, thus improving heat transfer. In addition, increasing the size of the core induces an increase in reactivity of the reactor, which allows a flattening out of the heat flux along the radius.

From the operational standpoint the basic advantage of all the new stations is the possibility of conducting loading and unloading work during operation of the reactors. The design of the loading and unloading mechanisms is different for each of the projects. In the Scottish station project, loading and unloading of the reactor is done from below, in all the others from above. Changing the fuel elements from below has two apparent advantages: at the top cover of the reactor space becomes available which can be used for easier location of the regulating and control mechanisms; the manipulators required for channel replacement become simpler. It is interesting to note that the manipulators are equipped with television for visual observation of the replacement of the channels [10].

Increasing the core dimensions created serious difficulties in building the reactor pressure shells. Except for the Berkeley reactor, all the reactors have spherical shells, which allows increased gas pressures without inducing higher stresses in the shell walls. The reactor shell at Berkeley is similar to that at Calder Hall and differs from it only in dimensions; the entry and exit system for the gas is also similar to the Calder Hall scheme. The solution of this problem for a spherical shell is more complicated. The designers of the station in Scotland, for example, made the reactor shell with double walls: the inside wall is thin and made of heat resistant steel, serving as a heat shield; the outer wall is 7.6 cm thick and carries the pressure. The entering gas flows into the space between the walls, then into the channels, and through a pipe that pierces both walls

to the outside; to minimize heat loss, thermal insulation is used.

The system of heat removal by gas is the same in essential features in all the projects. Differences exist only in the selected gas blowers. At the Berkeley and Hinkley Point stations ordinary axial flow blowers are used, powered by alternating current induction motors; at the Bradwell station the blowers are powered by auxiliary turbogenerators. In the Hunterston reactor design the blowers are centrifugal type and are located inside the heat exchangers. The number of heat exchangers in all the reactor designs is eight per each installation, but at the Bradwell station the number has been decreased to six for economic reasons, but the heat transfer surface in each exchanger has been increased.

Construction work is already proceeding on the building for one of the reactors at Berkeley. About 400 people are employed at the construction site, and toward the end of 1957 this number will grow to 2000. Start up of the station is scheduled for spring of 1960 [3].

Construction work was begun at Bradwell on January 18, and work will begin at Hunterston in the very near future [7].

It is necessary to note that the rapid development of atomic energy in England has placed the metallurgical industry of the country in difficulty. At present there is felt a scarcity of sheet steel which is essential for the welded shells of the reactors and heat exchangers [2].

Expenditures for the construction of the first three stations will be about 120 million pounds sterling (capital costs will be 125-135 pounds/kw, which is 2-3 times higher than for coal burning stations) [4]. The cost of the nuclear fuel will be less than the cost of conventional fuel; therefore the cost of electrical energy (0.65-0.70 pence/kw-hr) will be comparable to the cost of electrical energy produced by conventional coal burning electro-stations [9].

L.S.

LITERATURE CITED

[1] Electr. Times 130, 3397, 331-334 (1956).

[2] Financial Times (January 15, 1957).

[3] Financial Times (January 18, 1957).

[4] Financial Times (January 19, 1957).

[5] Nucl. Power 1, 6, 237 (1956).

[6] Nucl. Power 1, 7, 302 (1956).

[7] Nucl. Power 2, 9, 3 (1957).

[8] Nucl. Power 2, 10, 39 and 42-57 (1957).

[9] Nucl. Engineering 2, 10, 5-10 (1957).

[10] Engineer 203, 5272, 219 (1957).

[11] Engineer 203, 5273, 260 (1957).

[12] Engineer 203, 5274, 282-285 (1957).

[13] Engineering 183, 4743, 152 (1957).

[14] Engineering 183, 4742, 121 (1957).

[15] Engineering 183, 4745, 218 (1957).

[16] Engineering 183, 4746, 249 (1957).

[17] Atomics and Nucl. Energy 8, 3, 93-96 (1957).

[18] Nucleonics 14, 12, R-1 (1956).

SMALL ATOMIC ELECTRO-STATIONS

As has previously been reported [1], the Oak Ridge National Laboratory has designed a small size atomic electro-station intended for use in remote and inaccessible places. A small size atomic electro-station with reactor APPR-1 (Army Package Power Reactor) has also been designed by the American Firm "Alco Products" for the Army. Construction of the station is being completed at Fort. Belvoir, Virginia, along the Potomac River, near Washington.

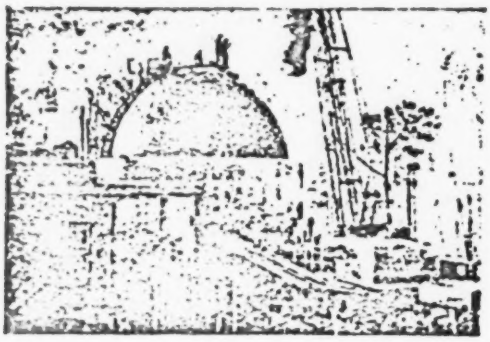

Fig. 1. Construction of the reactor APPR-1.

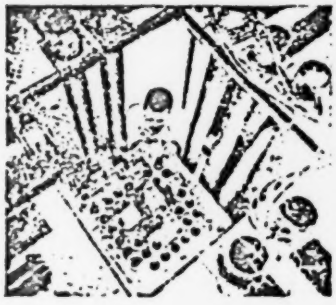

Fig. 2. Core of the reactor APPR-1.

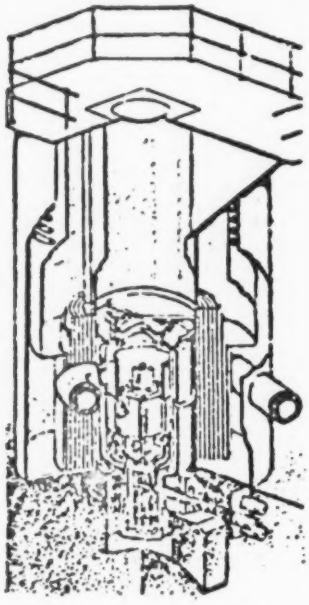

Fig. 3. Cross section of the reactor. The primary shield is composed of a layer of iron and water. Actuation of the regulating rods is accomplished from beneath the reactor core (some of the rods are not shown in the drawing). Coolant entry is at the left, exit at the right. For fuel element replacement the removable plate (bolted down) is lifted off and the elements are removed through the upper tank, which is filled with water.

It was recently announced [2] that the English firms "Humphries and Glasgow Ltd." and "Daniel Adamson and Co." concluded an agreement with the firm "Alco Products" regarding the construction in England of small size atomic electro-stations. In the first stages of construction about one third of the equipment and the fuel elements as well, will be supplied from the USA. Later the construction of such stations will be carried out by English industry. The reactors are designed for 2, 5, 10 and 25 mw of electrical power, which is enough for the electrical requirements of settlements containing 20000-40000 people. Considering the high cost of transporting conventional fuel, small size atomic electro-stations when built in remote areas, will be considerably more economical than small conventional electro-stations. The prototype for such reactors is the APPR-1, which uses pressurized water as the coolant and moderator. A reactor of the same type was installed on the submarine "Nautilus" [3]. A general understanding of the English small size atomic electro-stations can be gained from a description of the APPR-1 [4].

The electrical power output of the APPR-1 is approximately 2 mw. As structural materials it employs only mild carbon steel and stainless steel. The area occupied by the reactor building is not large (equal in area approximately to a tennis court) (Figure 1). The reactor is entirely safe. The area of horizontal cross section of the core,

consisting of 44 fuel elements, is approximately 0.25 m^2. The corner fuel elements are eliminated to give the core a more cylindrical form (Figure 2). The length of the fuel elements is about 90 cm, of which the active portion takes 55 cm. The fuel units are plate type and contain enriched uranium clad in stainless steel. In the future, tube type fuel units may be adapted. The fuel elements have end boxes for entry and exit of the coolant.

The regulating rods are actuated from below by means of a gear drive actuated by a shaft which passes through a pressure seal to a motor located externally. Reactor shut down is effected by safety rods falling into the reactor core under the action of gravity following the cutoff of current to electromagnetic clutches. The safety rods (5 in number) are hollow square tubes of absorbing material, that displace fuel elements. With the reactor running at full power the rods are moved out of the core and the fuel elements remain within it.

The core is surrounded by a thermal neutron shield and is located inside the pressure shell (diameter about 1.2 m, height 3.9 m). The primary coolant enters the reactor shell into a circular passage formed between the shielding and the shell wall, then passes into the lower, inlet, plenum chamber, rises through the core, and leaves it through the exit duct which is located on the same plane as the inlet (Figure 3). Water at a temperature of 230°C and a pressure of 85 atmos enters a cylindrical steam generator which is located vertically. The circulation of the primary loop water is accomplished by means of a hermetically sealed centrifugal pump. The pressure in the loop is maintained automatically by a volume compensator with electrical heating.

The reactor shell is closed at the top by a removable plate, above which is located a cylindrical tank 2.7 m high, that can be filled with water. Replacement of the fuel elements is done under water when the reactor is completely shut down. The shell and the reactor, surrounded by concentric layers of iron and water shielding, and also the upper cylindrical tank, are in their turn located in an external tank, having concrete shielding 60 cm thick.

The reactor, heat exchangers, pumps and mechanisms for replacement of fuel elements are all located in one building, made of iron and concrete and designed to contain the gaseous fission products in event of a reactor accident. The rest of the reactor equipment – turbines, water processing installation, control room, etc. – are located in a two story building, adjacent to the reactor building.

The small size, 10 mw electro-station being designed for England is characterized by the following data:

Reactor

Thermal power	46,000 kw
Total electrical power	10,600 kw
Useful electrical power	10,000 kw
Uranium enrichment	4-12%
Uranium loading	1.25-3.5 tons
Reactor duration at 100% load factor	18 months
at 80% load factor	30 months
Number of regulating rods	7-9
Average fast neutron flux	$5 \cdot 10^{14}$ neut/cm^2sec
Average thermal neutron flux	10^{14} neut/cm^2sec
Temperature coefficient of reactivity	$\Delta k = 3.6 \cdot 10^{-4}$/1°C

Primary Loop

Pressure	105 atmos
Coolant flow	34 m^3/min
Coolant temperature:	
at reactor inlet	250°C
at reactor outlet	270°C
Pressure shell:	
diameter	1.35 m
height	4.8 m

All surfaces in contact with the primary coolant are made of stainless steel.

Secondary Loop

Parameters of the secondary loop are dependent to a large extent on the choice of turbine type. However, for classification purposes they are as follows:

Steam:	
pressure	26 atmos
temperature	230°C
Steam flow through condenser	80 tons/hr
Back pressure in the condenser	63 mm Hg
Temperature of feed water	138°C

Shielding

The concrete shielding is 1-1.2 m thick and surrounds the equipment in the primary loop. The reactor building, filling the role of biological shielding, is 21 m in diameter and height. Used fuel elements are kept in a storage pool located in the reactor building.

Cost

The total cost (including the fuel elements) is estimated at 2 million pounds sterling.

I. Ch.

LITERATURE CITED

[1] Atomic Energy No. 1, 113 (1956).

[2] Financial Times (January 30, 1957), p. 9.

[3] Engineering 183, 4744, 183 (1957).

[4] Nucl. Power 2, 11, 104 (1957).

A FLOATING ATOMIC ELECTRO-STATION

An English magazine* has published an interesting proposal for construction of floating atomic electro-stations. The proposal is based on the following reasoning. The execution of the recently adopted accelerated program for construction of atomic electro-stations in England, can lead to the situation where it will be increasingly difficult to find in a short time ground space for new atomic electro-stations, which must be located near plentiful sources of water, and near locations suitable for disposal of radioactive wastes. For this reason the author proposes the location initially of atomic electro-stations on pontoons or in large iron and concrete barges. With such a station location the problem of a water supply disappears and (when the distance from shore is far enough) the problem of radioactive waste disposal is considerably simplified. The station must be connected to the electric network by underwater cable.

The construction of floating atomic electro-stations must be considered as a temporary measure until large stationary atomic electro-stations gradually replace conventional coal stations. In the future (about the year 2000 or earlier) the floating stations will grow so obsolete that it will be possible to sink them, thus economizing the time and facilities necessary for the disassembly of the stations. Finally, in the author's opinion,

*F. Myers, Engineer 203, 5272, 214 (1957).

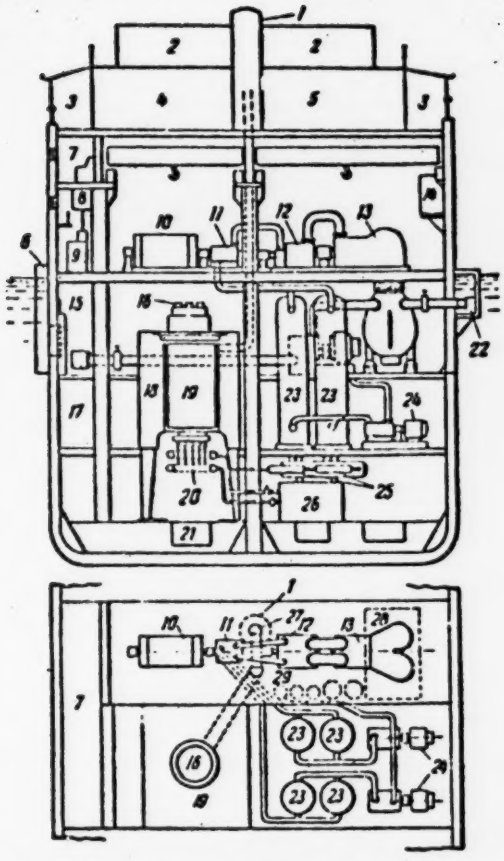

Cross sections of a floating atomic electro-station, showing a typical arrangement of reactor and turbogenerator of 50 mw: 1) exhaust pipe; 2) living quarters; 3) promenade deck; 4) service areas, shops, laboratories, etc.; 5) recreation room, dining room, etc.; 6) wire mesh strainer; 7) control room; 8) cables; 9) switchboard; 10) turbogenerator; 11) high pressure turbine; 12) intermediate pressure turbine; 13) low pressure turbine; 14) expansion tank; 15) water inlet for condenser cooling; 16) regulating rods; 17) fuel stores; 18) biological shield; 19) reactor; 20) coolant piping; 21) depleted channels; 22) outlet for water cooling the condenser; 23) heat exchangers; 24) feed pumps; 25) electromagnetic pumps; 26) coolant sump; 27) ventilator; 28) condenser; 29) feed water preheaters.

these stations can be so constructed (or reconstructed in the future) that it will be possible to adapt them to the use of thermonuclear energy based on the synthesis of the hydrogen in the sea water.

In order to obtain maximum speed in construction of the floating stations, it is essential to standardize the most suitable stations (suitable by weight and reliability). Reliability must be given more significance than the thermal efficiency of the station. The iron and concrete hull of the floating station can be prepared in a harbor, and the equipment installed with the aid of lifting cranes. From the harbor to the anchor site the station can be either towed or can proceed under its own power.

As fuel in the station's reactor, enriched uranium can be used, and as coolant, a sodium-potassium mix-

ture. A boiling water reactor could also be used on the floating station. The station must be completely automated.

The station must have installed turbines designed for steam at ordinary conditions (42 atmos, 427°C), with generators of 50 mw power rating each. Potential at generator terminals is 11 kv and is raised to 132 kv at a substation located at the opposite end of the floating station.

As is seen in the drawing, the reactor 19 of the station has small dimensions and is surrounded by biological shielding 18. The turbogenerators 10 are mounted on heavy steel frames under two bridge cranes. The heat exchangers 23 are located vertically (for drainage of the sodium-potassium mixture into the sump tank). The upper ends of the heat exchangers are connected by piping to the turbine.

Some difficulty is presented by the problem of locating maintenance personnel at the station, which must be designed as automatic in operation. Apparently, as in floating light houses, it will be possible to establish duty shifts on the station. However, if it becomes necessary to station personnel permanently aboard the station, it will be necessary to work out a number of additional measures to create normal working conditions for the personnel.

Yu. K.

NEW DATA CONCERNING URANIUM ALLOYS

Some new data concerning uranium alloys have recently been published.

The U–Bi system [1] has been studied metallographically and by x-ray diffraction, neutron diffraction and thermal analysis. Alloys containing up to 30% U were prepared in a graphite crucible at about 1300°C from pieces of uranium and bismuth (99.99%), the latter having been filtered through a porous Pyrex filter. Alloys with a higher U content were prepared from uranium powder and crushed bismuth, the uranium powder being obtained by hydrogenation and dehydrogenation in the same graphite crucible in which the alloy was prepared. The system is of practical interest, since bismuth is very fusible and has a low thermal neutron cross section, and U–Bi alloys may be used as liquid nuclear fuels. The phase diagram constructed from the data of many writers is given in [2].

Crystal structures, lattice parameters, A	Theoretical density, g/cm³	Other properties
UBi – body-centered tetragonal, $a_0 = 11.12$; $c_0 = 16.55$; $c_0/a_0 = 0.95$	13.6	Most pyrophoric compound
U_3Bi_4 – cubic, $a_0 = 9.350$	12.59	Least pyrophoric compound
UBi_2 – cubic, $a_0 = 8.89$	12.4	Harder than the other compounds

The principal features of the diagram can be expressed by the following reactions:

Eutectic	$Bi + UBi_2 \xrightleftharpoons{270^\circ C} L_{\sim 0.05}$;	
Peritectic	$L_{34.0} + U_3Bi_4 \xrightleftharpoons{1010^\circ C} UBi_2$;	
Peritectic	$L_{\sim 20.0} + UBi \xrightleftharpoons{\sim 1050^\circ C} U_3Bi_4$;	
Syntectic	$L_{61.0} + L_{99.0} \xrightleftharpoons{1400-1450^\circ C} UBi$ and	
Eutectic	$\gamma U + UBi \xrightleftharpoons{1130^\circ C} L_{\sim 99.0}$	

(The indices against L denote the percentage of uranium in the liquid.)

The properties of the intermetallic compounds are shown in the table above.

The solubility of bismuth in solid uranium is not recorded. The solubility of uranium in liquid bismuth was found up to 900°C [1].

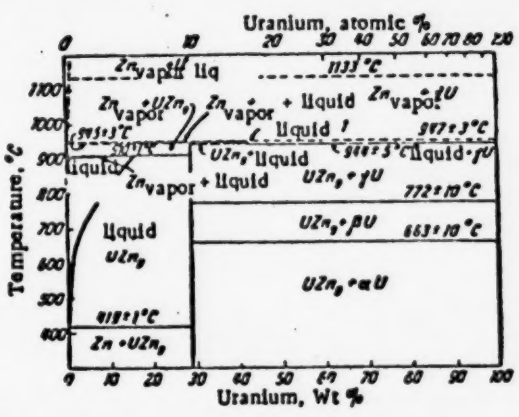

Fig. 1. Phase diagram of U–Zn system at p = 1 atm.

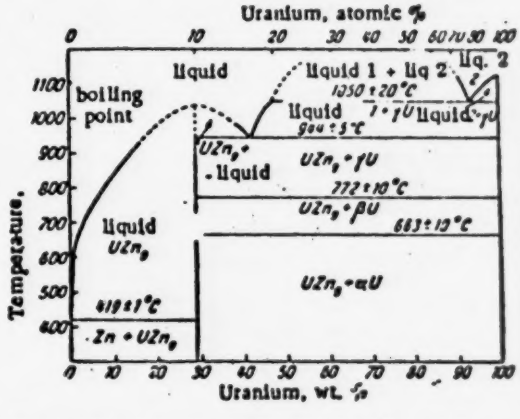

Fig. 2. Phase diagram of U–Zn system at p = 5 atm.

U–Si system. The republished diagram [2,3] includes all the phases previously known; only the margins of the diagram have been really satisfactorily studied. With the exception of U_3Si, all the compounds have covalent bonds between the Si atoms and are very brittle, although none of them has outstanding hardness. Alloys of composition between U_3Si_2 and USi_2 are resistant to atmospheric corrosion; they spark copiously when abraded. Metallographic examination [3] shows that the compound U_3Si (ε-phase) exists at about 23 atomic % Si, i.e., it does not correspond to the stoichiometric composition. It is formed at 930°C by peritectoid reaction. Alloys with the ε-phase should preferably be poured at a temperature of about 1625°C in a chill to obtain U_3Si_2 dendrites of maximum grain fineness. Cooling can be done in a graphite crucible, but if contamination by carbon is to be avoided, a beryllium crucible must be used. To transform the cast alloy to the ε-phase, long-continued annealing (4-6 days) at 800°C is recommended. During this treatment, hardness falls considerably (from 40 to about 22 R_C) and density increases.

The ε-phase has relatively high plasticity. When contained in a copper jacket, it can be cold formed with a 20% reduction. The ε-phase can be satisfactorily extruded at 850°C with an extrusion constant K = 31.6 kg/mm² ($p = K \ln R$, where p is the specific extrusion pressure and R is the ratio of the initial to the final cross section).

Carbon lowers the temperature of the peritectoid transformation of the ε-phase; metallographic observation shows that in the presence of up to 0.1 wt % carbon, the carbide phase does not appear. The effect of carbon on the physical properties of the ε-phase was not determined. The ε-phase is also obtained in ternary alloys on adding 1 to 10 atomic % niobium, nickel, iron, beryllium, aluminum, zirconium and copper to uranium

containing 15 atomic % Si.

The U–Zn system has been studied [4] by metallographic analysis, x-ray diffraction, thermal analysis and measurement of the vapor pressure from the "dew point." The alloys were prepared from uranium (total impurities less than 0.05%) and zinc of a purity > 99.99% in crucibles of high purity magnesia, magnesia containing calcium fluoride or tantalum (when heated in an atmosphere of helium for 10-15 min at 1100-1200°C, tantalum does not react with the alloy). The charge cleaned by washing with weak HNO_3, rinsed and dried, was placed in a dry chamber filled with helium, where it was placed in a crucible of tantalum 0.25 mm thick. The crucible was then sealed by welding on it a tantalum cap and was placed inside a stainless steel bomb (AISI 309) which was also hermetically sealed.

In another method of preparing the alloy, degreased and pickled uranium turnings were pressed with granulated zinc into 20 g compacts under a pressure of 1.40 tons/sq cm. The compacts were placed in a MgO crucible and sealed in evacuated tubes of Vycor (high melting point glass) or quartz. The alloy was homogenized for two weeks at 550°C; during this treatment its volume increased by several percent. Phase diagrams for pressures of 1 atmos (Figure 1) and 5 atmos (Figure 2) were constructed on the results of the investigation [4]. The pressure was produced by zinc vapor and in addition by helium in the stainless steel bombs. Variation in the pressure did not appreciably affect the position of the solid-solid or solid-liquid boundaries. The solubility of uranium in zinc was determined in separate experiments. The solubility of zinc in solid uranium is low and could not be detected by either metallographic or thermal analysis. The only intermediate compound discovered, U_2Zn_{17} [5] and not UZn_9 as indicated in [4] has a hexagonal structure and belongs to the space class D^4_{3h} with $a_0 = 8.99$ A, $c_0 = 26.35$ A and $d_{exp} = 8.50$ g/cm^3, $d_{x\text{-}ray} = 8.57$ g/cm^3; according to metallographic data [4], the x-ray region of homogeneity (theoretical composition 28.805 wt % U) is less than 0.7 wt %, and according to structural data [5] it lies within the limits U_2Zn_{15-17}.

G.Z.

LITERATURE CITED

[1] R.J. Teitel, J. Metals 9, Sec. 2, 131 (1957).

[2] Nuclear Reactors, III, Materials for Nuclear Reactors (IL, Moscow, 1956), pp. 298-302.

[3] A. Kaufmann, B. Cullity and G. Bitsianes, J. Metals 9, Sec. 2, 23 (1957).

[4] P. Chiotti, H.H. Klepfer and K.J. Gill, J. Metals 9, Sec. 2, 51 (1957).

[5] E.S. Makarov and S.I. Vinogradov, Crystallography 1, 634 (1956).

BRIEF REPORTS

England. A new experimental reactor (NERO) has been installed at Harwell; the thermal capacity of the reactor is less than 100 watts. This reactor is intended for research with the idea of improving English reactors in which gas coolants and graphite moderators are used.

The reactor is a graphite stack, the dimensions and shape of which can be changed within the limits of a diameter of 4.2 meters and a height of 3 meters. The graphite stack is surrounded by a concrete shield of 60 cm in thickness.

Heat-exchanger elements of different types can be placed in the stack with various spacing and lattice configurations. The arrangement of the heat-exchanger elements can be changed in a few days. The reactor is controlled by cadmium rods. The maximum thermal-neutron flux is 10^8 neut/cm^{2}sec.

The reactor will be used mainly for checking calculations in studies of the effect of the fissionable isotopes U^{235} and Pu^{239} and the original material U^{238} on the physical characteristics of graphite reactors. It is also proposed to study the use of sodium as a coolant in graphite reactors. For this reason the reactor has been named NERO (Na experimental reactor zero energy). (Engineering 183, 4749, 346, 1957.)

USA. According to a statement issued by the AEC, in 1975 the electric power generated by nuclear power stations in the USA is expected to reach 50,000-75,000 megawatts; it is anticipated that several hundred reactors will be built. By 1962 the electric power of nuclear installations, proposed or under construction, will be 1,000 megawatts, in 1965, 3,000-4,000 megawatts. Up to 1975 the power of nuclear installations will be increased by some 8,000-12,000 megawatts per year.

The data given by the AEC includes all reactors built in the USA (including demonstration reactors), a total of 231 reactors; of these, 94 are in the design stage, 46 are being built, 74 are completed or already operating, and 17 are demonstration reactors.

Of the 46 reactors which are under construction only 5 can be considered as industrial power reactors. Hence the program of building several hundred power reactors in the next one or two decades will be a formidable task for American industry. (Nucl. Power 2, 11, 83, 1957.)

USA. The Westinghouse Electric Corporation, Pennsylvania Power and Light Company and Union Carbide Nuclear Company plan the construction of a new nuclear power station with a capacity of 150 megawatts.

It is proposed to use a mixture of enriched uranium and thorium in the form of a suspension in heavy water as the fuel; this fuel will circulate through the reactor and deliver heat to a steam generator. The advantage of this type of reactor is the possibility of reprocessing nuclear fuel continuously at a nuclear power station without disturbing operation.

It is expected that the station will be completed in 1962. (J. of Commerce, February 27, 1957.)

USA. 60 miles from San Francisco (at Stockton, California) a site has been chosen for the construction of a center for the development of methods and research into the economic utilization of radiation for conservation and pasturization of feed. A reactor will be built on this site (cost 3 million dollars) and used for irradiation of feed products; an accelerator and laboratory, etc. will also be built at a cost of 4.5 million dollars. (Nucleonics 14, 12, R-7, 1956.)

USA. To satisfy the growing need for the boron isotope B^{10}, the Atomic Energy Commission has set up an installation at Niagara Falls (New York State).

The output, containing 30-95% of the isotope B^{10}, will be produced in kilogram quantities in pure form and in the form of chemical compounds. (Atomic Energy Guideletter, No. 109, February 15, 1957.)

USA. A group of American firms has developed an atomic battery which, it is expected, will find wide application. In the battery, which is about twice the size of a tablet, energy is transformed from one form to another. The β-rays emitted by promethium-147 fall on a phosphor layer which gives off light flashes; the light energy is then converted into electrical energy.

Promethium-147 is not dangerous but its cost at the present time is quite high (500 dollars per curie) and the amount of promethium used in one battery is worth more than 200 dollars. It is expected that the cost of promethium will be reduced to 50 cents per curie when methods are developed for the extraction of large amounts from fission products. (Newsweek 49, 5, 39, 1957.)

Italy. Close to the small city of Ispra on the shore of Lake Maggiore an atomic center will be built on a site of 395 acres. The first nuclear reactor will be built on the site in 1958. (Discovery 18, 2, 83, 1957.)

Federated Republic of Germany. The Parliament of the country of Severny Rein-Westpthal has approached the government of the FRG with a proposition to acquire a DIDO reactor from Great Britain. The reactor will be used for scientific research at the atomic center which will be set up near Düsseldorf (Atomic Energy Newsletter 16, 13, 4, 1957.)

BIBLIOGRAPHY

NEW LITERATURE

Amirkhanov, Kh.I. and Brandt, S.B. Determination of the Absolute Age of Rocks by the Radioactive Transformation of Potassium-40 into Argon-40 (Makhachkal). Dagestan Branch, Acad. Sci. USSR, 1956, 149 pp., 8 rubles, 50 kopecks.

Astafev, V.Ya. Atomic Energy and its Application. Penza, 1956, 65 pp., free.

Voitkevich, G.V. Radiogeology and its Significance in the Understanding of the History of the Earth. State Geo. Tech. Press, 1956, 110 pp., 5 rubles, 20 kopecks.

Questions of Radiobiology. Collection. Trans. by A.A. Baev, et al. Ed. and with an introduction by G.M. Frank. IL, 1956, 578 pp., 22 rubles, 10 kopecks.

Grigoruv, P.F. Examination of Wear of Parts of an Aviation Engine by Radioactive Isotopes. Branch of the All-Union Inst. of Scientific and Tech. Information, 1956, 13 pp., with diagrams, 4 rubles.

Desov, A.E. Heavy and Hydrated Concretes (for Protection from Radiation Effects). State Construction Press, 1956, 88 pp., 3 rubles, 10 kopecks.

Dzhelepov, B.S. and Peker, L.K. Decay Schemes for Radioactive Isotopes. Izvestia Akad. Nauk SSSR, 1956, 176 pp., free.

Study of the Wear of Machine Parts by Radioactive Isotopes. Collection of Articles Ed. by P.E. Dyachenko. Izvestia Akad. Nauk SSSR, 1957, 144 pp., 5 rubles, 45 kopecks.

Kachur, L.A. et al. Radiation Sickness. Aftereffects of Radioactive Emanations. State Medical Press, 1956, 95 pp., 2 rubles, 25 kopecks.

Levchuk, T.P. et al. Radioactive Isotopes and Their Use in Biochemistry and Medicine. "Znanie" Press, 1956, 32 pp., 60 kopecks.

Masalov, G.I. Use of Radioactive Isotopes for Stamping Cold-Rolled Steel Strips. Branch of the All-Union Inst. of Scientific and Tech. Information, 1956, 10 pp., with illustrations, 1 ruble, 50 kopecks.

Material on the Toxicology of Radioactive Substances. Collection of Articles Ed. by A.A. Letavet and E.B. Kurlyandskaya, State Medical Press, 1957, 203 pp., 8 rubles, 40 kopecks.

Mezentsev, V.A. The Atom and Atomic Energy. 3rd Revised Edition. Military Press, 1957, 200 pp., 3 rubles, 10 kopecks.

Scientific Conference on the Use of Radioactive Isotopes in Technology, Biology and Medicine. Riga, 1956, 35 pp., free.

Problems in the Use of Atomic Energy. Collection of Articles. 2nd Revised and Expanded Edition. Military Press, 1956, 624 pp., 7 rubles, 45 kopecks.

Soboleva, M.V. and Pydovkina, A.I. Uranium Minerals. Handbook. State Geolog. Tech. Press, 1957, 408 pp., 20 rubles, 90 kopecks.

The Physical and Technical Aspects of the Use of Radioactive Isotopes. Collection of Articles. Editorial Staff: Ya.E. Chudars (chief ed.), et al. Riga Press of Acad. Sci. of the Latvian SSR, 1956, 165 pp., 6 rubles, 95 kopecks.

Chemistry and Geochemistry. Collection of Articles. Chief ed. I.E. Starik. Trans. of the V.G. Khlopkin Radiation Institute, Izvestia Akad. Nauk SSSR, 215 pp., 11 rubles, 80 kopecks.

Shlyk, A.A. Tracer Isotopes in the Study of the Biosynthesis of Chlorophyl. Minsk. Press of Acad. Sci. Belyorussian SSR, 1956, 299 pp., 10 rubles.

Shklovsky, I.S. Cosmic Radiation. State Tech. Press, 1956, 492 pp., 15 rubles, 75 kopecks.

Nuclear Geology. Trans. from the English by G.V. Avdzeiko. Ed. with introduction by I.E. Starik. IL, 1956, 555 pp., 22 rubles, 30 kopecks.

Journal Articles

Adamovich, L.P. and Yutsis, B.V. Photometric Determination of Beryllium and Beryllium Bronzes. Ukrainian Chem. J. Vol. 22, No. 6 (1956).

Airapetyan, M.A. and Polak, L.S. Use of Radioactive Isotopes for the Study of the Movement and Distribution of Fluids in a Seam. Proc. of the Oil Inst. of the Acad. Sci., Kazakhstan SSR Vol. I (1956).

Akimov, A.I. Spectral Analysis of Small Admixtures of Cerium and Praseodymium in Lanthanum by the Addition Method. Optics and Spectroscopy Vol. 2, No. 2 (1957).

Akimov, Yu.K. et al. Useful Fast Neutron Detector. Instruments and Experimental Techniques No. 2 (1956).

Alekseev, A.I. Cross Section for the Photoproduction of a Positron in an External Field with Radioactive Corrections (letter to the Editor). J. Exptl.-Theoret. Phys. Vol. 31, No. 5 (1956).

Alpers, V.V. and Surkova, L.V. Measurement of the Gaps in the Tracks of Charged Particles in Nuclear Emulsions. Inst. Experimental Technology No. 2 (1956).

Atavin, P.I. Operations on Blood Vessels in Severe Radiation sickness (Experimental Research). J. Military Medicine No. 2 (1957).

Afrikyan, L.M. Production of μ-Meson Pairs by γ-Quanta in Nuclei (Letter to the Editor). J. Exptl.-Theoret. Phys. Vol. 31, No. 6 (1956).

Batenin, I.V. and Sharov, B.V. X-Ray Installation for the Structural Exploration of Radioactive Materials. Instruments and Experimental Techniques No. 3 (1956).

Bereznyak, N.G. and Eselson, B.N. Density of the Normal Component of Solutions of Helium Isotopes (letter to the Editor). J. Exptl.-Theoret. Phys. Vol. 31, No. 5 (1956).

Bolshakov, K.A. et al. Study of Solubility in the System $UO_2S_2O_4-H_2C_2O_4-H_2O$. J. Inorganic Chem. Vol. 2, No. 1 (1957).

Budnitskaya, E.V. et al. The Changes in the Substrate of a Lipoid Exchange (in plants) and the Activity of a Lipoxidase Under the Influence of Ionizing Radiation. Biochemistry Vol. 21, No. 6 (1956).

Burnazyan, A.I. The Atom on Guard for Health. Science and Life No. 1 (1957).

Vasilevsky, N.M. The Coagulability of Blood Under the Effects of Ionizing Radiations. Byelorussian Health Service No. 1 (1957).

Viktorov, D.V. and Maksimov, M.Z. Dependence of the Taper Length of a Trail in Photoemulsions on the Particle Charge. J. Exptl.-Theoret. Phys. Vol. 32, No. 1 (1957).

Gamaleya, A.N. Clinical Uses of Radioactive Isotopes. J. Military Medicine No. 2 (1957).

Gertsriken, S.D. A New Method of Determining the Diffusion Coefficient in Solid Bodies, Using Tracer Atoms. Collection of Scientific Works of the Inst. of Metal-Physics, Acad. Sci. Ukrainian SSR No. 7 (1956).

Grigorev, E.L. and Soloveva, L.P. Nuclear Disintegrations Produced in Photoemulsions by 660 Mev Protons. J. Exptl.-Theoret. Phys. Vol. 31, No. 6 (1956).

Davidchuk, L.Ya. and Chmutov, K.V. A Simple Radioactivity Indicator. J. Phys. Chem. Vol. 30, No. 12 (1956).

Danilov, V.I. et al. Method of Increasing the Density of a Beam of Protons from the 6-Meter Synchrocyclotron. Instruments and Experimental Techniques No. 3 (1956).

Dzhelepov, V.P. et al. Interaction of Negative π-Mesons with Carbon and Lead at 210-250 Mev. J. Exptl.-Theoret. Phys. Vol. 31, No. 6 (1956).

Dontsov, Yu.P. and Striganov, A.R. Single-Isotope Mercury Light Source and Determination of the Cross Section for Thermal-Neutron Capture by Au^{198}. Optics and Spectroscopy Vol. 2, No. 1 (1957).

Derdi, G. A Physical Model of the Hyperon (Letter from Budapest). J. Exptl.-Theoret. Phys. Vol. 32, No. 1 (1957).

Zvyagintsev, O.E. and Sudarikov, B.N. Salicylates of Uranium and Thorium. J. Inorganic Chem. Vol. 2, No. 1 (1957).

Ivanenko, D.D. and Pustovalov, G.E. Meson-Atoms. Usp. Fiz. Nauk Vol. 61, No. 1 (1957).

Ivanov, Yu.S. and Fesenko, A.I. Increase of Efficiency of a Wilson Chamber Working in the Photon Beam of a Synchrocyclotron. Instruments and Experimental Techniques No. 3 (1956).

Kavkin, L.P. A Radioactive Ionization Manometer. Instruments and Experimental Techniques No. 2 (1956).

Karibskaya, E.V. and Malenkova, K.M. Reaction of an Animal Organism to Ionizing Radiation under Cobalt Feeding. Bulletin of Roentgenology and Radiology No. 6 (1956).

Kelman, V.M. et al. Study of the Conversion Lines in the β-Spectrum of a Mixture of the Isotopes Eu^{153} and Eu^{154}. J. Exptl.-Theoret. Phys. Vol. 32, No. 1 (1957).

Kogan, A.V. and Sokolov, I.A. The Total Energy of the β-Transition RaC-RaC' (Letter to the Editor). J. Exptl.-Theoret. Phys. Vol. 31, No. 5 (1956).

Kozyreva, E.F. The Interaction Mechanism of the Particles in a Discharge Plasma. Optics and Spectroscopy Vol. 2, No. 1 (1957).

Kompaneets, A.S. The Establishment of the Thermal Equilibrium between Quanta and Electrons. J. Exptl.-Theoret. Phys. Vol. 31, No. 5 (1956).

Kondratev, L.N. et al. α-Decay of Pu^{240}. J. Exptl.-Theoret. Phys. Vol. 31, No. 5 (1956).

Kononenko, A.M. Computation of the Dose Level due to α-Radiation during the Distribution of a Radioactive Substance in an Organism. Biophysics Vol. 2, No. 1 (1957).

Kuznetsov, V.I. et al. Clinical Symptoms in Persons Subjected for Considerable Periods to Ionizing Radiation. J. Military Medicine No. 2 (1957).

Lapidus, L.I. Isotopic Invariance and Particle Production. J. Exptl.-Theoret. Phys. Vol. 31, No. 5 (1956).

Lapitsky, A.V. et al. Formation of Lower Oxides of Niobium and Tantalum in Some Deoxidation and Oxidation Reactions. J. Inorganic Chem. Vol. 2, No. 1 (1957).

Lozhkin, O.V. and Perfilov, N.A. Heavy Nuclear Fragments in Disintegrations Produced by Fast Protons in a Nuclear Emission. J. Exptl.-Theoret. Phys. Vol. 31, No. 6 (1956).

Lonina, N.A. et al. Dependence of Detection Properties of Nuclear Emulsions on Temperature. J. Scientific and Applied Photography and Cinemaphotography Vol. 2, No. 1 (1957).

Luchnik, N.V. Anomalous (Biological) Reaction Under Small Irradiation Doses. Biophysics Vol. 2, No. 1 (1957).

Lvov, V. Facts of the Atomic Age (from the History of the Discovery and Use of Atomic Energy). Conclusion. The Star No. 3 (1957).

Neudachin, V.G. Selection Rules for the "Seniority" Quantum Number in Nuclear Reactions (Letter to the Editor). J. Exptl.-Theoret. Phys. Vol. 31, No. 5 (1956).

Popov, M.M. and Gagarinsky, Yu.V. The Composition and Pressure of Dissociation of a Stable Crystal Hydrate of Uranium Tetrafluoride. J. Inorganic Chem. Vol. 2, No. 1 (1957).

On the term "Cyclotron Resonance" (Letter to the Editor from Ya.G. Dorfman and V.N. Lazurkin). Usp. Fiz. Nauk Vol. 61, No. 1 (1957).

Rodin, S.S. The Antineutron. Science and Life No. 1 (1957).

Rydnik, V.I. Rays Transform Metals (Possibilities in the Use of Radioactive Radiations for Changing the Properties of Metals and Alloys). Science and Life No. 2 (1957).

Takibaev, Zh.S. Study of Showers Formed in a Photoemulsion by Cosmic Ray Particles in the Stratosphere. Bulletin of the Kazakhstan Acad. of Sci. No. 1 (1957).

Tamm, I.E. The Structure of Nucleons (Letter to the Editor). J. Exptl.-Theoret.Phys.. Vol. 32, No. 1 (1957).

Fok, M.V. Study of the Afterglow of an Eu^{+++} Ion in a Phosphor with a Thorium Oxide Base. Optics and Spectroscopy Vol. 2, No. 1 (1957).

Freidlina, P.Kh. et al. Exchange Reactions of Tetraacetylacetonate of Zirconium. News of the Izv. Akad. Nauk SSSR, Div. Chem. Sci. No. 1 (1957).

Furman, K.S. Measurement Applications of X-Rays Excited by β-Rays. Instrument Design No. 1 (1957).

Khokhlov, Yu.K. Certain Sum Rules for Cross Sections of Electric Quadrupole Transitions in the Nuclear Photoeffect. J. Exptl.-Theoret. Phys. Vol. 32, No. 1 (1957).

Tserkovnikov, Yu.A. Stability of Plasma in a Strong Magnetic Field. J. Exptl.-Theoret. Phys. Vol. 32, No. 1 (1957).

Sheremetev, G.D. Optical Properties of Uranium Hexafluoride. Optics and Spectroscopy Vol. 2, No. 1,(1957).

Emanuel, N.M. The Stimulation of the Chain Branches of Reactions by Penetrating Radiation in the Initial Development of a Process. Doklady Akad. Nauk SSSR 111, No. 6 (1956).

Estulin, I.V. et al. Gamma Rays Emitted by J, Rh and Co in Thermal-Neutron Capture (Letter to the Editor). J. Exptl.-Theoret. Phys. Vol. 31, No. 5 (1956).
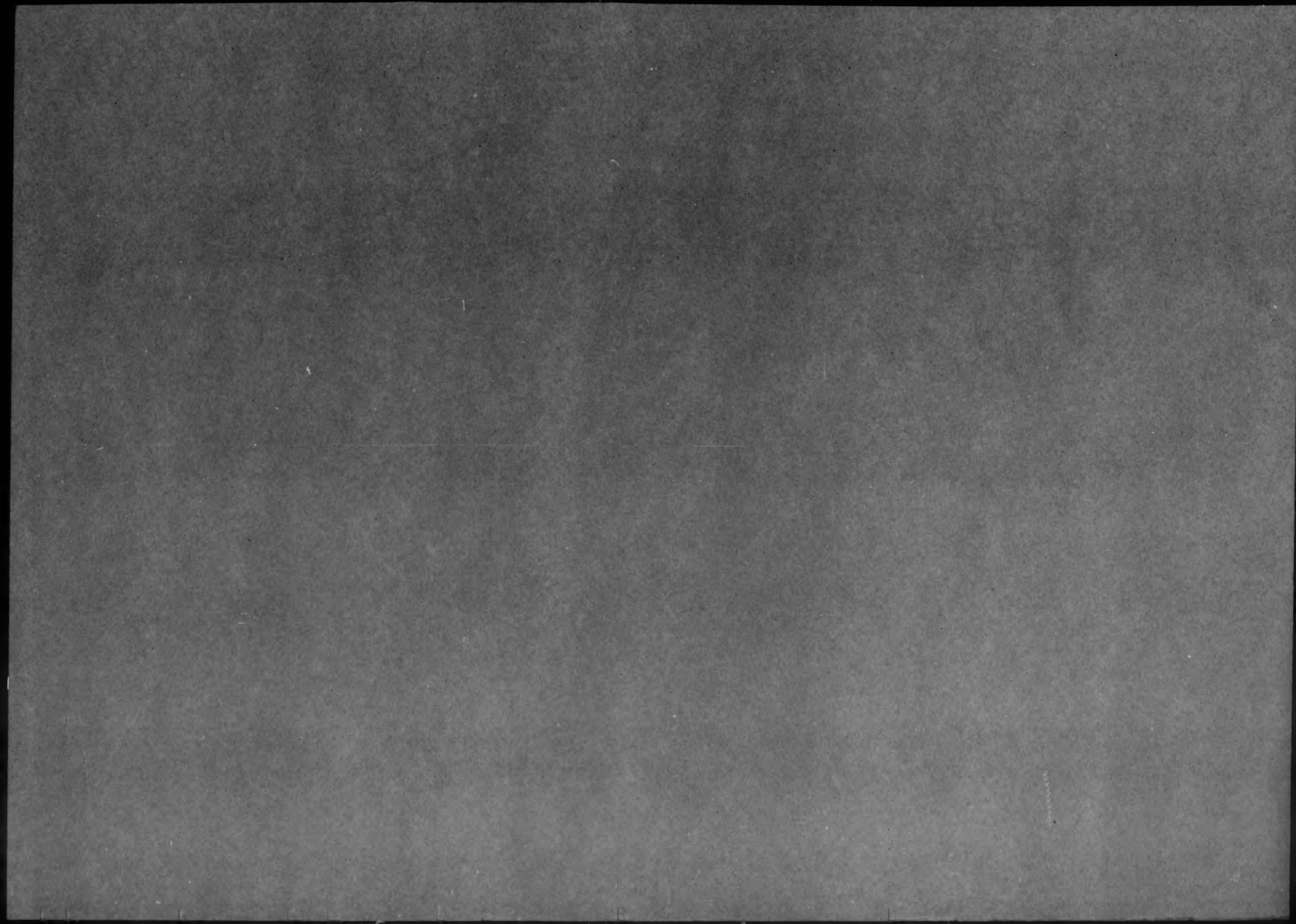
Nuclear Cooling (Trans. of an article from the English Journal "Nature"). Usp. Fiz. Nauk Vol. 61, No. 1 (1957).